

**AERODYNAMICS AND ENERGETICS OF ANIMAL FLIGHT
BASED ON PROPELLER MODELS**

James Richard Usherwood

A dissertation for the degree of Doctor of Philosophy in the University of Cambridge

Queens' College

May 2001

Preface

This dissertation is an account of work carried out in the Department of Zoology, University of Cambridge, between October 1996 and October 2000, under the supervision of Prof. C.P. Ellington. It is the result of my own work and includes nothing which is the outcome of work done in collaboration.

Acknowledgements

I would like to thank the following people for their help during the course of this research: Steve Ellis for constructing, advising on, and modifying, the propeller designs; Ian Goldstone for help and advice on all matters technical; members, both present and past, of the Insect Flight Group, and other friends from the Department of Zoology, Queens' College, and Portugal Place Squash Club.

Finally, the supervision of Prof. Charlie Ellington has been special. Despite various frustrations and delays during this work, meetings with Charlie left me feeling inspired, enthused and motivated.

This work was supported by a B.B.S.R.C. Research Studentship, and I am especially indebted to Tom Edwards for providing accommodation for me during the final year.

Contents

Preface	<i>i</i>
Acknowledgements	<i>i</i>
Contents	<i>ii</i>
Symbols and abbreviations	<i>v</i>
A graphical description of relevant angles of attack and incidence	<i>viii</i>
Chapter 1: General introduction	1
Horizontal and slow flapping flight.....	1
Analyses of hovering animal flight	1
Leading-edge vortices in engineering applications	3
Outline of the present study.....	6
Chapter 2: The aerodynamics of revolving hawkmoth wings	8
Introduction	8
Materials and methods.....	11
The experimental propeller.....	11
Wing design.....	14
Smoke observations.....	18
Force measurements	19
Experimental protocol	22
Data processing.....	23
Coefficients.....	29
Display of results	34
Results	35
Force results.....	35
Air-flow observations	42
Discussion.....	44
Vertical force coefficients are large.....	44

The relationship between C_v and C_h for sharp, thin wings	48
The effects and implications of wing design	56
Accounting for differences between ‘Early’ and ‘Steady’ propeller coefficients	58
Conclusion	61
Chapter 3: Propeller force coefficients from mayfly to quail.....	62
Introduction	62
Aspect ratio	62
The implications of Reynolds number to flight.....	63
Key species	64
Materials and methods.....	65
Large propeller experiments	65
Small propeller (‘mini-spinner’) experiments	68
The mini-spinner for low Re : model mayfly wings.....	68
The mini-spinner for high Re : real and model quail wings	73
Results	77
AR series	77
<i>Bombus</i> results.....	77
Steady results for range of species	81
Discussion.....	83
Steady high-lift mechanisms exist for a wide range of revolving wings.	83
Further implications of aspect ratio	84
The ‘normal force relationship’ is unaffected by induced downwash.....	90
Conclusion	93
Chapter 4: The ‘normal forces model’: A new method for estimating the power requirements of slow flapping flight	94
Introduction	94
Traditional approaches to power estimates for slow flight.....	94
The present study	94
Methods	98
General assumptions.....	98
Models	100

Parameters	106
Results	113
Discussion.....	122
Hovering with a horizontal stroke plane.....	122
Slow flight with an inclined stroke plane	124
Conclusion	126
Chapter 5: General discussion.....	127
‘Propeller’ force coefficients and the future of propeller-based experiments.....	127
Power calculations.....	127
Animal hovering is inefficient.....	129
Implications to Micro Air Vehicle design	130
References.....	132

Symbols and abbreviations

The symbols and abbreviations used in the text are given below, along with a description of their meanings. In most cases each symbol has a single definition, but a few have a secondary meaning which is used briefly. For these instances, the chapter in which the secondary meaning is used is stated.

Symbol or abbreviation	Description
a	Model angle of attack for error analysis
A	Area of far wake
AR	Aspect ratio
A_0	Area swept by wings projected on to horizontal plane
c	Wing chord
C	Speed-sensitive components of electrical power loss
C_D	Drag coefficient
$C_{D,FP}$	Drag coefficient for a flat plate in perpendicular flow
$C_{D,ind}$	Induced drag coefficient
$C_{D,pro}$	Profile drag coefficient
C_h	Horizontal force coefficient
C_L	Lift coefficient
C_N	Normal force coefficient
C_R	Resultant force coefficient
C_v	Vertical force coefficient
D_{ind}	Induced drag
D_{par}	Parasite drag
D_{pro}	Profile drag
F	Force
F_h	Horizontal force
F_R	Resultant force
F_v	Vertical force

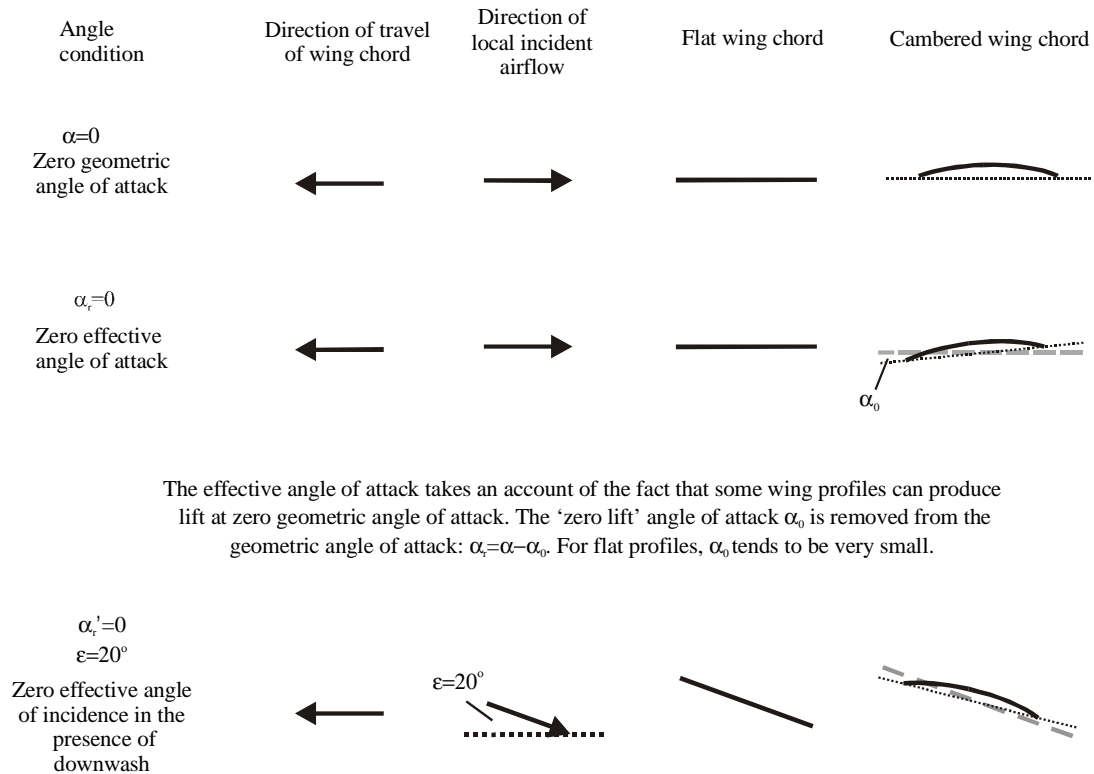
g	Acceleration due to gravity
I	Electric current
k_{ind}	Correction factor for induced power
L	Lift
LEV	Leading-edge vortex
m	Total body mass
m_{m}	Muscle mass
m_{w}	Wing mass
m_2	Second moment of mass (moment of inertia) of both wings
n	Wingbeat frequency
N	Integer number
P	Power
P_{acc}	Inertial power
P_{aero}	Aerodynamic power
P_{ind}	Induced power
P_{met}	Metabolic power from respiratory gas analysis
P_{pro}	Profile power
P_{winding}	Power due to winding in electric motor
Q	Torque
r	Radial position along the wing
$\hat{r}_1(S)$	Non-dimensional first moment of area
$\hat{r}_2(S)$	Non-dimensional second moment of area
$\hat{r}_3(S)$	Non-dimensional third moment of area
$\hat{r}_2(m)$	Non-dimensional second moment of wing mass
R	Wing length. Also electrical resistance (Chapter 3)
Re	Reynolds number
S	Area
S_1	First moment of wing area for both wings
S_2	Second moment of wing area for both wings
S_3	Third moment of wing area for both wings
t	Time
T_{d}	Time spent on downstroke
T	Time for complete wingstroke wing stroke

U	Velocity of wing element
U_r	Relative velocity of air at a wing element
V	Velocity. Also Voltage (Chapter 3)
w	Induced air velocity
w_0	Vertical component of induced air velocity
α	Geometric angle of attack
α_r	Effective angle of attack
α_0	Zero lift angle of attack
α'	Angle of incidence
α'_r	Effective angle of incidence
β	Inclination of stroke plane
ε	Downwash angle
ϕ	Angular position of wing within stroke plane
$\bar{\phi}$	Mean angular position of wing within stroke plane
Φ	Wingstroke amplitude
η	Muscle efficiency
ν	Kinematic viscosity of air
π	Pi (=3.1416)
ρ	Density of air
τ	Proportion of time spent on downstroke
ω	Variable angular velocity
ω_{\max}	Maximum angular velocity
Ω	Angular velocity of propeller

Other superscripts and subscripts

*	(e.g. P^*_{aero}) Body-mass-specific
†	(e.g. P^\dagger_{aero}) Muscle-mass-specific
'	(e.g. L') per unit wing span
Early	(e.g. $C_{v,\text{Early}}$) before propeller wake developed
r	(e.g. c_r) relating to a wing element
Steady	(e.g. $C_{v,\text{Steady}}$) after propeller wake developed

A graphical description of relevant angles of attack and incidence



The effective angle of attack takes an account of the fact that some wing profiles can produce lift at zero geometric angle of attack. The 'zero lift' angle of attack α_0 is removed from the geometric angle of attack: $\alpha_r = \alpha - \alpha_0$. For flat profiles, α_0 tends to be very small.

The effective angle of incidence **also** takes into account the direction of the incident air

The black dotted line under the cambered wing chord represents the chord line against which α is taken. The grey dashed line (horizontal when $\alpha_r = 0$) represents the line against which the effective angle of attack α_r is taken.

Chapter 1: General introduction

Horizontal and slow flapping flight

Slow, flapping flight is used by many insects, birds and bats during landing (where low speeds minimise the risk of injury) and take-off (necessary unless a run-up or period of free-fall is possible). Less common, though still widespread, is the use of hovering flight. This enables both specialists and opportunists to utilise slow, localised or otherwise inaccessible food sources, and it is also a major component of many display flights in both insects and birds. Aerodynamic and energetic analyses of such flight have long been of interest to biologists, providing insights into muscle physiology (Casey, 1976; Wells, 1993; Dudley and Chai, 1996; Josephson, 1997a,b; Josephson and Ellington, 1997; Winter *et al.* 1998), and unconventional aerodynamics (see below). More recently, it has also become a subject of considerable research for engineers, due to funding from military bodies aiming to produce 'Micro Air Vehicles' for surveillance purposes (e.g. Greek, 1999; Shyy *et al.* 1999; Ellington, 1999; Ellington and Usherwood, in press).

Analyses of hovering animal flight

Vertical force balance

Conventional analyses of hovering animal flight are based on average coefficients derived from force measurements on wings in wind tunnels. They fail to account for the vertical force balance of hovering (Ellington, 1984a-e): calculated mean lifts are not great enough to oppose animal weight for various Diptera (Ennos, 1989a), bumblebees (Dudley and Ellington, 1990b), hawkmoths (Willmott and Ellington, 1997c) hummingbirds (Wells, 1993), long-eared bat (Norberg, U, 1976) or pied flycatcher (Norberg, U, 1975). Some difference between the airflow around flapping wings, and that experienced by wings in wind tunnels, must account for the incorrect balance of force coefficients. Flapping wings are different from wings in wind tunnels in four aspects: interaction, acceleration, rotation (supination and

pronation about the long wing-axis) and revolution (the rotation of the wing about the body axis, as with a propeller). The first three aspects are ‘unsteady’ phenomena, and have all been used as, at least partial, accounts for the high lift of flapping wings. Despite certain theoretical and experimental successes in analysing interaction (e.g. Weis-Fogh’s ‘clap and fling’: Lighthill, 1973; Weis-Fogh, 1973; Maxworthy, 1979), acceleration (Dickinson and Götz, 1993) and rotation (Dickinson, 1994) these phenomena, when considered alone, are unsatisfactory in accounting for weight support for the majority of hovering animals. Most hovering animals do not allow the wings to get close enough for a form of ‘clap and fling’ to be effective. Flow visualisation for accelerating and rotating model wings shows a large, unsteady leading-edge vortex which quickly breaks away, leading to stall, apparently making the phenomenon deleterious for insects with large stroke amplitudes or using forward-flight (Ellington, 1995).

Recent experiments based on flow observations over real (Willmott, 1995; Willmott *et al.* 1997) and mechanical model (Ellington *et al.* 1996; Van den Berg and Ellington, 1997a,b; Müller *et al.* in prep.) hawkmoth wings have discovered the presence of a ‘spiral’ leading-edge vortex over flapping wings. The leading-edge vortex (LEV) over flapping wings was observed to be caused by ‘delayed stall’ (not wing rotation), and stabilised by a strong spanwise flow. This results in a very tight, intense, spiralling vortex, capable of accounting for a considerable proportion of the overall lift, and strongly analogous to the leading-edge vortices over delta-wings (Van den Berg and Ellington, 1997b). Flow visualisations and force measurements on flapping model *Drosophila* wings (Dickinson *et al.* 1999) show rotation and wake capture (an unsteady effect due to interaction between the wing and its recent wake) also contribute to force production, and are particularly significant for manoeuvrability and control.

Power

Modern techniques for the analysis of the energetics of animal flight (e.g. Pennycuik, 1972, 1975; Rayner, 1979a-c; Ellington, 1984a-f) divide the mechanical power requirements into ‘parasite’, ‘induced’, ‘climbing’, ‘profile’ and ‘inertial’ powers (see Casey, 1981). Previous analyses of the profile power requirements of

slow and hovering flight must be questionable as they rely on profile drag coefficients derived largely from the same wind-tunnel experiments as were used in the determination of lift coefficients. For insects, an approximation given by Ellington (1984f) relating profile drag coefficient to Reynolds number has been used widely. For vertebrates, the general value (Rayner, 1979c; Pennycuick *et al.* 1992) of 0.02 is often taken for the profile drag coefficient. This study provides the first opportunity to derive appropriate profile drag coefficients for revolving wings experiencing ‘high-lift’, with attached leading-edge vortices.

Leading-edge vortices in engineering applications

Separation of flow at the leading edge of thin, swept- and delta-wings, appropriate for flight at high Mach numbers, results in the formation of leading-edge vortices. These are strongly analogous to those found over flapping hawkmoth wings (Van den Berg and Ellington, 1997b), and are used to provide high forces for landing and take-off in many delta-wing aircraft. Smoke flow visualisations of delta-wing LEVs shows a similar spiral structure (Werlé, 1963, see Fig. 1.1) and spanwise flow (‘jetting’ of the vortex core results in velocities up to three times higher than the free-stream velocity, Payne *et al.* 1988) to those over flapping wings. LEVs over delta-wings are associated with high force coefficients (both lift and drag) and allow remarkable incidences to be achieved before stall.

For moderately swept wings, the LEVs tend to curve inboard at the wing tips, and are not stable in position. This results in the loss of stability and control, as the control surfaces at the wing tips become ineffective. In order to delay the onset of LEVs over wings which usually operate under conventional, attached-flow conditions, a variety of wing features have been developed. Fig. 1.2 shows the wing of a Harrier GR3 standing at Duxford Imperial War Museum. It displays small wing fences, vortex generators and a sawtooth leading-edge. Structures such as the rocket pods, which protrude from the under-surface of the wing and only interfere with flow over the upper surface only at high angles of incidence, are termed ‘vortilons’ (see Barnard and Philpott, 1995). Each of these features shed trailing vortices over the upper surface of the wing, which serve to ‘scour’ the boundary layer over the upper

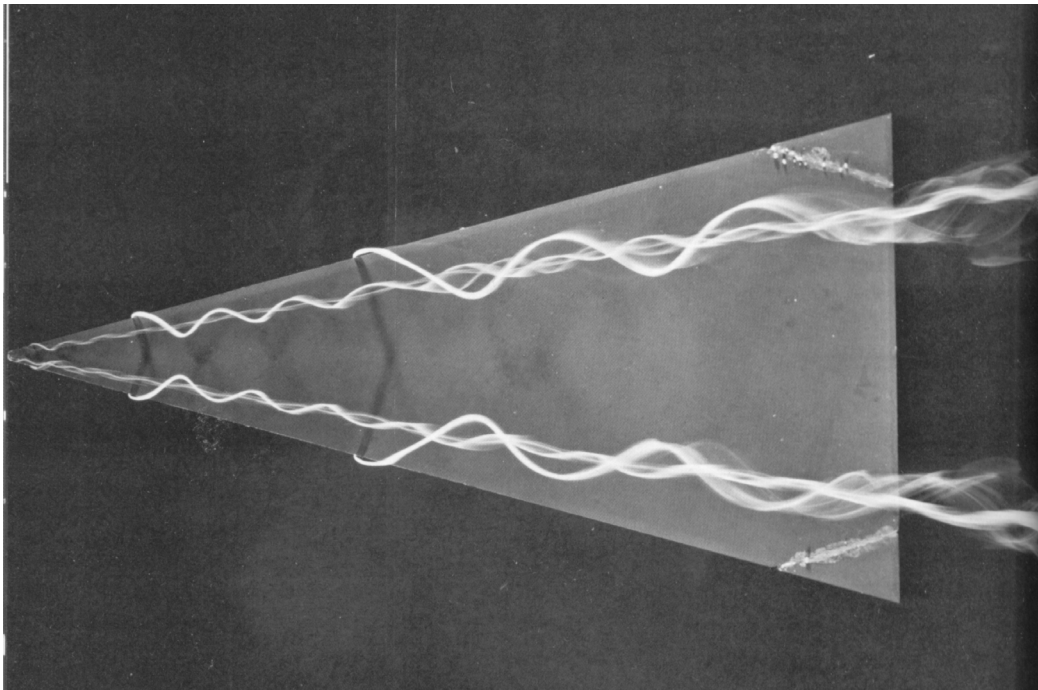


Fig. 1.1. Steady leading-edge vortices over a thin delta wing at a high incidence (Werlé, 1963).

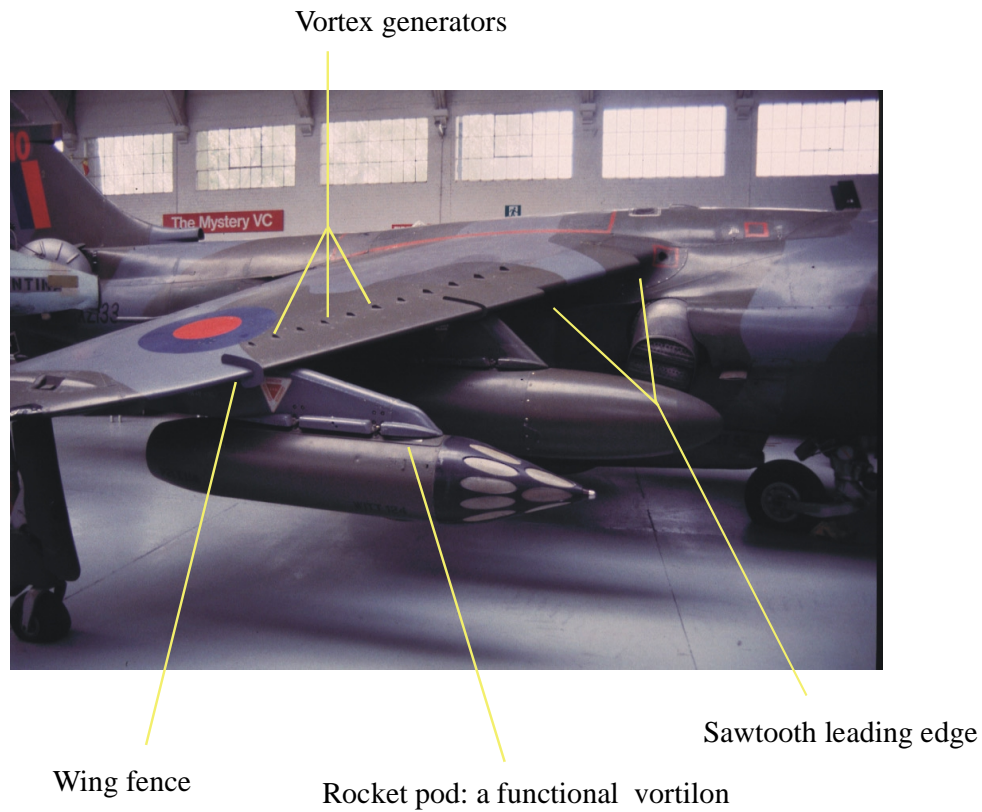


Fig. 1.2. A Harrier GR3 standing at Duxford Imperial War Museum. Structures that delay or control the development of leading-edge vortices are labelled.

wing surface, thus preventing spanwise boundary layer thickening, separation, and the creation of LEVs.

In general, helicopter rotors stall conventionally, and may be analysed with coefficients derived from steady, 2-dimensional flow conditions. However, swept rotor tips, such as the BERP design (British Experimental Rotor Programme, see Hopkins (1986)), make use of LEVs to delay stall, thus allowing higher incidences to be used, resulting in higher force coefficients.

Outline of the present study

The period of the down- or upstroke, away from pronation or supination, of an insect using a horizontal stroke plane for hovering, can be perceived as pure propeller-like revolution (Fig. 1.3). In order to study the aerodynamic properties of this period of the wing stroke in isolation from wing rotation or wing-wing interaction, propellers are developed to display the characteristics of model and real animal wings in simple revolution. Chapters 2 and 3 investigate the aerodynamics of animal-like wings in revolution, using smoke visualisation and force measurements on propellers. Chapter 2 focuses on wing models appropriate for a hovering hawkmoth *Manduca sexta*, testing the effects of leading-edge detail, camber, and twist on force production. The first profile drag coefficients appropriate for revolving wings operating with leading-edge vortices are presented. Chapter 3 extends the propeller force experiments to model and real quail wings, and model mayfly and bumblebee wings. The effect of aspect ratio on *Manduca* wing planforms is also investigated, allowing inferences to be made on the aerodynamics of the majority of flapping insects. Angles of attack tested range from -20° to $+100^\circ$, and so conclusions can also be drawn on the aerodynamics of animals using near-vertical stroke-planes.

Chapter 4 develops the ‘Normal force relationship’, found to be relatively unaffected by planform or induced velocity field in Chapters 2 and 3, into a new method for calculating power requirements for hovering flight. Morphological and kinematic parameters for a range of animals, including bumblebees and euglossine bees, hummingbirds, flycatcher and bats, are applied to these models. Possible energetic implications of unsteady mechanisms are also discussed.

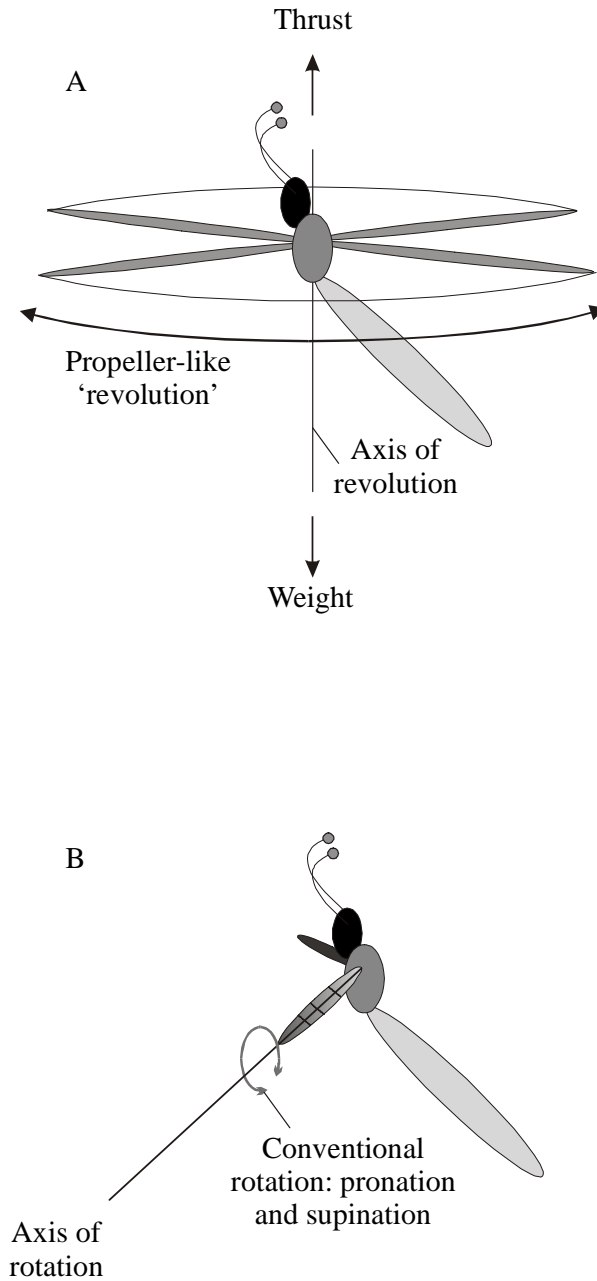


Fig. 1.3. Insects that hover with a horizontal stroke plane move their wings through periods of propeller-like revolution between start and end of each half-wingstroke (A). In studies of insect flight, the term 'rotation' (B), in studies of insect flight, refers to rotation about the long-axis of the wing, pronation and supination, which tend to occur at the ends of each halfstroke, when the wings are moving relatively slowly.

Chapter 2: The aerodynamics of revolving hawkmoth wings

Introduction

Recent experiments on the aerodynamics and forces experienced by model flapping insect wings have allowed great leaps in the understanding of the mechanisms of insect flight. ‘Delayed stall’ creates a ‘transient’ leading-edge vortex (LEV) that is maintained by spanwise flow, and apparently accounts for two-thirds of the required lift during the downstroke of a hovering hawkmoth (Ellington *et al.* 1996; Van den Berg and Ellington, 1997b). Maxworthy (1979) identified such a vortex during the ‘quasi-steady second phase of the fling’ in a flapping model, but its presence, and implications for lift production for insects using a horizontal stroke plane, have only been realised after the observations of smoke flow around tethered (Willmott *et al.* 1997) and mechanical (Van den Berg and Ellington, 1997a,b) hawkmoths. Additional mechanisms, ‘rotational circulation’ (referring to rotation about the pronation/supination axis) and ‘wake capture’, described for a model *Drosophila*, account for further details of force production, particularly important in control and manoeuvrability (Dickinson *et al.* 1999).

Experiments based on flapping models are the best way at present to investigate the unsteady and 3-dimensional aspects of flapping flight. The effects of wing-wing interaction, wing rotation about the supination/pronation axis, wing acceleration, and interactions between the wing and the induced flow-field, can all be studied with such models. However, flapping models inevitably confound some or all of these variables. In order to investigate the properties of the leading-edge vortex over ‘revolving’ wings, while minimising the confounding effect of these variables, this study is based on a propeller model. ‘Revolving’ from here on refers to the rotation of the wings about the body, as in a propeller. A propeller mimics, in effect, the steady phase of a down- (or up-) stroke.

The unusually complete kinematic and morphological data available for the hovering hawkmoth *Manduca sexta* (Willmott and Ellington, 1997b), along with its relatively large size, have made this an appropriate model insect for previous aerodynamic studies. This, and the potential for comparisons with computational (Liu

et al. 1998) and mechanical flapping models, both published and current (Müller, *et al.* in prep.), make Willmott's hovering hawkmoth an appropriate starting point for propeller experiments.

This study assesses the influences of leading-edge detail, twist, and camber on the aerodynamics of revolving wings. The similarities between the LEV over flapping wings, and those found over swept- and delta- wings operating at high incidences (Van den Berg and Ellington, 1997b), suggest that the detail of the leading-edge may be of interest (Lowson and Riley, 1995): the sharpness of the leading-edge is critical in determining the relationship between force coefficients and angle of attack. Protuberances from the leading-edge are used on swept-wing aircraft to delay or control the formation of leading-edge vortices (see Ashill *et al.* 1995, and Barnard and Philpott, 1995). Similar protuberances at a variety of scales exist on biological wings; from the fine sawtooth leading-edge of dragonfly wings (Hertel, 1966), to the adapted digits of birds (the alula), bats (thumbs), some, but not all, sea-turtles, and pterosaurs. The effect of a highly disrupted leading-edge is tested using a 'sawtooth' variation on the basic *Manduca* planform.

Willmott observed wing-twists of 24.5° (downstroke) to 19° (upstroke) in the hovering hawkmoth F1, creating higher angles of attack at the base than tip for both up- and down-stroke. Such twists are typical for a variety of flapping insects (e.g. Jensen, 1956; Norberg, Å, 1972; Weis-Fogh, 1973; Wootton, 1981; Ellington, 1984c), but this is not always the rule (Vogel 1967a; Nachtigall, 1979). The hawkmoth wings were also seen to be mildly cambered, agreeing with observations for a variety of insects: see, for instance, photographs by Dalton (1977) or Brackenbury (1992). Both of these features of insect wings have been assumed to provide aerodynamic benefits (e.g. Ellington, 1984c), and have been shown to be created by largely passive, but intricate, mechanical deflections (Wootton, 1981, 1991, 1992, 1993, 1995; Ennos, 1988).

Previous studies of the effects of camber have had mixed results. Camber on conventional aircraft wings increases the maximum lift coefficients, and normally improves the lift:drag ratio. This is also found to be true for locust (Jensen, 1956), *Drosophila* (Vogel, 1967b) and bumblebee (Dudley and Ellington, 1990b) wings. However, the effects of camber on unsteady wing performance appear negligible (Dickinson and Götz, 1993).

The propeller rig presented here enables the aerodynamic consequences of LEVs to be studied. It also allows the importance of various wing features, previously described by analogy with conventional aerofoil or propeller theory, to be investigated.

Materials and methods

The experimental propeller

A two-winged propeller (Figs 2.1 and 2.2) was designed and built to enable both the quantitative measurement of forces, and the qualitative observation of the flows experienced by propeller blades (or ‘wings’) as they revolve.

The shaft of the propeller was attached via a 64:1 spur gearbox to a 12V Escap DC motor/tachometer, driven by a servo with tacho feedback. The input voltage was ramped up over 0.8 seconds: a compromise between applying excessive initial forces (which may damage the torque strain gauges, and which set off unwanted mechanical vibrations) and achieving a steady angular velocity as quickly as possible. The voltage across the tachometer was sampled along with the force signals (see below) at 50Hz. Angular velocity during experiments was determined from the tacho signal, and so any small deviations in motor speed (e.g. due to higher torques at higher angles of attack) were accounted for.

The mean Reynolds number Re for a flapping wing is a somewhat arbitrary definition (e.g. Ellington 1984f, Van den Berg, 1997a), but it appears unlikely that Willmott’s hovering hawkmoths were operating anywhere near a critical value: both larger and smaller insects can hover in a fundamentally similar way. Because of this, and the benefits in accuracy when using larger forces, a fairly high rotational frequency (0.192Hz) was chosen, which results in a mean Reynolds number of 8071. While this is a little higher than that derived from Willmott’s data (7300) for F1 (the hawkmoth selected below for a ‘standard’ wing design) using Ellington’s conventions for flapping wings (1984f)

$$Re = \frac{4\Phi R^2 n}{\nu AR}, \quad (2.1)$$

where Φ is the wingstroke amplitude, n the flapping frequency, ν the kinematic viscosity of air, and AR the aspect ratio, it is certainly within the range of hovering hawkmoths.

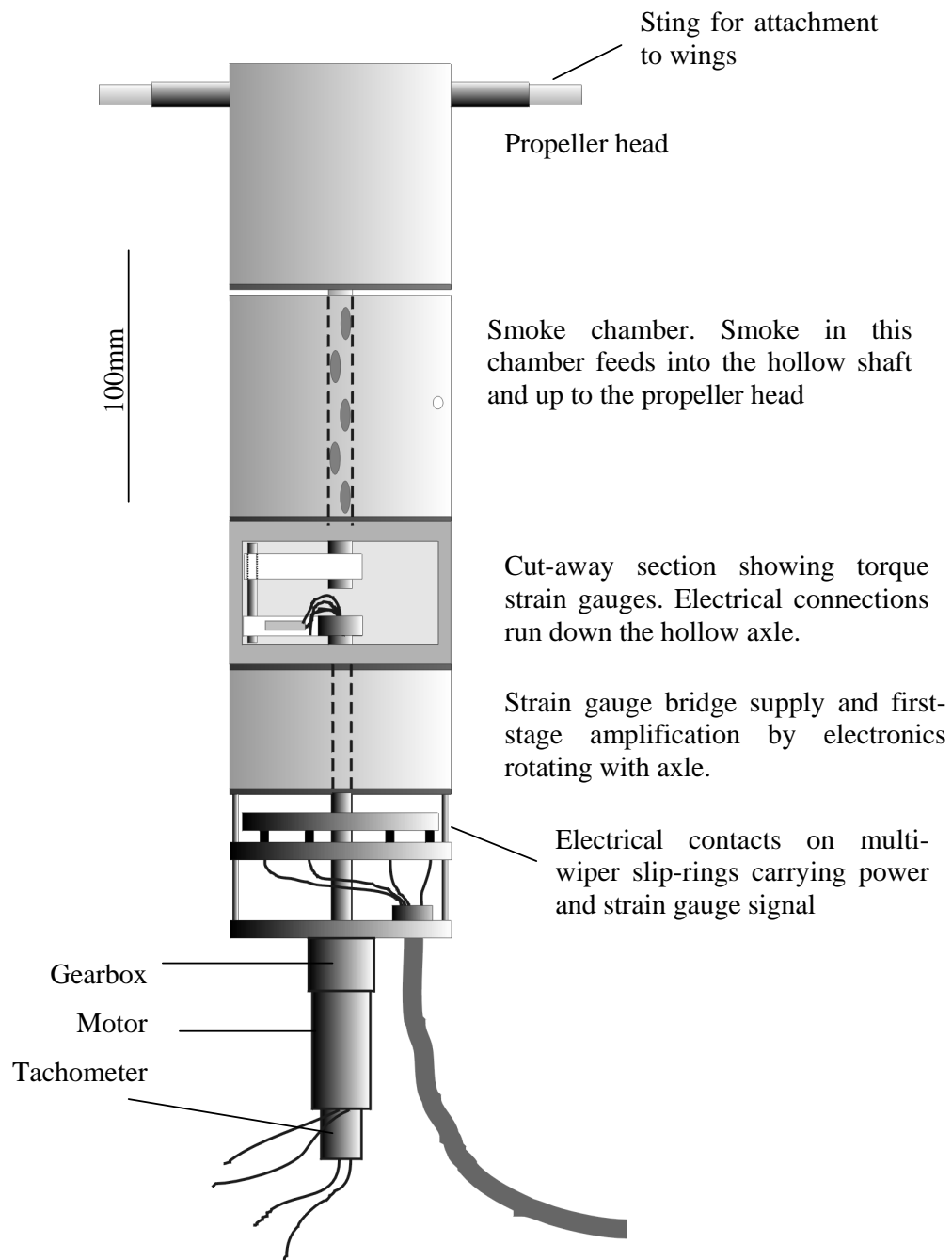


Fig. 2.2. Propeller body.

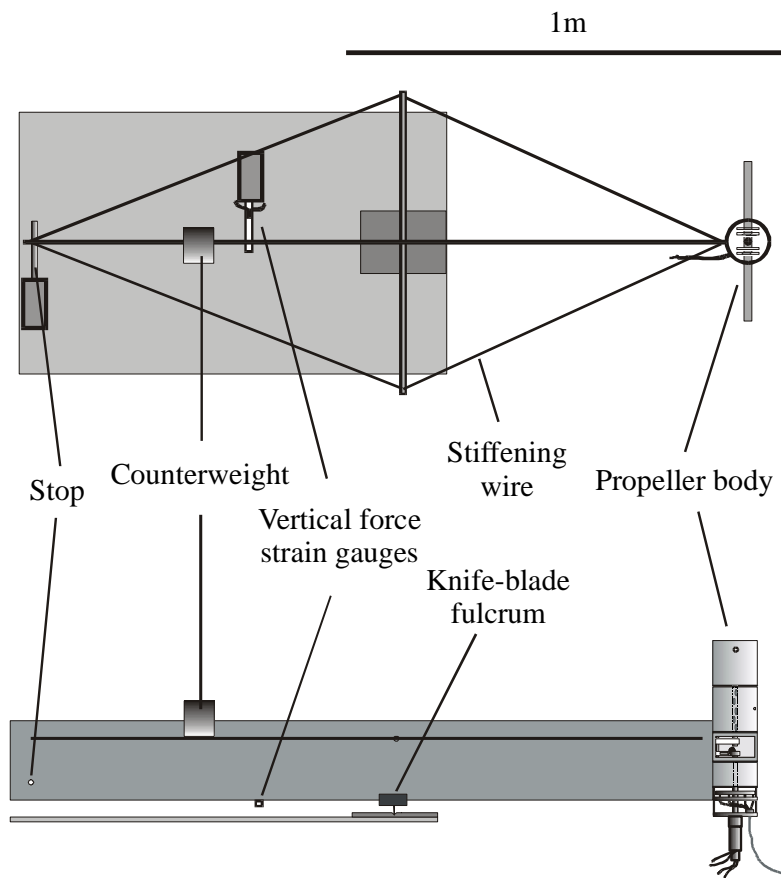


Fig. 2.3. Plan and side view of propeller rig.

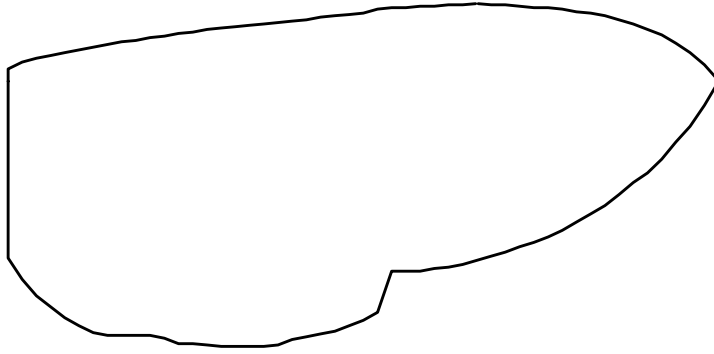
Wing design

The wings were constructed from 500×500×2.75mm sheets of black plastic ‘FLY-WEIGHT’ envelope stiffener. This material consists of two parallel, square, flat sheets sandwiching thin perpendicular lamellae which run between the sheets for the entire length of the square. The orientation of these lamellae result in hollow tubes of square cross-section running between the upper and lower sheets from leading to trailing edge. Together, this structure and material produces relatively stiff, light, thin, strong wing models.

The basic ‘*Manduca*’ wing planform was derived from a female hawkmoth ‘F1’ described by Willmott and Ellington (1997a,b), Fig. 2.3A. F1 was selected as the most representative, as its aspect ratio and radii for moments of area were the closest to the averages found from previous studies (Ellington, 1984b; Willmott and Ellington, 1997b). The wing was connected to the sting on the propeller head by a 2.4mm diameter steel rod running down a 20mm groove cut in the ventral surface of the wing. The groove was covered in tape, resulting in an almost flat surface barely protruding from the wing material. The rod also defined the angle of attack of the wing as it was gripped by grub-screws at the sting, and bent at right angles within the wing to run internally down one of the ‘tubes’ formed by the lamellae. Representative zero geometric angle of attack α was set by ensuring the base chord of each wing was horizontal. The rotation of each sting (about the pronation/supination axis) could be set independently in increments of 5° using a 72-tooth cog and pallet arrangement. The leading- and trailing- edges of the wings were taped, producing bluff edges less than 3mm thick. The wing thickness was less than 1.6% of the mean chord.

A

52.25mm (real) or 0.5m (model)



B

0.5m

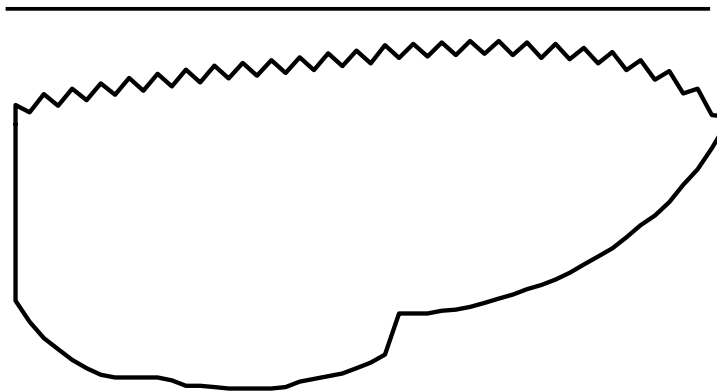


Fig. 2.3. Standard (A) and 'Sawtooth' (B) *Manduca* planforms.

Leading-edge range

Three variations on the basic, flat, *Manduca* wing model were constructed. ‘Sharp’ leading-edges were produced by sticking a 10mm border of 0.13mm brass shim to the upper surface of the leading-edge of standard *Manduca* wing models which had 10mm taken off the leading-edges. The converse of this, wings with ‘thick’ leading-edges, was achieved by using two layers of the plastic wing material, resulting in wings of double thickness. While this confounds leading-edge thickness and wing thickness, it allowed wings to be produced that had thick leading-edges without also distinct steps in upper or lower surface. The third design was of standard thickness and had a ‘sawtooth’ leading-edge of 45° pitch (Fig. 2.3B), with 10mm deep, 10mm long sawteeth.

Twist range

Twisted wing designs were produced by introducing a second 2.4mm diameter steel rod, which ran down the central groove, with bends at each end going perpendicularly down internal tubes at the wing base and near the tip. The two ends of the rod were out of plane, thus twisting the wing, creating a lower angle of attack at the tip than at the base. One wing pair had a twist of 15° between base and tip, while the second pair had 32°. No measurable camber was given to the twisted wings.

The wing material was weakened about the longitudinal axis of the wing by alternately slicing dorsal and ventral surfaces, which destroyed the torsion box construction of the internal ‘tubes’. This slicing was necessary to accommodate the considerable shear experienced at the trailing and leading edges, far from the twist axis.

Camber range

Standard *Manduca* wing models were heat-moulded to apply a camber. The wings were strapped to evenly-curved steel sheet templates and placed in an oven at 100°C for approximately one hour. The wings were then allowed to cool overnight.

The wings ‘uncambered’ to a certain extent on removal from the templates, but the radius of curvature remained fairly constant along the span and the reported cambers for the wings were measured *in situ* on the propeller. For thin wings, camber can be described as the ratio of wing depth to chord. One wing pair had a 7% camber over the basal half of the wing: cambers were less at the tip due to the narrower chord. The second wing pair had a 10% camber over the same region. The application of camber also gave a small twist of less than 6° for both wing models.

Wing moments

The basic wing shape used was a direct copy of the *Manduca* F1 planform except in the case of the sawtooth leading-edge design. However, the model wings do not revolve exactly about their bases: the attachment ‘sting’ and propeller head displace each base by 53.5mm from the propeller axis. Since the aerodynamic forces are influenced by both the wing area *and* its distribution along the span, this offset must be taken into account.

Table 2.1 shows the relevant wing parameters for aerodynamic analyses, following Ellington’s (1984b) conventions. The total wing area S (for two wings) can be related to the single wing length R and the aspect ratio AR :

$$S = \frac{4R^2}{AR}. \quad (2.4)$$

Aerodynamic forces and torques are proportional to the second and third moments of wing area, S_2 and S_3 respectively (Weis-Fogh, 1973). Non-dimensional radii corresponding to these moments are given by

$$\hat{r}_2(S) = \sqrt{\frac{S_2}{S R^2}} \quad (2.5)$$

and

$$\hat{r}_3(S) = \left(\frac{S_3}{S R^3} \right)^{\frac{1}{3}}. \quad (2.6)$$

Non-dimensional values are useful as they allow differences in wing shape to be identified while controlling for wing size.

Table 2.1. *Wing parameters for real and model Manduca wings*

	<i>Manduca</i> F1	Model <i>Manduca</i> with offset	Model sawtooth <i>Manduca</i> with offset
R (mm)	52.25	556	556
AR	5.66	6.34	6.33
$\hat{r}_2(S)$	0.511	0.547	0.547
$\hat{r}_3(S)$	0.560	0.588	0.588

The accuracy of the wing-making and derivation of moments was checked after the experiments by photographing and analysing the standard ‘Flat’ *Manduca* wing. Differences between the expected S_2 and S_3 for the model wings and those observed after production were less than 1%.

Smoke observations

Smoke visualisation was done independently from force measurements. Vaporised Ondina EL oil (Shell, UK) from a lab-built smoke generator was fed into a chamber of the propeller body, and from there into the hollow shaft. This provided a supply of smoke at the propeller head, even during continual revolution. Smoke was then delivered from the propeller head to the groove in the ventral surface of the wing by 4.25mm diameter Portex tubing. Smoke dispersed down the groove, down the internal wing ‘tubes’, and flowed out of the leading and trailing edges of the wing wherever the tape had been removed. Observations were made directly, or via a video camera mounted directly above the propeller. Photographs were taken using a Nikon DS-560 digital camera with 50mm lens. Lighting was provided by 1kW Arri and 2.5kW Castor spotlights. A range of rotational speeds was used: the basic flow properties were the same for all speeds, but a compromise speed was necessary. At high speeds the smoke spread too thinly to photograph, while at low speeds the smoke jetted clear of the boundary layer and so failed to label any vortices near the wing. A frequency of 0.1Hz was used for the photographs presented here.

Force measurements

Measurement of vertical force

The propeller body was clamped to a steel beam by a brass sleeve. The beam projected horizontally, perpendicular to the propeller axis, over a steel base plate (Fig. 2.2). The beam (1.4m long, 105mm deep and 5mm wide) rested on a knife-blade fulcrum, which sat in a grooved steel block mounted on the base-plate. Fine adjustment of the balance using a counterweight allowed the beam to rest gently on a steel shim cantilever with foil strain gauges mounted on upper and lower surfaces. The shim was taped firmly to the beam, and deflected in response to vertical forces acting on the propeller on the other side of the fulcrum due to the ‘see-saw’ configuration. The strain gauges were protected from excessive deflection by a mechanical stop at the end of the beam. Signals from these ‘vertical force’ strain gauges were amplified and fed into a Macintosh Quadra 650, using LabVIEW to sample at 50Hz. A range of masses (5g, 15g, 20g, 30g and 35g) was applied at the base of the propeller, directly in line with the propeller axis, to provide loads in order to determine the characteristics of the vertical force transducer (Fig. 2.4A). Responses were highly linear and showed little hysteresis. Five calibration measurements using a 5g mass were made before and after each experiment. The average coefficient of variation for each group of five measurements was less than 2%, and there was never a significant change between calibrations before and after each experiment.

The upper edge of the steel beam was sharpened underneath the area swept by the propeller wings in order to minimise aerodynamic interference. The beam was also stiffened by a diamond structure of cables, separated by a 10mm diameter aluminium tube sited directly over the fulcrum.

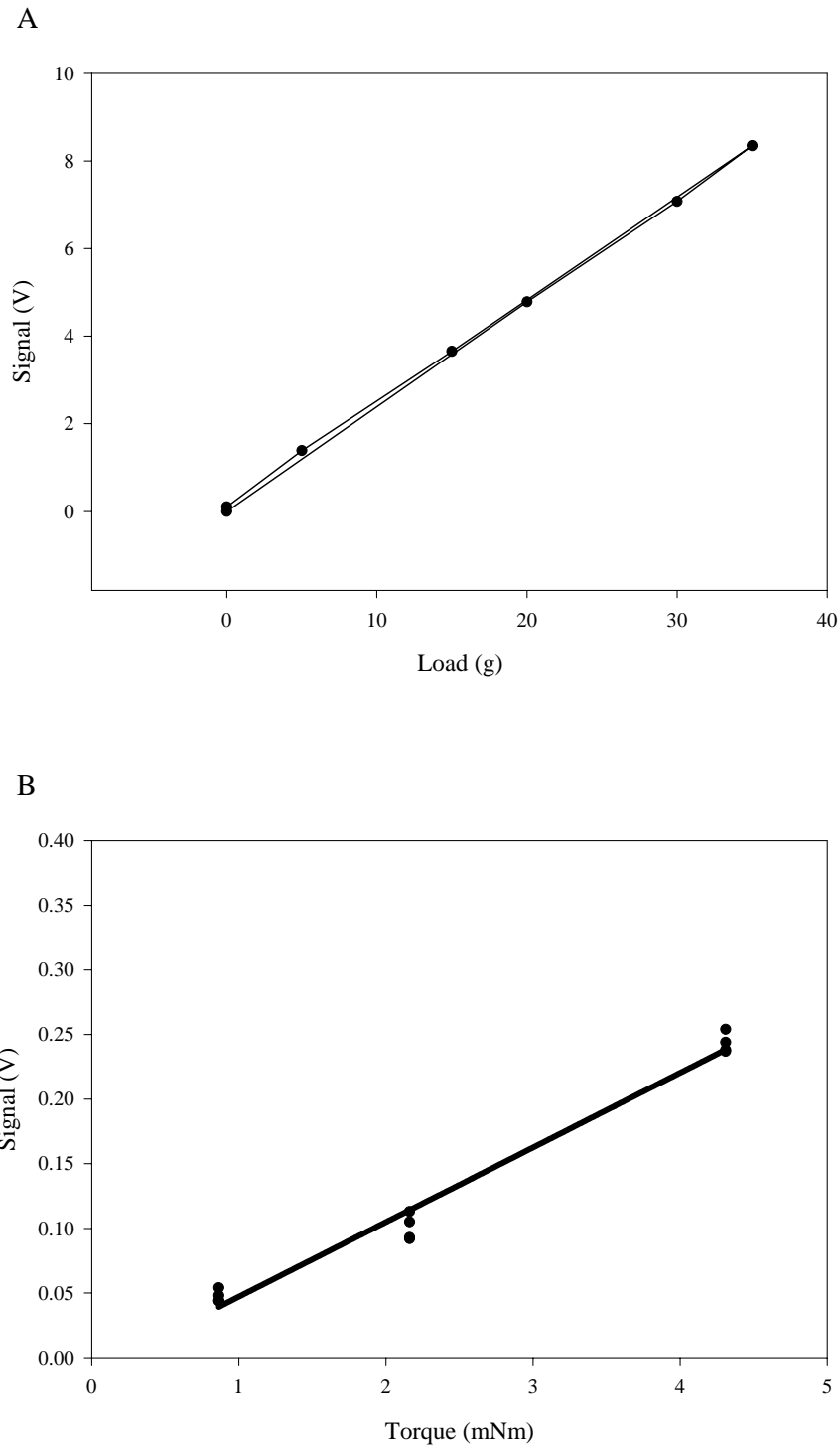


Fig. 2.4. Calibration responses for vertical force (A) and torque (B) transducers. Responses were highly linear in both cases; linear regression lines fit with r^2 of 0.9996 and 0.9804 for lift and torque responses respectively.

Measurement of torque

The torque Q required to drive the wings was measured via a pair of strain gauges mounted on a shim connected to the axle of the propeller (Fig. 2.5). The signal from these strain gauges was pre-amplified with revolving electronics also attached to the shaft, before passing through electrical slip-rings (through which the power supply also passed) machined from circuit board. The signal was then amplified again before being passed to the computer as with the vertical force signal.

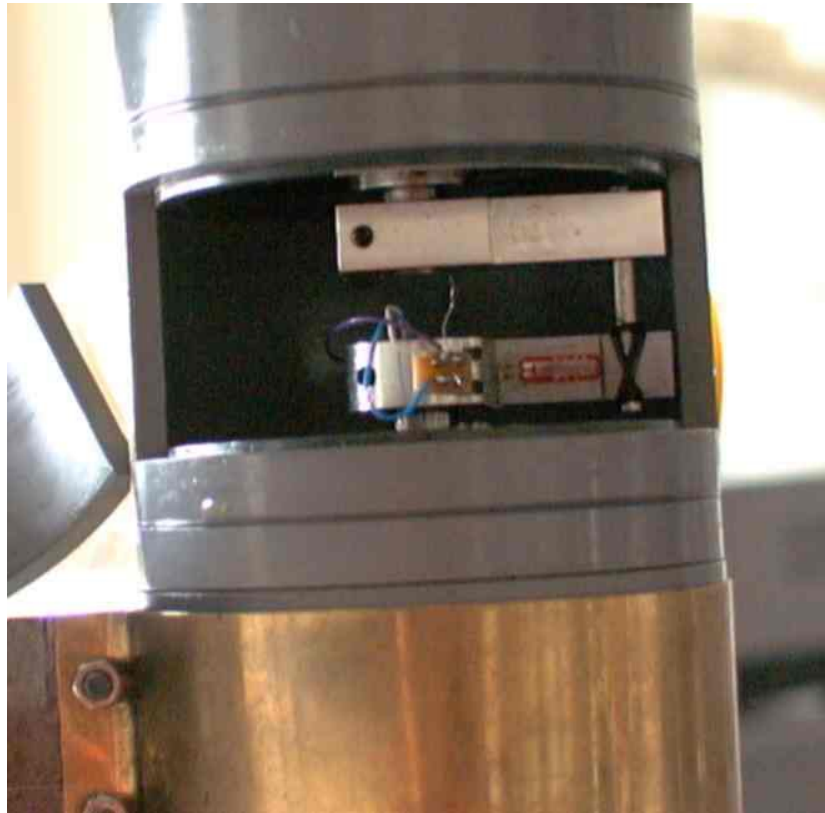


Fig. 2.5. Close-up of torque strain gauges.

The torque signal was calibrated before each experiment by applying a known torque: a 5 gram mass hung freely from a fine cotton thread, which passed over a pulley and wrapped around the propeller head. This produced a 49.1mN force at a distance of 44mm from the centre of the axle, and resulted in a calibration torque of 2.16mNm. This procedure was extremely repeatable, and showed no significant differences throughout the experiments. Five calibration readings were recorded before and after each experiment. The average coefficient of variation for each group of five measurements was less than 6%. The behaviour of the torque transducer was determined by applying a range of torques (0.864mNm, 2.16mNm and 4.31mNm) propeller head, directly perpendicular to the propeller axis. Responses (Fig. 2.4B) were highly linear and showed little hysteresis.

Torques due to friction in the bearings above the strain gauges, and to aerodynamic drag other than that caused by the wings, were measured by running the propeller without wings. This torque was subtracted from the measurements with wings, giving the torque due to the wing-drag only.

Experimental protocol

Each wing type was tested twice for a full range of angles of attack from -20° to $+95^\circ$ with 5° increments, and three times using an abbreviated test, covering from -20° to $+100^\circ$ in 20° increments. Four runs were recorded at each angle of attack, consisting of approximately 10s before the motor was turned on, followed by 20s after the propeller was started. The starting head-positions for these four runs were incremented by 90° , and pairs of runs started at opposite positions were averaged to cancel any imbalance in the wings. Overall, -20° , 0° , 20° , 40° , 60° and 80° had 10 independent samples each, 100° had 6, and all the other angles of attack had 4.

Data processing

Once collected, the data was transferred to a 400 MHz Pentium II PC and analysed in LabVIEW. Fig. 2.6 shows a typical trace for a single run. The top (green) trace shows the tacho signal, with the wing stationary for the first 10s. The middle (blue) trace shows the torque signal: a very large transient is produced as the torque overcomes the inertia of the wings, and then the signal settles down. The bottom (red) trace shows the vertical force signal. The rise in the tacho signal was used to identify the start of wing movement. Zero-values for the force signals were defined as the means before the wings started moving, and from then on signal values were taken relative to their zeroes.

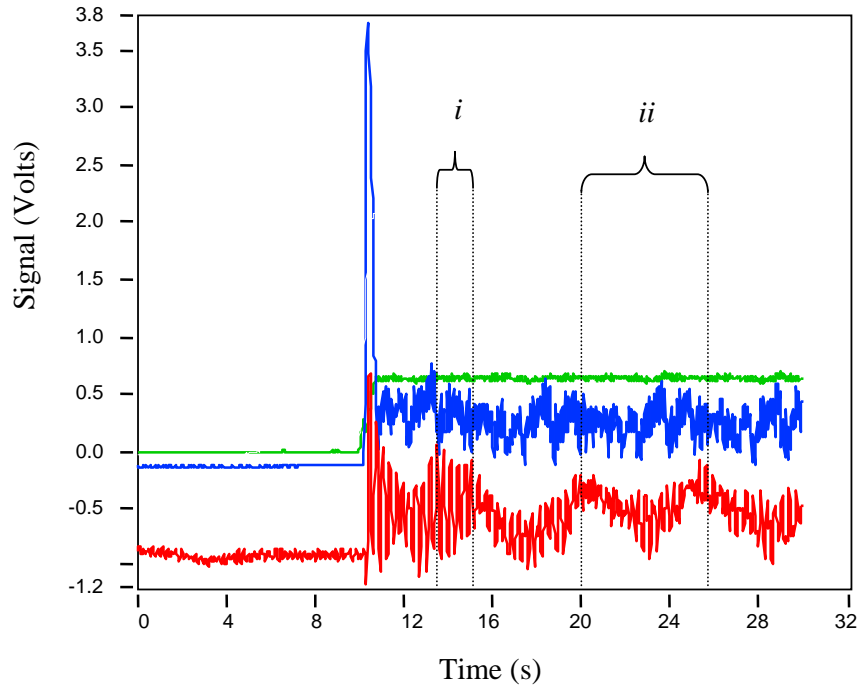


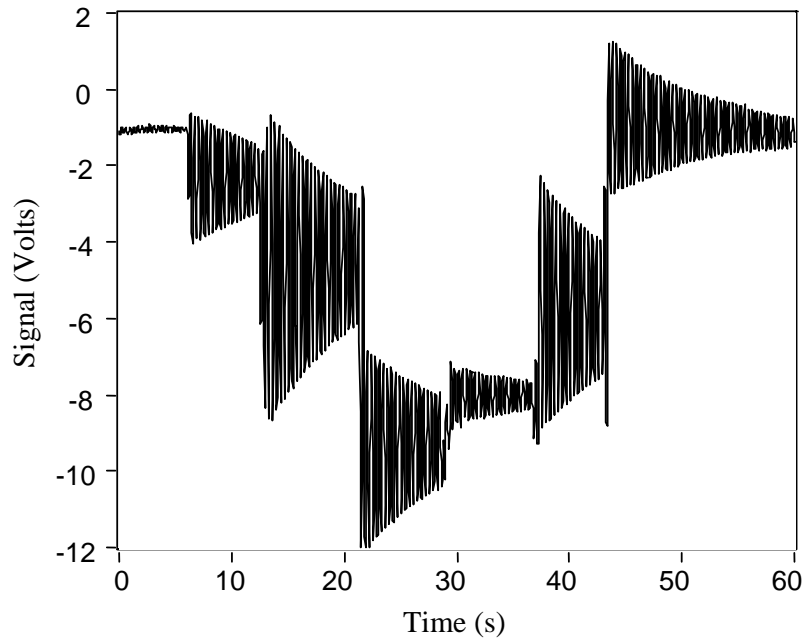
Fig. 2.6. Typical voltage signals for a single run at high α . The top (green) line shows tachometer trace, middle (blue) line the torque signal, and bottom (red) line the vertical force signal. Periods of 5 major oscillations in the vertical force trace (*i*) and imbalance over one complete revolution (*ii*) are marked with dotted lines.

Filtering

Force and torque signals were low-pass filtered at 6Hz using a FIR filter. Large-amplitude oscillations persisted in the vertical force signal. These are due to the massive propeller and beam resting on the vertical force strain gauge shim, thus producing a lightly-damped mass-spring system. The magnitude of the oscillation was so great that conventional low-pass or band-stop filtering proved inadequate without unacceptably compromising the frequency response. However, a simple physical argument allows this oscillation to be removed effectively. A moving average, taken over the period of oscillation, comprises only the aerodynamic force and the damping force: mean inertial and spring forces are zero over a cycle. When the damping force is negligible this method will yield the mean aerodynamic force with a temporal resolution on the order of the oscillation period. This filtering technique was tested on a signal created by the addition and removal of a range of masses to the propeller head (Fig. 2.7). The removal of the oscillation from the signal was highly effective (Fig. 2.7B), and the full change in signal was observed after a single oscillation period (0.32s) had passed. This ‘step’ change corresponded to the static calibration of the vertical strain gauge, confirming that the damping force was indeed negligible. The longer-period oscillation visible in the vertical force signal trace (Fig. 2.6) is due to a slight difference in mass between the wings. The effect of this imbalance is cancelled by averaging runs started in opposite positions.

A similar filtering technique was used on the torque signal. Unlike the vertical force signal, however, several modes of vibration were observed. A large filter window size (1.28s) was needed to remove the dominant mode, but resulted in a poorer temporal resolution (equivalent to approximately a quarter-revolution).

A



B

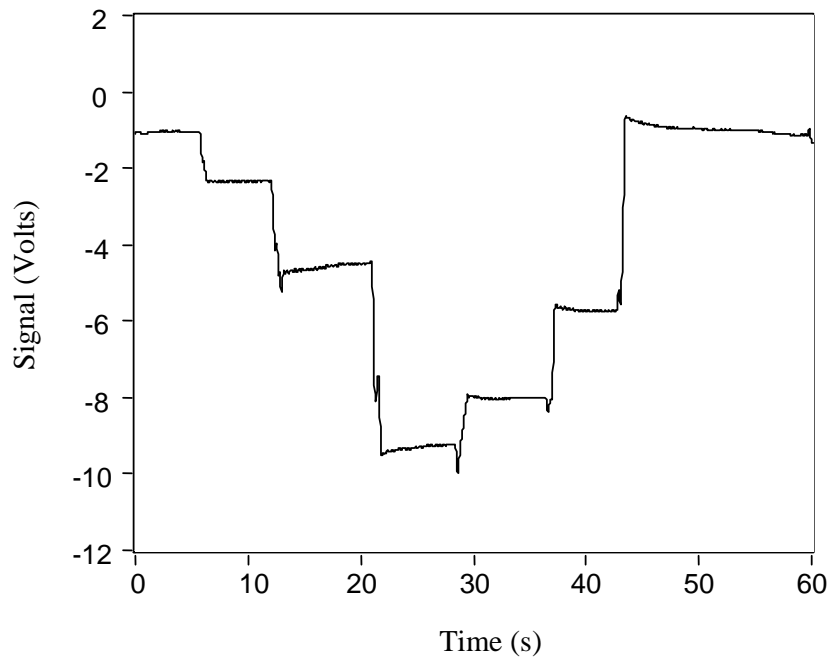


Fig. 2.7. Vertical force signal (Volts) over time with the addition, and then removal, of 5g, 10g, and 20g before (A) and after (B) filtering.

Pooling the data into 'Early' and 'Steady'

The filtered data for each angle of attack was pooled into 'Early' or 'Steady' classes. 'Early' results were averaged force coefficients relating to the first half-revolution of the propeller, between 60° and 120° from the start of revolution; from 1.5 to 3.1 chord-lengths of travel of the middle of the wing. This discarded the initial transients, and ensured that the large filter window for the torque signal did not include any data beyond 180° . *A priori* assumptions were not made about the time course for development of the propeller wake, so force results from between 180° and 450° from the start of revolution were averaged, and form the 'Steady' class. The large angle over which 'Steady' results were averaged, and the relative constancy of the signal for many revolutions (Fig. 2.8) suggest that the 'Steady' results are close to those that would be found for propellers that have achieved steady-state revolution, with a fully developed wake. However, it should be noted that brief high (or low), dynamic, and biologically significant forces, particularly during very early stages of revolution, are not identifiable with the 'Early' pooling technique.

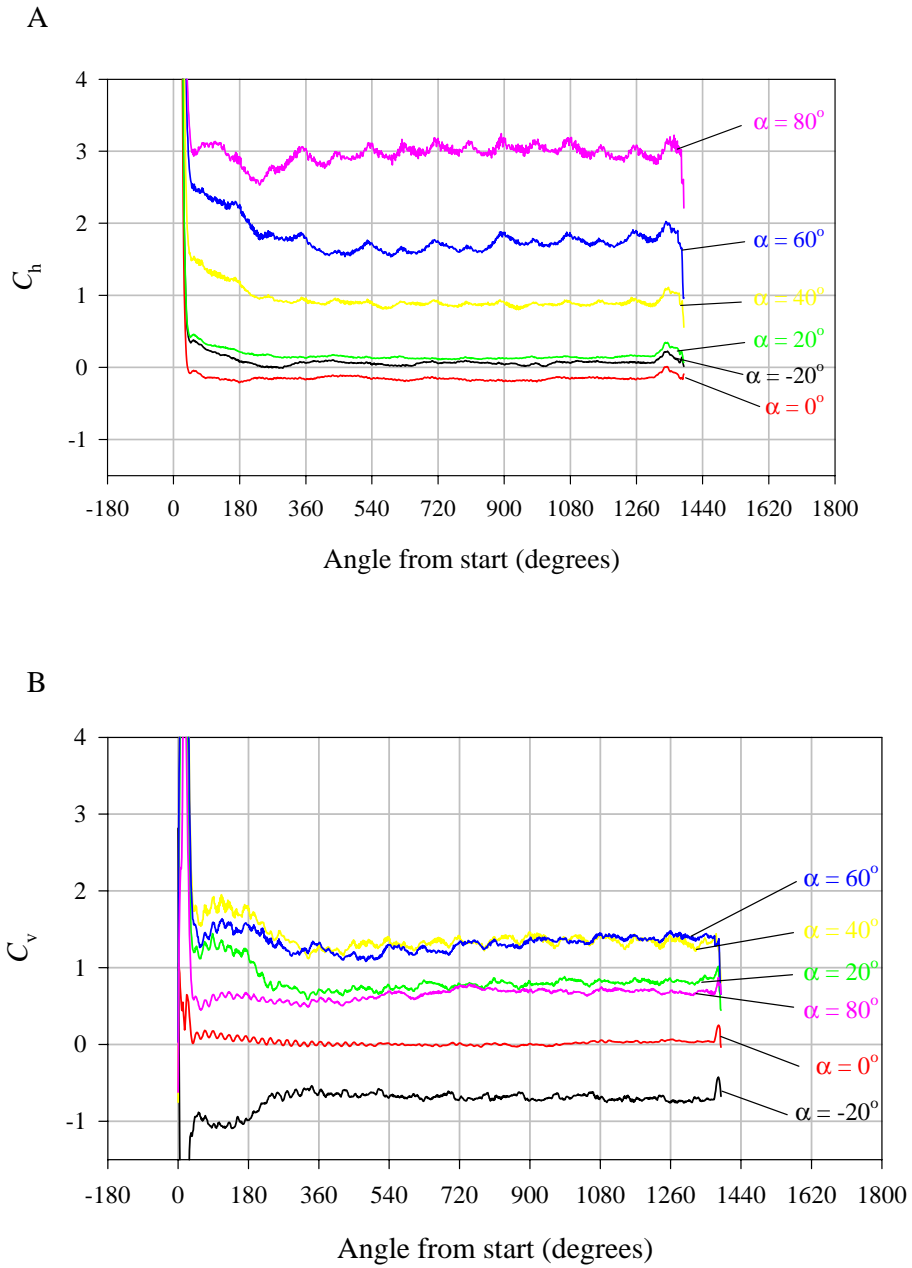


Fig. 2.8. Averaged horizontal (A) and vertical (B) force coefficients against angle of revolution for standard *Manduca* wings over the ‘abbreviated’ range of α .

Coefficients

Conversion into ‘propeller coefficients’

Calibrations before and after each experiment were pooled and used to convert the respective voltages to vertical forces (N) and torques (Nm). ‘Propeller coefficients’ analogous to the familiar lift and drag coefficients will be used for a dimensionless expression of vertical and horizontal forces F_v and F_h , respectively: lift and drag coefficients are not used directly, as they must be related to the direction of the oncoming air (see below).

The vertical force on an object, equivalent to lift if the incident air is stationary, is given by

$$F_v = \frac{\rho}{2} C_v S V^2 \quad (2.7)$$

where ρ is the density of air (taken to be 1.2kgm^{-3}), C_v is the vertical force coefficient, S is the area and V is the velocity of the object. A pair of revolving wings may be considered as consisting of many objects, or ‘elements’. Each element, at a position r from the wing base, with width dr and chord c_r , has an area $c_r \times dr$, and a velocity U given by

$$U = \Omega r \quad (2.8)$$

where Ω is the angular velocity (in radians per second) of the revolving wings.

The ‘mean coefficients’ method of blade-element analysis (first applied to flapping flight by Osborne, 1951) supposes that a single mean coefficient can represent the forces on revolving and flapping wings. So, the form of equation (2.7) appropriate for revolving wings is

$$F_v = 2 \frac{\rho}{2} C_v \sum_{r=0}^{r=R} c_r dr (\Omega r)^2. \quad (2.9)$$

The initial factor of 2 is to account for both wings. Ω is a constant for each wing element, and so equation (2.9) can be written

$$F_v = \frac{\rho}{2} \Omega^2 C_v \left[2 \sum_{r=0}^{r=R} c_r r^2 dr \right] \quad (2.10)$$

The bracketed term is a purely morphological parameter, the second moment of area S_2 of both wings (see Ellington, 1984b). From these expressions, the mean vertical force coefficient can be derived:

$$C_v = \frac{2 F_v}{\rho S_2 \Omega^2} \quad (2.11)$$

The mean horizontal force coefficient C_h can be determined in a similar manner. The horizontal forces (equivalent to drag if the relative air motion is horizontal) for each wing element act about a moment arm of distance r from the wing base, and combine to produce a torque Q . Thus, the equivalent of equation (2.10) uses a cubed term for r :

$$Q = \frac{\rho}{2} \Omega^2 C_h \left[2 \sum_{r=0}^{r=R} c_r r^3 dr \right] \quad (2.12)$$

In this case the bracketed term is the third moment of wing area S_3 for both wings. The mean horizontal force coefficient C_h is given by

$$C_h = \frac{2 Q}{\rho S_3 \Omega^2} \quad (2.13)$$

Coefficients derived from these propeller experiments, where the wings revolve instead of translate in the usual rectilinear motion, are termed here as ‘propeller coefficients’.

Conversion into conventional profile drag and lift coefficients

If the motion of air about the propeller wings can be calculated, then the steady propeller coefficients can be converted into conventional coefficients for profile drag $C_{D,pro}$ and lift C_L . The propeller coefficients for ‘Early’ conditions provide a useful comparison for the results of these conversions; the induced downwash of the propeller wake has hardly begun, so $C_{h,Early}$ and $C_{v,Early}$ approximate $C_{D,pro}$ and C_L . However, wings in ‘Early’ revolution do not experience completely still air; some downwash is produced even without the vorticity of the fully developed wake. Despite this, $C_{h,Early}$ and $C_{v,Early}$ provide the best direct (though under-) estimates of $C_{D,pro}$ and C_L for wings in revolution.

Consider the wing-element shown in Fig. 2.9 which shows the forces (where the prime denotes forces per unit span) acting on an element in the two frames of reference. A downwash air velocity results in a rotation of the ‘lift / profile drag’ from

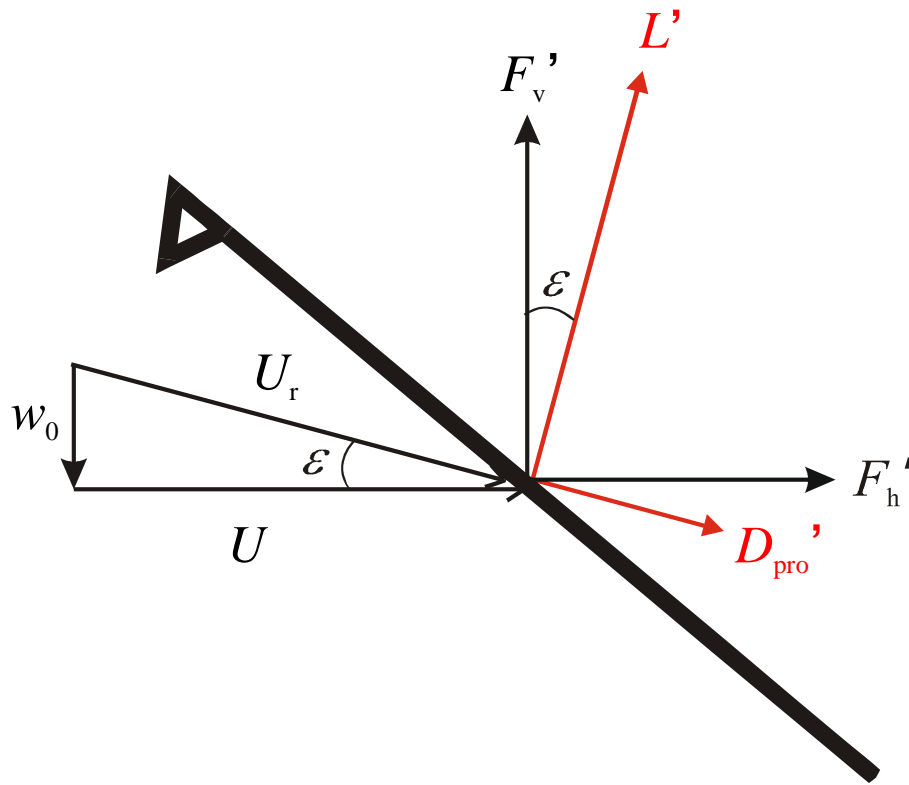


Fig. 2.9. Construction for the derivation of lift and profile drag.

‘vertical / horizontal’ frame of reference by the downwash angle ε . In the ‘lift / profile drag’ frame of reference, a component of profile drag acts downwards. Also, a component of lift acts against the direction of motion; this is conventionally termed ‘induced drag’. A second aspect of the downwash is that it alters the appropriate velocities for determining coefficients; C_h and C_v relate to the wing speed, whereas $C_{D,pro}$ and C_L relate to the local air speed.

If a ‘triangular’ downwash distribution is assumed (which is reasonable, and the analysis is not very sensitive to the exact distribution, see Stepniewski and Keys, 1984), with local vertical downwash velocity w_0 proportional to spanwise position along the wing r , then there is a constant downwash angle ε for every wing chord. The mean downwash velocity $\overline{w_0}$ across a Froude ‘actuator disc’ (the area swept by the wings, πR^2) can be determined using a ‘Rankine-Froude’ approach following Ellington’s (1984e) formulation. The mean pressure exerted by this disc is assumed to be steady with time, and this causes a downward acceleration of the air that continues for some distance below the disc because of the high pressure in the accelerated air (‘jet’). The jet pressure gradually returns to atmospheric far below the disc, and the air velocity then remains constant. Using Bernoulli’s equation, the Rankine-Froude theory shows that the mean vertical velocity \overline{w} finally attained in the ‘far’ wake is twice the mean induced velocity $\overline{w_0}$ at the disc: $\overline{w} = 2\overline{w_0}$. Furthermore, continuity of flow requires that the volume of air passing through the far wake per unit time equals that flowing through the disc, so the far wake area A must be half that of the disc. The momentum equation for fluids may be applied to the far wake, and it gives the force F required to generate a steady flow of velocity \overline{w} over an area A as

$$F = \rho \overline{w}^2 A. \quad (2.14)$$

This simply equates the force F to the rate of change of momentum of the jet, which is equal to the product of mass flow, $\rho \overline{w} A$, and velocity \overline{w} . Equation (2.14) may be rewritten in terms of $\overline{w_0}$ and πR^2 using the relations above and, when equated to the vertical force F_v , the unknown mean induced velocity can then be found:

$$\overline{w_0} = k_{ind} \sqrt{\frac{F_v}{2\rho\pi R^2}}. \quad (2.15)$$

A correction factor k_{ind} is also included to account for non-uniform (both spatially and temporally) downwash distributions. $k_{ind} = 1.2$ is used in this study (following

Ellington, 1984e) but, again, the exact value is not critical. The local induced downwash velocity, given the triangular downwash distribution and maintaining the conservation of momentum, is given (Stepniewski and Keys, 1984) by

$$w_0 = \frac{\overline{w_0} r \sqrt{2}}{R}, \quad (2.16)$$

and so the value of w_0 appropriate for the wing tip is $\overline{w_0} \sqrt{2}$. Given the wing velocity at the tip is ΩR , the downwash angle ε is given by

$$\varepsilon = \tan^{-1} \left(\frac{\overline{w_0} \sqrt{2}}{\Omega R} \right). \quad (2.17)$$

If small angles are assumed, then the approximations

$$C_{D,\text{pro}} \approx C_h \cos(\varepsilon) \quad (2.18)$$

and

$$C_L \approx C_v \cos(\varepsilon) \quad (2.19)$$

may be used. However, these approximations can be avoided: it is clear from Fig. 2.9 that the forces can be related by

$$F'_h = L' \sin(\varepsilon) + D'_{\text{pro}} \cos(\varepsilon) \quad (2.20)$$

and

$$F'_v = L' \cos(\varepsilon) - D'_{\text{pro}} \sin(\varepsilon). \quad (2.21)$$

From these,

$$D'_{\text{pro}} = F'_h \cos(\varepsilon) - F'_v \sin(\varepsilon) \quad (2.22)$$

and

$$L' = F'_v \cos(\varepsilon) + F'_h \sin(\varepsilon). \quad (2.23)$$

The appropriate air velocities for profile drag and lift coefficients may be described conveniently as proportions of the wing velocity. In simple propeller theories, a vertical downwash is assumed, and the local air velocity U_r at each element, as a proportion of the velocity of the wing-element U , is given by

$$\frac{U_r}{U} = \frac{1}{\cos(\varepsilon)}. \quad (2.24)$$

More sophisticated propeller theories postulate that the induced velocity is perpendicular to the relative air velocity U_r , because that is the direction of the lift

force and hence the direction of momentum given to the air. A ‘swirl’ is therefore imparted to the wake by the horizontal component of the inclined induced velocity. Estimating the induced velocity, ε , and U_r then becomes an iterative process because they are all coupled, but for small ε we can use the approximate relation

$$\frac{U_r}{U} \approx \cos(\varepsilon): \quad (2.25)$$

i.e. the relative velocity is slightly smaller than U , whereas the assumption of a vertical downwash makes it larger than U .

Given the rotation of the frames of reference described in equations (2.22) and (2.23), and the change in relevant velocities discussed for equations (2.24) and (2.25), profile drag and lift coefficients can be derived from ‘steady’ propeller coefficients:

$$C_{D,pro} = \left(C_{h,Steady} \cos(\varepsilon) - C_{v,Steady} \sin(\varepsilon) \right) \left(\frac{U}{U_r} \right)^2 \quad (2.26)$$

and

$$C_L = \left(C_{v,Steady} \cos(\varepsilon) + C_{h,Steady} \sin(\varepsilon) \right) \left(\frac{U}{U_r} \right)^2 \quad (2.27)$$

Display of results

Angle of incidence

The definition of a single geometric angle of attack α is clearly arbitrary for cambered and twisted wings, so angles were determined with respect to a zero-lift angle of attack α_0 . This was found from the x-intercept of a regression of ‘Early’ C_v data ($C_{v,Early}$) against a range of α from -20° to $+20^\circ$. The resulting angles of incidence, $\alpha' = \alpha - \alpha_0$, were thus not pre-determined; the experimental values were not the same for each wing type, although the increment between each α' within a wing type is still 5° . The use of angle of incidence allows comparison between different wing shapes without any bias introduced by an arbitrary definition of geometric angle of attack.

Determination of significance of differences

Because the zero lift angle differs slightly for each wing type, the types cannot be compared directly at a constant angle of incidence. Instead, it is useful to plot the relationships between force coefficients and angles with a line width of +/- one mean standard error: this allows plots to be distinguished and, at these sample sizes (and assuming parametric conditions are approached), the lines may be considered different if (approximately) a double line thickness would not overlap. The problems of sampling in statistics should be remembered, so occasional deviations greater than this would be expected without any underlying aerodynamic cause.

Results

Force results

Typical changes of force coefficient with angle of revolution

Fig. 2.8 shows variations in propeller coefficients with the angle of revolution for standard 'flat' *Manduca* wings over the 'abbreviated' range of angles. Each line is the average of 6 independent samples at the appropriate α .

Standard Manduca

Fig. 2.10 shows C_h and C_v against α' for the standard flat *Manduca* model wing pair. The minimum C_h is not significantly different from zero and is, in fact, slightly negative. This illustrates limits to the accuracy of the measurements. Significant differences are clear between 'Early' and 'Steady' values for both vertical and horizontal coefficients over the mid-range of angles. Maximal values of C_h occur at α' around 90° , and C_v peaks between 40° and 50° . The error bars shown (+/- 1 S.E.) are representative for all wing types.

In the following Fig.s, 2.11 to 2.13, these standard *Manduca* results are included as an under-lying grey line, and represent 0° twist and 0% camber.

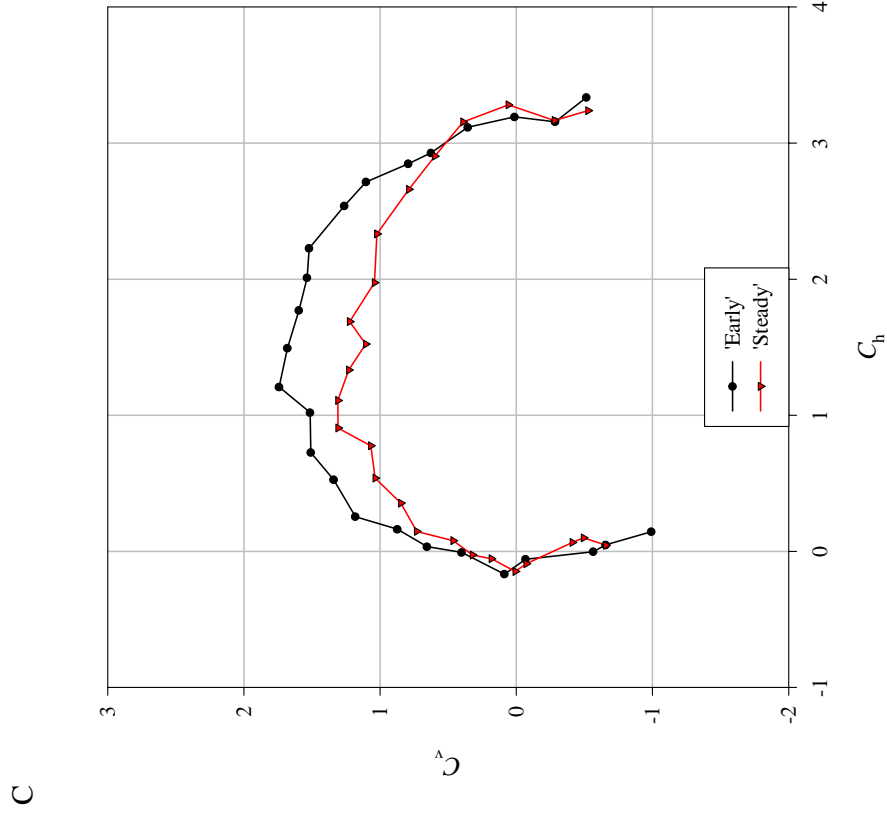
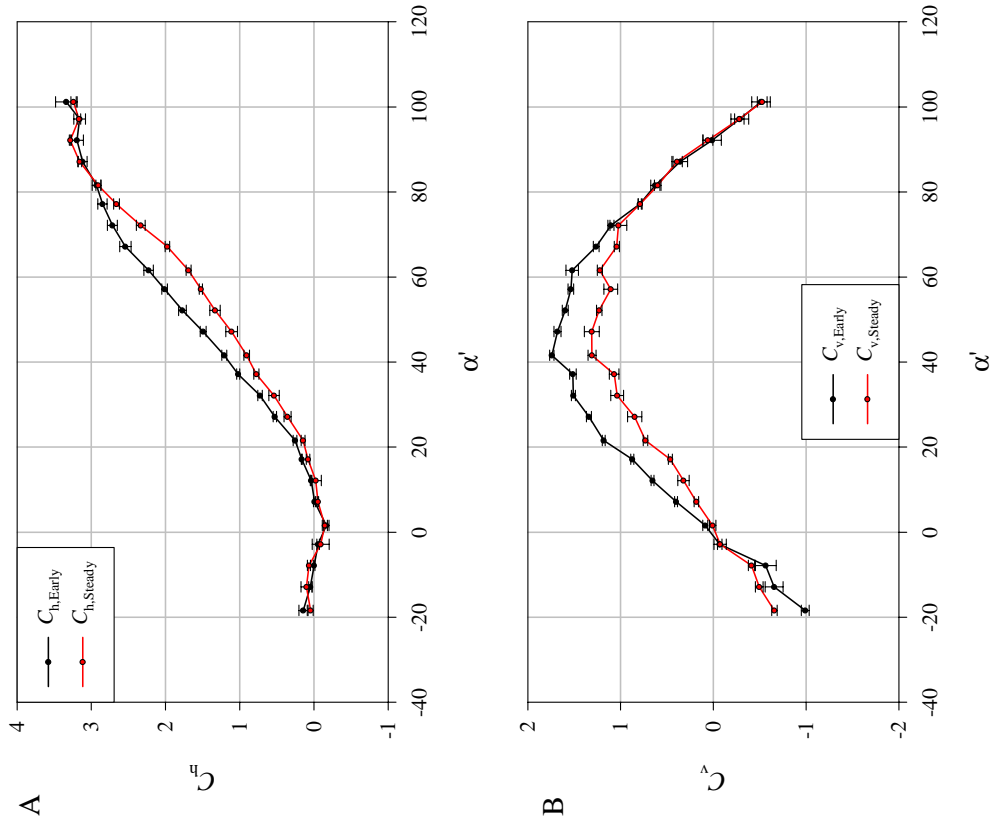


Fig. 2.10. Horizontal (A) and vertical (B) force coefficients, and the polar diagram (C), for Standard *Manduca* wings under 'Early' and 'Steady' conditions. Error bars in (A) and (B) show ± 1 standard error.

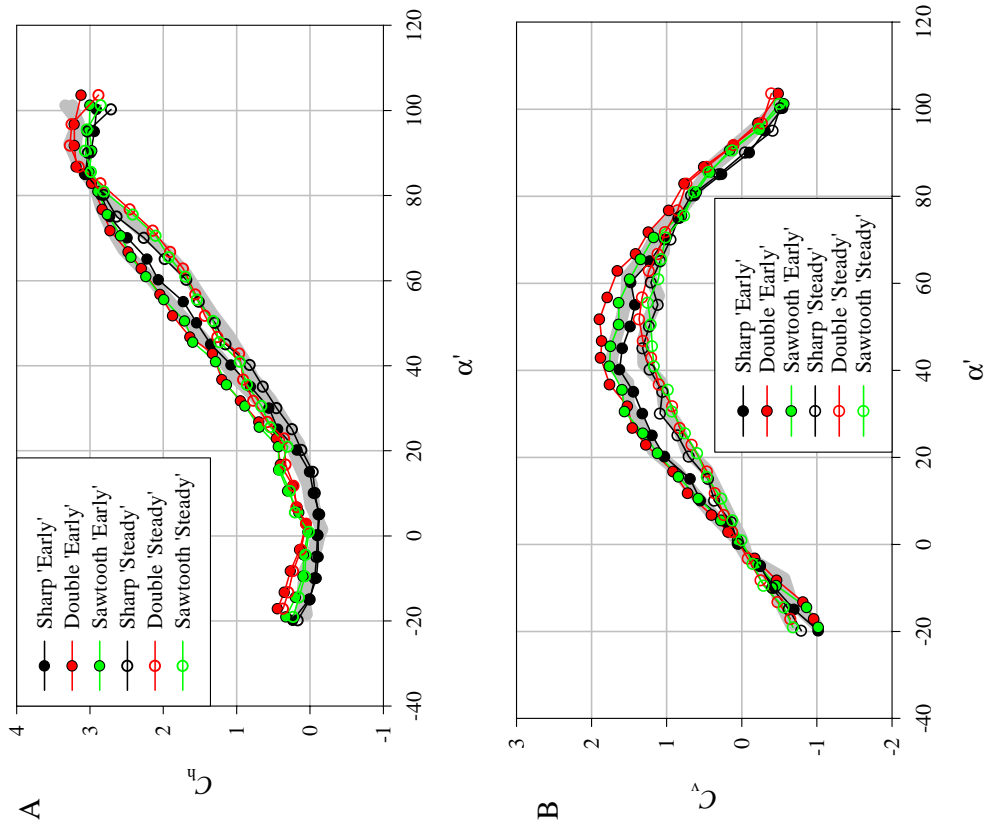


Fig. 2.11. Horizontal (A) and vertical (B) force coefficients, and the polar diagram (C), for the 'Leading-edge' range under 'Early' and 'Steady' conditions. Underlying grey lines show 'Early' (higher) and 'Steady' (lower) values for standard *Manduca* wings.

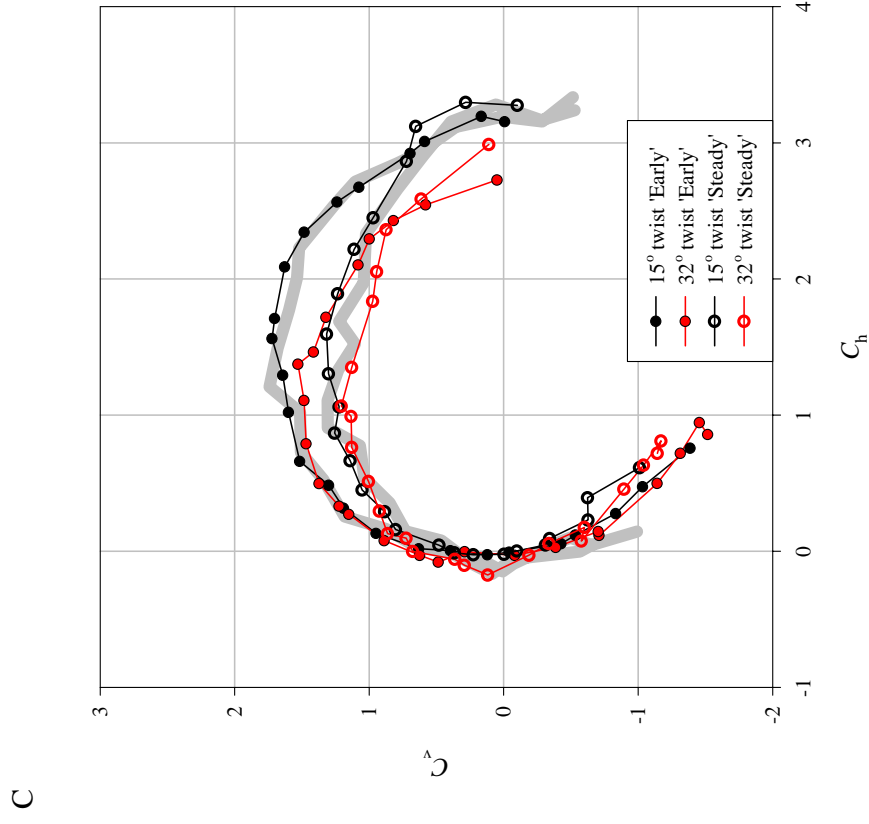
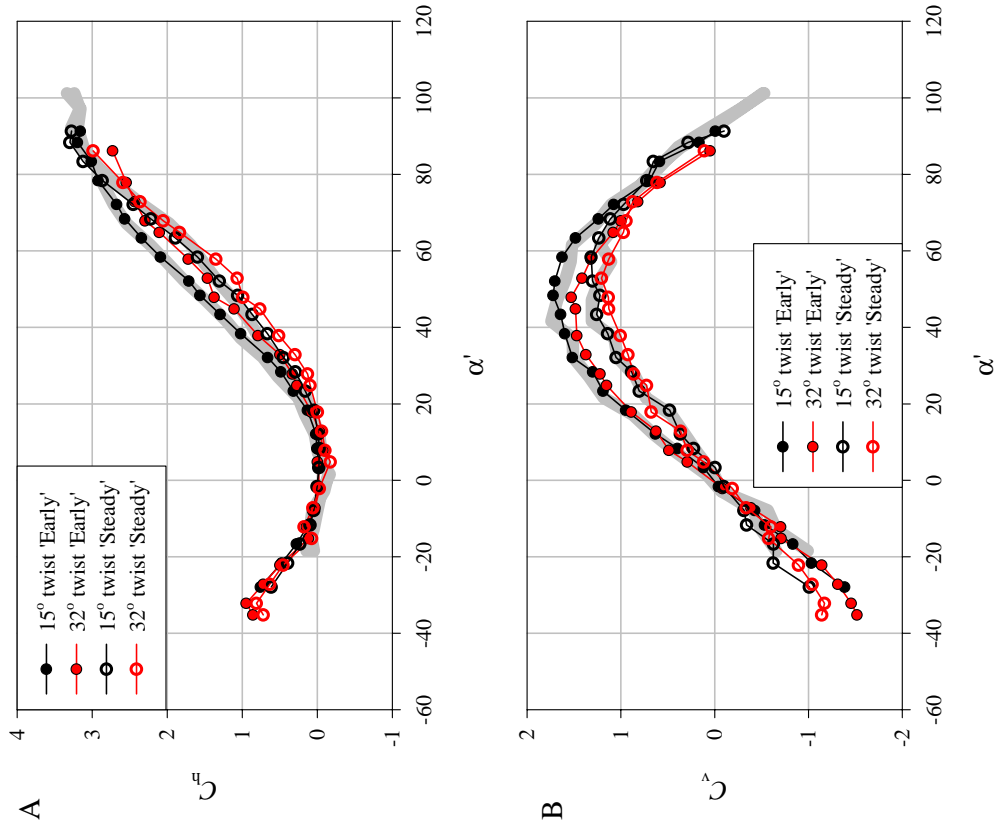


Fig. 2.12. Horizontal (A) and vertical (B) force coefficients, and the polar diagram (C), for *Manduca* wings with a range of twist under 'Early' and 'Steady' conditions. Underlying grey lines show 'Early' (higher) and 'Steady' (lower) values for standard *Manduca* wings.

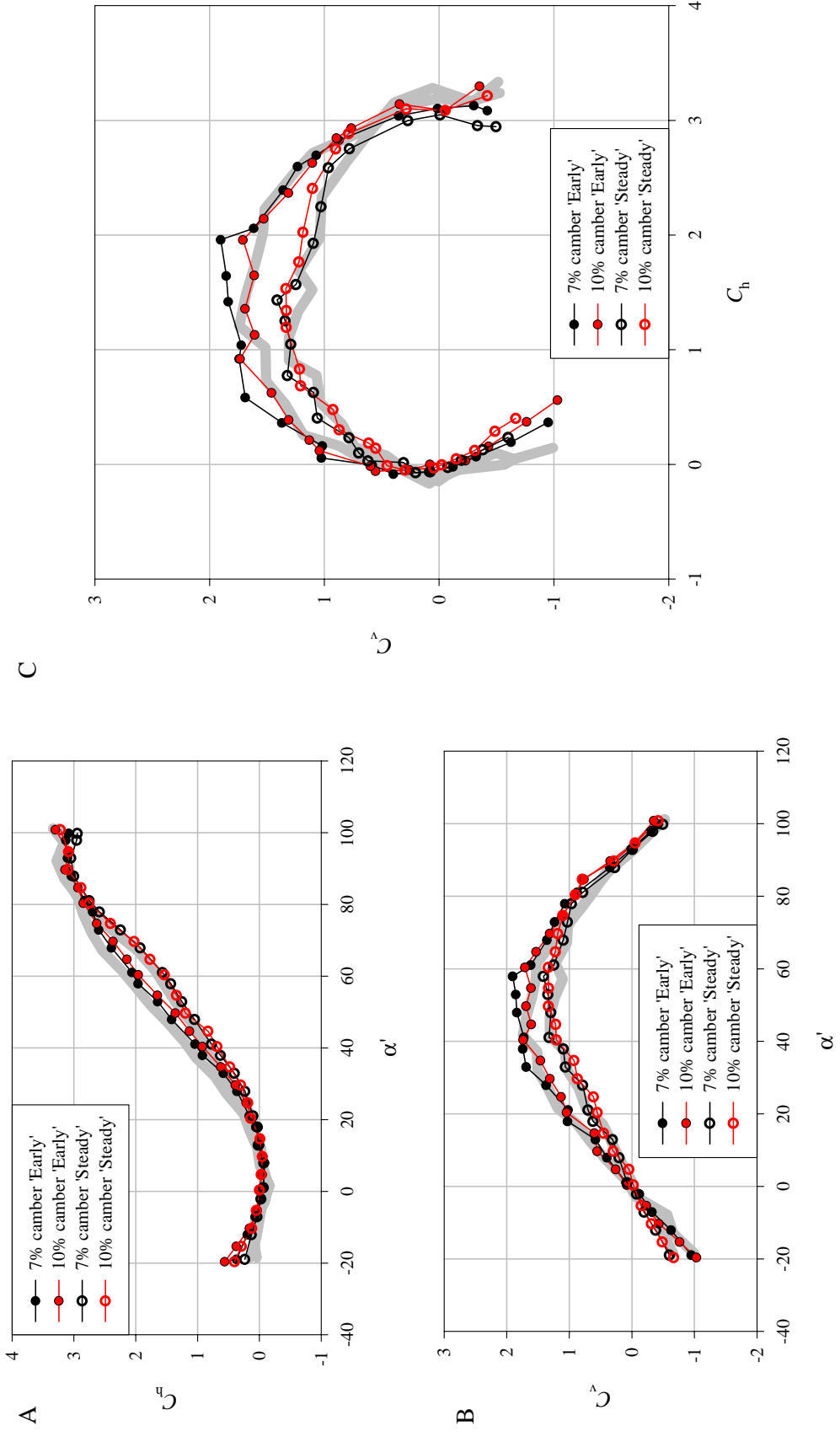


Fig. 2.13. Horizontal (A) and vertical (B) force coefficients, and the polar diagram (C), for *Manduca* wings with a range of camber under 'Early' and 'Steady' conditions. Underlying grey lines show 'Early' (higher) and 'Steady' (lower) values for standard *Manduca* wings.

Leading-edge range

Fig. 2.11 shows C_h and C_v against α' for *Manduca* wing models with a range of leading-edge forms. The relationships between force coefficients and α' are strikingly similar, especially for the 'Steady' values (as might be expected from the greater averaging period). The scatter visible in the polar diagram (Fig. 2.11C) incorporates errors in both C_h and C_v , making the scatter more apparent than in Fig. 2.11A and B.

Twist range

Fig. 2.12 shows C_h and C_v against α' for twisted *Manduca* wing models. Results for the 15° twist are not significantly different from the standard flat model. For the 32° twist, however, C_v and C_h both decrease under 'Early' and 'Steady' conditions at moderate to large angles of incidence. This is emphasised in the polar (Fig. 2.12C) which shows that the maximum force coefficients for the 32° twist are lower than for the less twisted wings. The degree of shift between 'Early' and 'Steady' force coefficients is not influenced by twist.

Camber range

Fig. 2.13 shows C_h and C_v against α' for cambered *Manduca* wing models, and the corresponding polar diagrams are presented in Fig. 2.13C. Consistent differences, if present, are very slight.

Conversion into profile drag and lift coefficients

Fig. 2.14 shows the results of the three models for determining $C_{D,pro}$ and C_L derived above, based on the average data for all wings in the ‘leading-edge’ range. The ‘Small Angle’ model uses expression (2.18) and (2.19); the ‘No Swirl’ model uses the large-angle expressions (2.22) and (2.23) and the assumption that the downwash is vertical (equation (2.24)); the ‘With Swirl’ model uses the large-angle expressions and the assumption that the induced velocity is inclined to the vertical (equation (2.25)).

The ‘Small Angle’ model is inadequate; calculated profile drag and lift coefficients are very close to ‘Steady’ propeller coefficients, and do not help account for the shift in forces between ‘Early’ and ‘Steady’ conditions. Both models using the large-angle expressions provide reasonable values of $C_{D,pro}$ and C_L for α up to 50° ; agreement with the ‘Early’ propeller coefficient polar is very good. Above 50° , both models, especially the ‘No Swirl’ model, appear to under-estimate C_L .

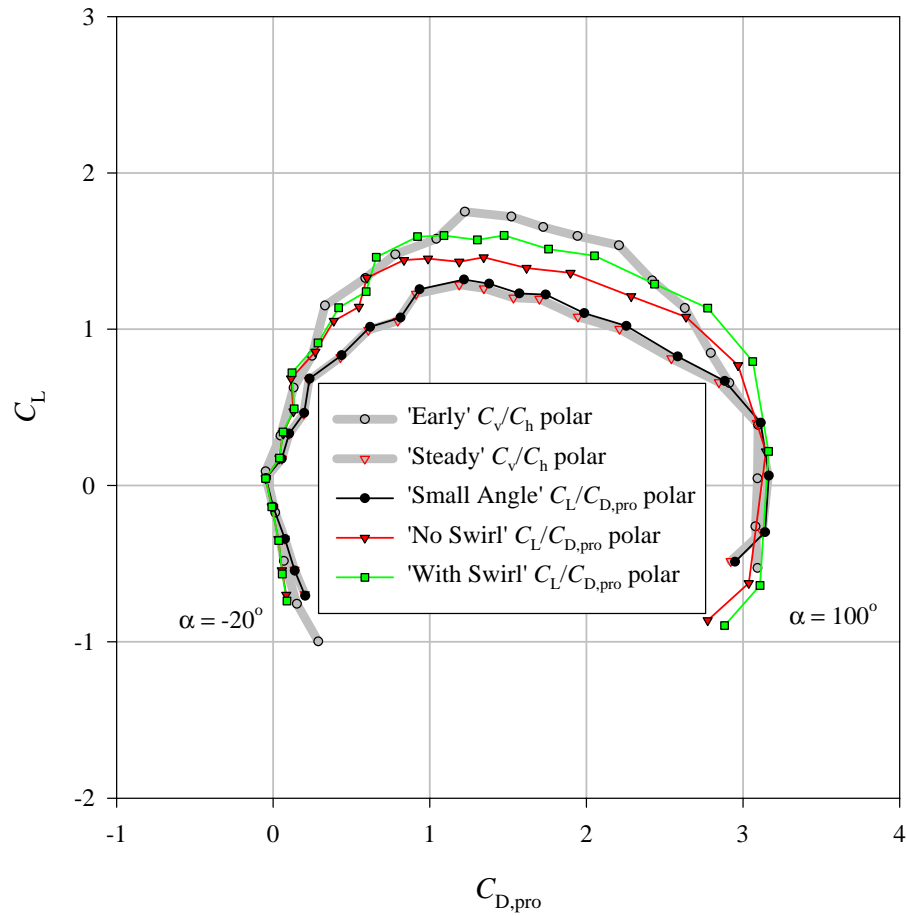


Fig. 2.14. Polar diagram showing results from three models for determining $C_{D,pro}$ and C_L from the 'Steady' data represented by the lower grey line. A good model would result in values close to, or slightly above, those of the 'Early' conditions represented by the upper grey line. Data are 'pooled' values for all wings in the 'leading-edge' series.

Air-flow observations

Smoke emitted from the leading and trailing edges, and from holes drilled in the upper wing surface, labels the boundary layer over the wing (Fig. 2.15). At very low angles of incidence (Fig. 2.15A), the smoke describes an approximately circular path about the centre of revolution, with no evidence of separation or spanwise flow. Occasionally at slight incidences (e.g. 10°), and consistently at all higher incidences, smoke separates from the leading-edge and travels rapidly towards the tip ('spanwise' or 'radially'). The wrapping up of this radially-flowing smoke into a well defined spiral 'leading-edge vortex' is visible under steady revolution (Fig. 2.15B), and starts as soon as the wings start revolving.

Near the wing tip, the smoke labels a large, fairly dispersed, tip- and trailing-vortex structure. At extreme angles of incidence (including 90°) flow separates at the trailing edge as well: stable leading- and trailing-edge vortices are maintained behind the revolving wing, and both exhibit a strong spanwise flow.

The smoke flow over the 'sawtooth' design gave very similar results.

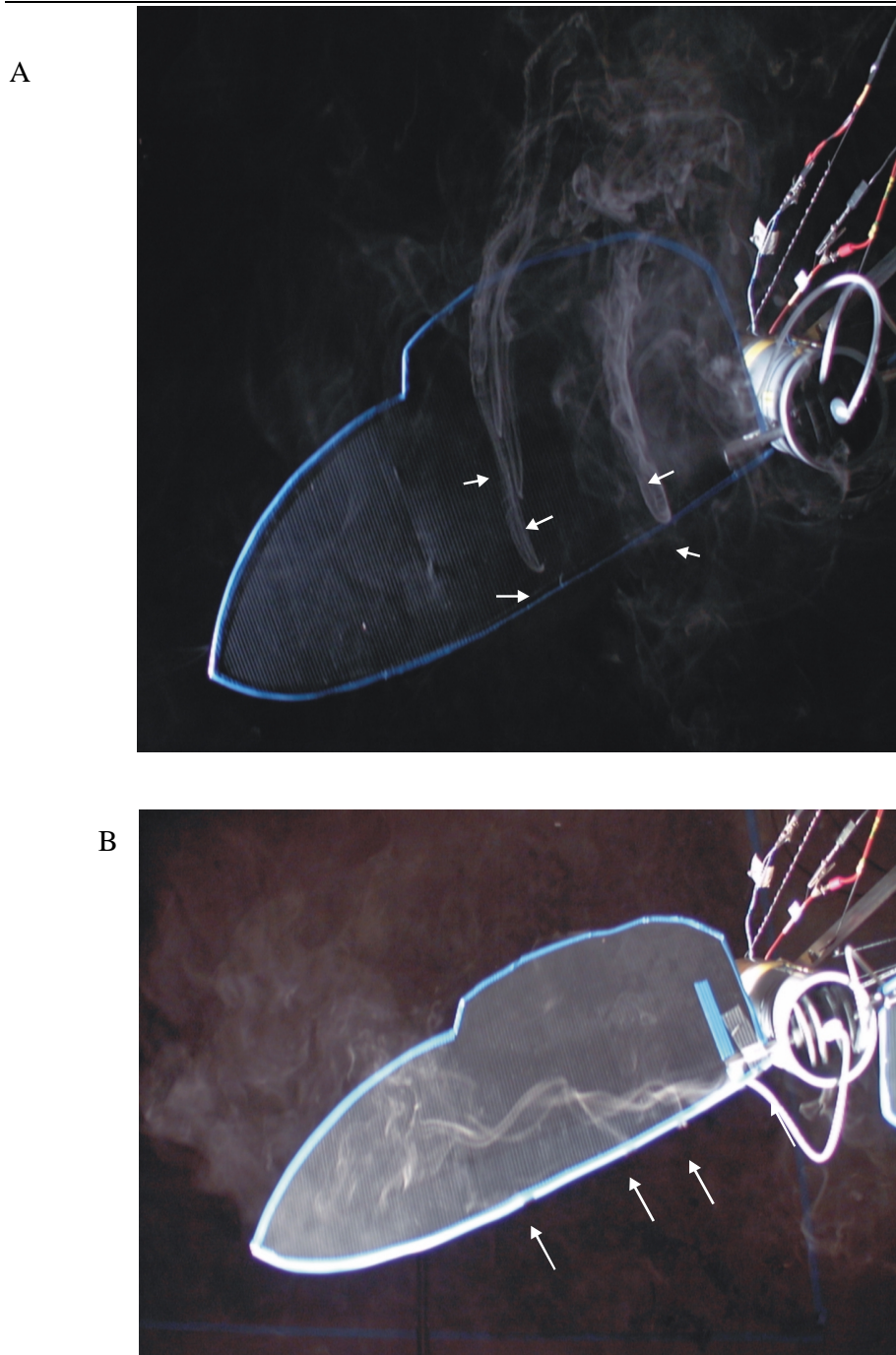


Fig. 2.15. Smoke flow over *Manduca* wings at $\alpha = 0^\circ$ (A) and $\alpha = 35^\circ$ (B) revolving steadily at 0.1Hz. Smoke was released from various positions (marked with white arrows) on the leading-edge and upper surface of the wings. At very low angles of attack, the smoke describes an approximately circular path as the wing revolves underneath. At higher angles, a spiral leading-edge vortex and strong spanwise flow is visible.

Discussion

Three points are immediately apparent from the results presented above. First, both vertical and horizontal force coefficients are remarkably large. Second, even quite radical changes in wing form have relatively slight effects on aerodynamic properties. In subsequent discussion ‘pooled’ values refer to the average results from all flat (uncambered, untwisted) wings for the whole ‘leading-edge range’. Pooling reduces noise, and can be justified as no significant differences in aerodynamic properties were observed for the range. Third, a significant shift in coefficients is visible between ‘Early’ and ‘Steady’ conditions.

Vertical force coefficients are large

If ‘Early’ values for C_v provide minimum estimates for ‘propeller’ lift coefficients (as the effects of the propeller wake are minimal, and any high, transient forces are obscured by the averaging of the ‘Early’ data), then the maximum lift coefficient $C_{L,max}$ for the ‘pooled’ data is 1.75, found at $\alpha'=41^\circ$. Willmott and Ellington (1997c) provide steady-state force coefficients for real *Manduca* wings in steady, translational, flow over a range of Re . Their results for $Re = 5560$ are shown with the ‘pooled’ data for flat wings in Fig. 2.16. The differences are remarkable: the revolving model wings produce much higher force coefficients. The maximum vertical force coefficient for the real wings in translational flow, 0.71, is considerably less than the 1.5 to 1.8 required to support the weight during hovering. Willmott and Ellington (1997c) therefore concluded that unsteady aerodynamic mechanisms must operate during hovering and slow flight. The same conclusions have previously been reached for a variety of animals, for which the values of C_L required for weight support fall well above 1.5 and sometimes over 2.

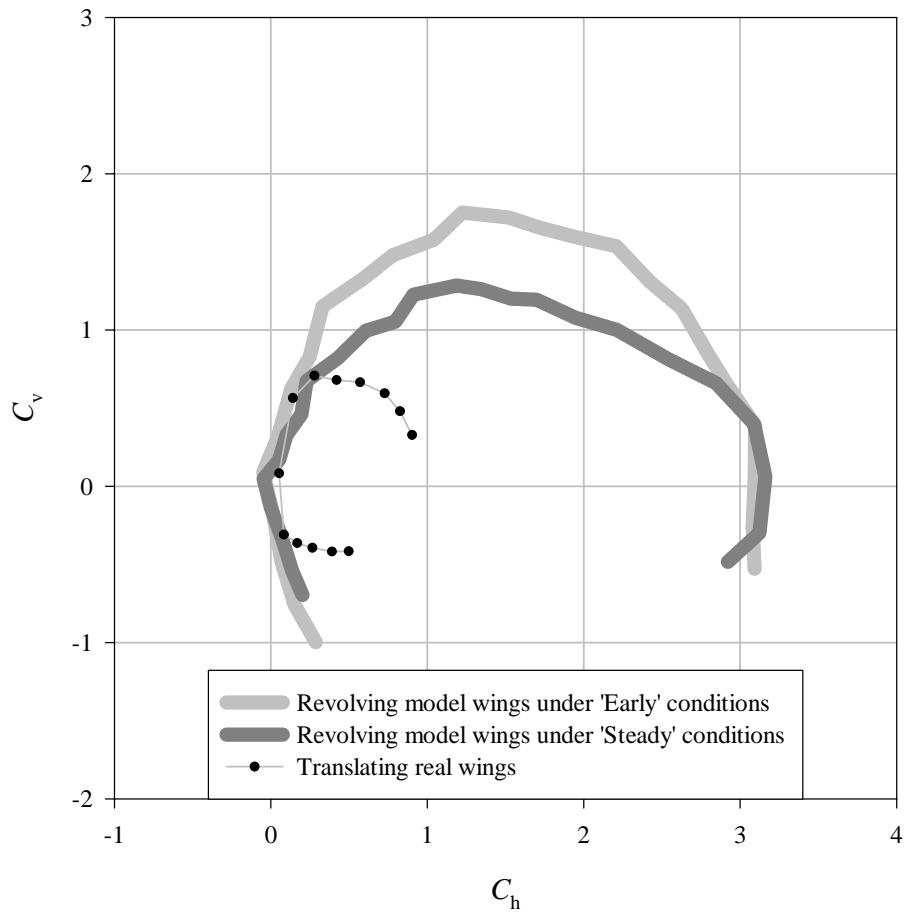


Fig. 2.16. Polar diagrams for real *Manduca* wings in steady translating flow and 'pooled' model *Manduca* wings in revolution under 'Early' (upper grey line) and 'Steady' (lower line) conditions. Data for *Manduca* in translational flow come from Willmott and Ellington (1997c) for $Re = 5560$ and range from $\alpha = -50^\circ$ to 70° in 10° increments.

The results presented in this study, that high force coefficients can be found in steadily revolving wings, suggest that the importance of unsteady mechanisms increasingly assumed since Cloupeau *et al.* (1979) (Ennos, 1989a; Dudley and Ellington, 1990b; Dudley, 1991; Dickinson and Götz, 1993; Wells, 1993; Wakeling and Ellington, 1997b; Willmott and Ellington, 1997c), particularly after the work of Ellington (1984a-f), may need some qualification. It should instead be concluded that unsteady *and/or* 3-dimensional aerodynamic mechanisms normally absent for wings in steady, translational flow, are needed to account for the high lift coefficients in slow flapping flight. Most wind tunnel experiments on wings confound the two factors: flow is steady, and the air velocity at the wing base is the same as that at the wing tip. Such experiments have resulted in maximum lift coefficients around or below 1: dragonflies of a range of species reach 0.93 to 1.15 (Newman *et al.* 1977; Okamoto *et al.* 1996; Wakeling and Ellington, 1997b), the crane fly *Tipula oleracea* achieves 0.86 (Nachtigall, 1977), the fruitfly *Drosophila virilis* 0.87 (Vogel, 1967b) and the bumblebee *Bombus terrestris* 0.69 (Dudley and Ellington, 1990b). Jensen (1956), though, created an appropriate spanwise velocity gradient by placing a smooth, flat plate in the wind tunnel, near the wing base, so that boundary effects resulted in slower flow over the base than the tip. He measured $C_{L,max}$ close to 1.3, which is considerably higher than values derived without such a procedure, and partly accounts for his conclusion that steady aerodynamic models may be adequate. Nachtigall (1981) used a propeller system to determine the forces on revolving model locust wings, but did not convert the results to appropriate coefficients.

The descent of samaras (such as sycamore keys) provides a case in which a steadily revolving, thin wing operates at high α . Azuma and Yasuda (1989) assume a $C_{L,max}$ up to 1.8 in their models, but appear to find this value unremarkable. Norberg, Å (1973) calculates high resultant force coefficients ($C_R = \sqrt{C_h^2 + C_v^2} = 1.7$), but does comment that this ‘stands out as a bit high’. Crimi (1996) has analysed the falling of ‘samara-wing decelerators’ (devices that control the descent rate of explosives) at much higher Reynolds numbers, and found that the samara wings developed a considerably greater ‘aerodynamic loading’ than was predicted using their aerodynamic coefficients.

'Propeller' v. 'unsteady' force coefficients

Although the steady propeller coefficients are of sufficient magnitude to account for the vertical force balance in hovering, this does not negate the possibility that unsteady mechanisms may be involved (Ellington, 1984a). Indeed, it would be surprising if unsteady mechanisms were not operating to some extent for flapping wings with low advance ratios. However, the results presented here suggest that the significance of unsteady mechanisms may be more limited to the control and manoeuvrability of flight (e.g. Ennos, 1989; Dickinson *et al.* 1999) than recently thought. Steady-state 'propeller' coefficients (derived from revolving wings) may go much of the way towards accounting for the lift and power requirements of hovering, though averaging force records over large periods, as has been done in this study, obscures transient high (or low) forces, which may occur on a revolving wing, particularly as it accelerates.

The relationship between C_v and C_h for sharp, thin wings

The polars displayed in Fig. 2.16 show that horizontal force coefficients are also considerably higher for revolving wings. The relationship between vertical and horizontal force coefficients is of interest as it gives information on the cost (in terms of power due to aerodynamic drag) associated with a given vertical force (required to oppose weight in the case of hovering). Flow separation at the thin leading-edge of the wing models described here results in a quite different net pressure distribution, and so C_v/C_h relationship, from that found for conventional wings.

Under 2-dimensional, inviscid conditions, flow remains attached around the leading-edge. This results in 'leading-edge suction'; flow around the leading-edge is relatively fast, and so creates low pressure. The net pressure distribution results in a pure 'lift' force; drag due to the component of pressure forces acting on most of the upper wing surface are exactly counteracted by the leading-edge suction. This is true even for a thin flat plate aerofoil: as the wing thickness approaches zero, the pressure due to leading-edge suction tends towards $-\infty$, so that the leading-edge suction force remains finite. The pressure forces over the rest of the wing act 'normal' to the wing surface. The horizontal component of the leading-edge suction force cancels the drag component of the pressure force over the rest of the wing. Under realistic, viscous,

conditions, this state can only be achieved by relatively thick wings with blunt leading-edges operating at low incidences. Fig. 2.17 (after Barnard and Philpott, 1995) shows the pressure distribution, and highlights the region of leading-edge suction, around a conventional aerofoil operating without any flow separation.

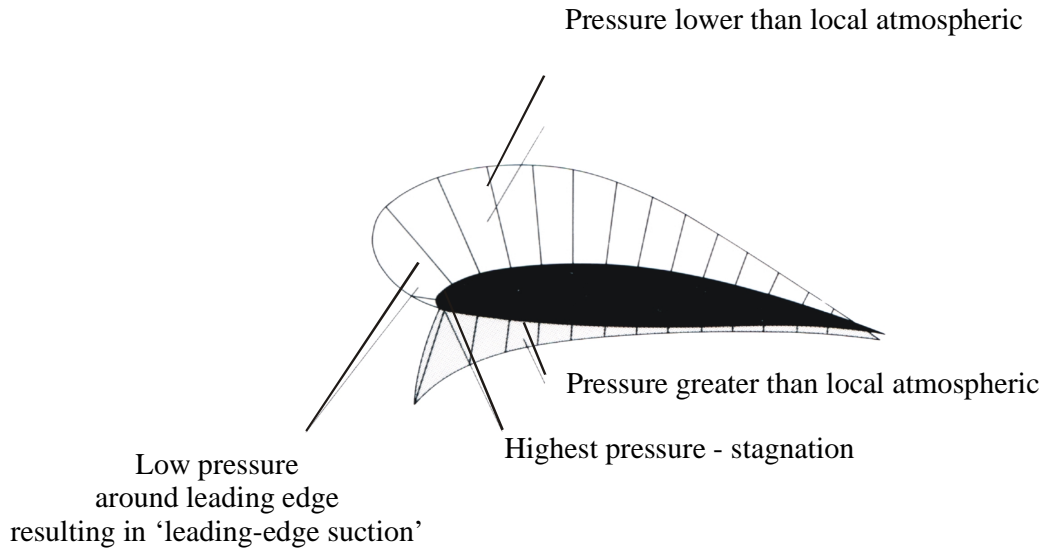


Fig. 2.17. Pressure distribution around a conventional airofoil (after Barnard and Philpott, 1995).

Viscid flow around relatively thin aerofoils at high incidences separates from the leading edge (Fig. 2.18B), and so there is no leading-edge suction. If viscous drag is also relatively small, the pressure forces acting normal to the wing surface dominate, and so the resultant force is perpendicular to the wing surface and not the relative velocity. In the case of wings in revolution, the high vertical force coefficients may be attributable to the presence of leading-edge vortices. If so, the high vertical (or lift) forces have to be associated with high horizontal (or drag) forces: leading-edge vortices. LEVs are a result of leading-edge separation (Fig. 2.18), and so are directly associated with a loss in leading-edge suction (Polhamus, 1971).

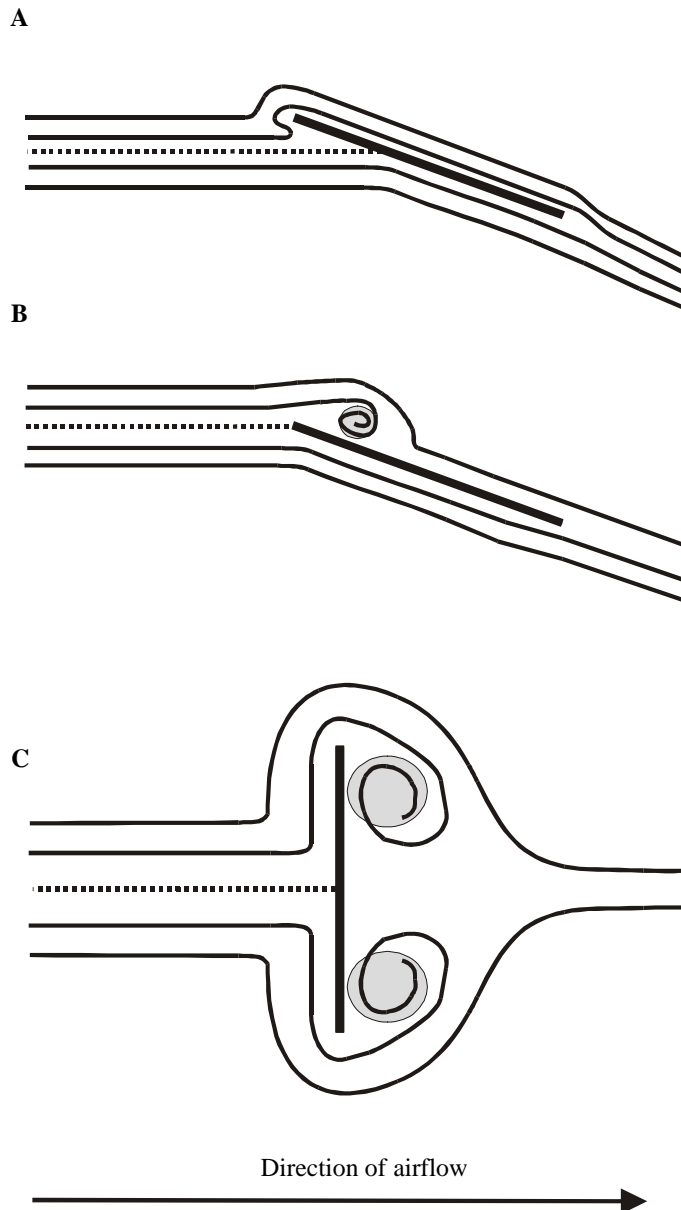


Fig. 2.18. Cartoons of flow around flat, revolving wing chords. At very low angles of incidence, or under theoretical, inviscid flow conditions, (A) flow diverges (dotted line) below the leading edge of the wing, and remains attached around the leading edge, providing 'leading-edge suction'. Under the conditions described for revolving model hawkmoth wings at high incidences (B) flow separates at the leading edge, thus losing the leading-edge suction. The separated flow then rolls up to form a leading-edge vortex, which has strong spanwise flow (grey circle). At extreme incidences (C) separation occurs at leading and trailing edges, which wraps up into two distinct structures, which both have strong flow towards the wingtip (grey circles).

The dominance of the normal pressure force allows a ‘normal force relationship’ to be developed which relates vertical and horizontal force coefficients to C_R ($=\sqrt{C_h^2 + C_v^2}$) and the geometric angle of attack α . Fig. 2.19 shows the forces acting on a wing element if the resultant force F_v' per unit span is dominated by normal pressure forces. This results, in terms of coefficients, in the relationships

$$C_h = C_R \sin(\alpha), \quad (2.28)$$

and

$$C_v = C_R \cos(\alpha). \quad (2.29)$$

These combine to produce the useful expressions

$$\frac{C_v}{C_h} = \frac{1}{\tan(\alpha)} \quad (2.30)$$

and

$$C_h = C_v \tan(\alpha), \quad (2.31)$$

which are used in Chapter 4 to determine power requirements of hovering and slow flight.

Fig. 2.20 compares the measured vertical and horizontal coefficients with those predicted from the normal force relationship for the standard flat wing data. The success of the model for both ‘Early’ and ‘Late’ conditions suggests that pressure forces normal to the wing surface are dominating the vertical and horizontal forces. At very low incidences, it is likely that viscous forces largely comprise the horizontal (equivalent to drag) forces, but this cannot be determined from the data. At higher incidences, though, C_h is clearly dominated by pressure forces acting perpendicular to the wing surface.

The trigonometry of the forces shown in Fig. 2.19 is such that the same physical arguments, this time with $C_R = \sqrt{C_{D,pro}^2 + C_L^2}$, and the effective angle of attack α_r , result in

$$C_{D,pro} = C_R \sin(\alpha_r), \quad (2.32)$$

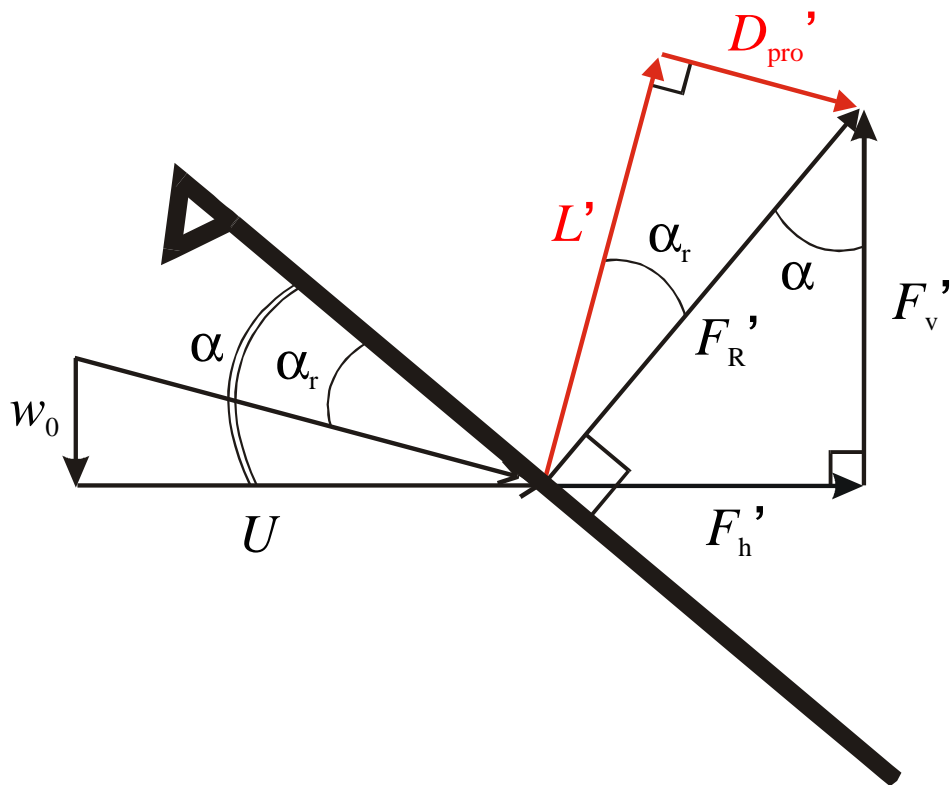


Fig. 2.19. Trigonometry of forces for a blade element if the resultant force for the element F_R' acts normal to the wing surface.

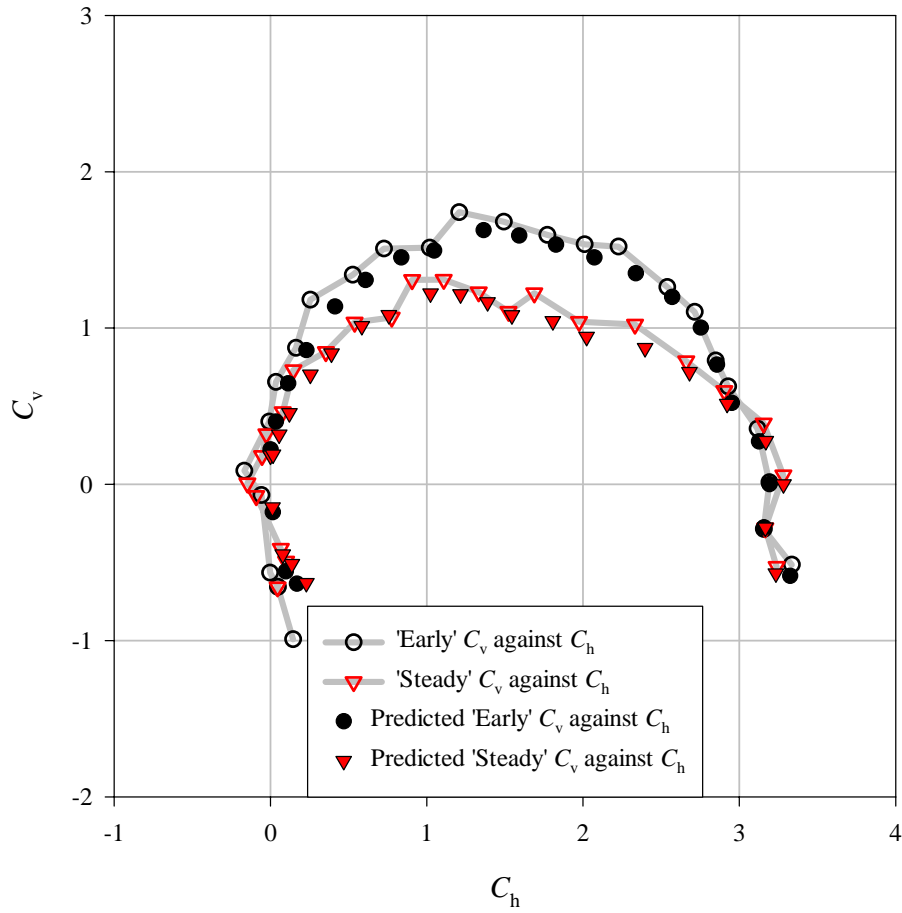


Fig. 2.20. Polar diagram comparing measured horizontal and vertical force coefficients with those predicted from the normal force relationship for the standard, flat, *Manduca* planform. α ranges from -20° to 100° in 5° increments.

$$C_L = C_R \cos(\alpha_r). \quad (2.33)$$

From this,

$$\frac{C_L}{C_{D,\text{pro}}} = \frac{1}{\tan(\alpha_r)}. \quad (2.34)$$

which may be used in power calculations based on the lift-drag frame of reference (Ellington, 1999).

This account of the pressure distribution over thin aerofoils, and the normal force relationship, should be applicable whenever the flow separates from a sharp leading-edge. Indeed, Fig. 2.21 shows that the division into vertical and horizontal force components using equations (2.28) and (2.29) fits very well for the real *Manduca* wings in translating flow, where the leading-edge vortex is two-dimensional and unstable (Willmott and Ellington, 1997c). The model underestimates C_h at small angles of attack, but that is simply because skin friction is neglected. However, *Manduca* typically operates at much higher angles, where the model fits the data very well for both translating and revolving wings.

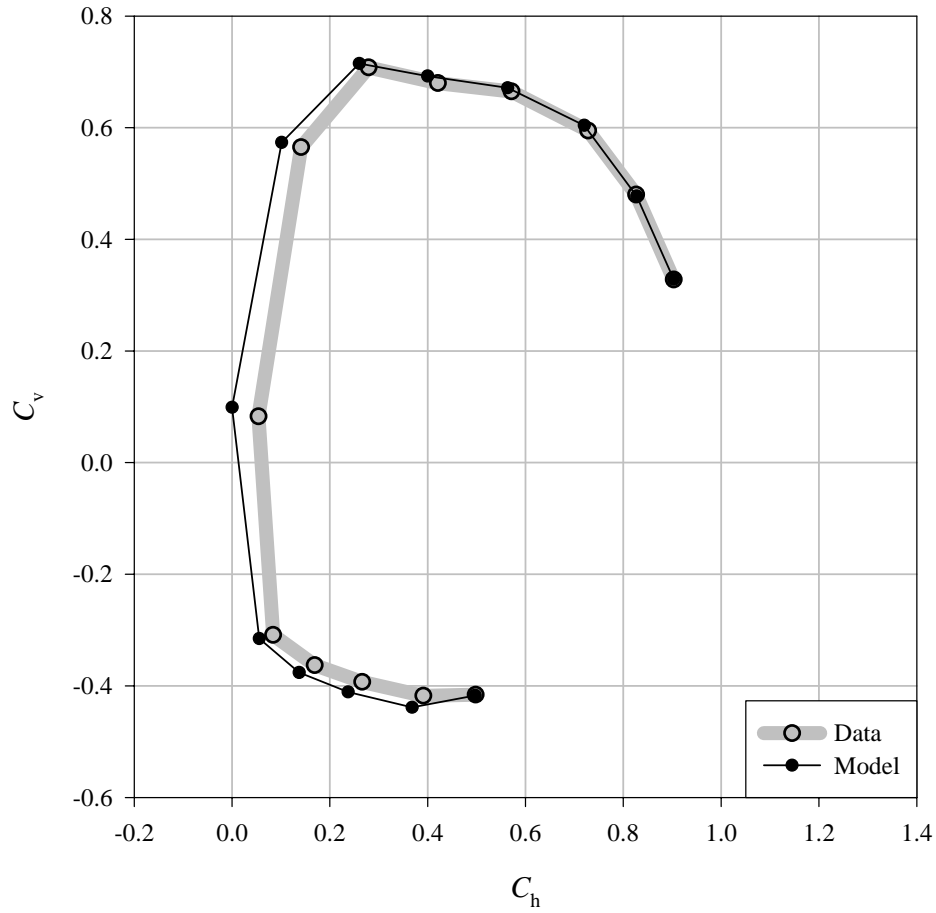


Fig. 2.21. Polar diagram showing the results of dividing the resultant force coefficient into horizontal and vertical coefficients using the ‘normal force relationship’. The original data are for real *Manduca* wings in translational flow at $Re = 5560$ (Willmott and Ellington, 1997c). α ranges from -50° to 70° in 10° increments.

The effects and implications of wing design

Leading-edge detail

The production of higher coefficients than would be expected in translating flow appears remarkably robust, and is relatively consistent over quite a dramatic range of leading-edge styles. This may be surprising as the leading-edge characteristics of swept or delta wings are known to have effects on leading-edge vortex properties (Lowson and Riley, 1995), and are even used to delay or control the occurrence of LEVs at high incidences. Wing features of some animals, such as the projecting bat thumb or the bird alula, may perform some role in LEV delay or control analogous to wing fences and vortilons on swept-wing aircraft (see Barnard and Philpott, 1995). Such aircraft wings, and perhaps the analogous vertebrate wings, experience both conventional (attached) and detached (with LEV) flow regimes at different times and positions along the wings. However, the results here suggest that it is unlikely that very small-scale detail of leading edges, such as the serrations on the leading edges of dragonfly wings (e.g. Hertel, 1966), would influence the force coefficients for rapidly revolving wings. The peculiar micro-structure of dragonfly wings may be more closely associated with their exceptional gliding performance (Wakeling and Ellington, 1997a).

Twist

The ‘Early’ and ‘Steady’ polars for the *Manduca* wing design with moderate (15°) twist are virtually identical to those for the flat wing design (Fig. 2.12). The only difference is that the zero-lift angle α_0 was about -10° for the twisted wing, so angles of incidence α' ranged from -30° to 90° instead of -20° to 100° as for the flat wings. Thus the bottom left of the polar was slightly extended, and the bottom right shortened. The effect was even more pronounced for the highly twisted (32°) wing design. This design also showed substantial reduction in the magnitude of the force coefficients at high angles of incidence, but this is readily explained: even when the

wing base is set to a high incidence, the tip of a highly twisted wing will be at a much lower angle.

Twist is desirable in propeller blades, and has been assumed desirable for insects by analogy. The downwash angle ε is typically smaller towards the faster moving tip of a propeller, so a lower angle of incidence α' is needed to give the same effective angle of incidence $\alpha_r' (= \alpha' - \varepsilon)$. Thus a twisted blade allows some optimal effective incidence to be maintained at each radial station despite the varying effects of downwash. However, what this optimal effective angle of incidence should be is unclear for insects. These revolving, low Re wings show no features of conventional stall; changes from high C_v to high C_h with increasing angle can be related entirely to the normal pressure force, and not to the sudden development of a stalled wake. So it is not, presumably, stall that is being avoided with the twisted wing.

The characteristic normally optimised in propeller design is the 'aerodynamic efficiency', or lift to drag ratio. This occurs at α_r' well below 10° for conventional propellers, and at α ($\approx \alpha_r'$ at these small angles) around 10° for the translating *Manduca* wings (Willmott and Ellington, 1997c). There is no reason to suppose that such values for α are not appropriate for the revolving wings described here. The maximum lift:drag ratio could not be determined in this study because of noise in the torque transducer at small incidences, but it is reasonable to suppose that the optimal α_r' for aerodynamic efficiency is low, probably below 10° . This is certainly below the angles used by hawkmoths, where α ranges from 21° to 74° (Willmott and Ellington, 1997b) or by many hovering insects: Ellington (1984c) gives $\alpha = 35^\circ$ as a typical value. So, twist is not maintaining an α_r' along the wing that maximises the lift:drag ratio. Angles of attack for hovering insects suggest that a compromise between high lift and a reasonably small drag might be more important than maximising the lift:drag ratio. They operate near the upper left corner of the polar, and the observed moderate wing twists might sustain the appropriate α_r' along the wing. However, it must be emphasised that the polars for the flat and moderately twisted wings were almost identical. The same point on the polar could be attained by either wing design simply by altering the geometric angle of attack, so there are no clear benefits to the twisted wing.

Less direct aerodynamic functions of twist should also be considered. Ennos (1988) shows that camber may be produced through wing twist in many wing designs,

so any aerodynamic advantages of camber might drive the evolution of twisted wings. It is also possible that twisting may have no aerodynamic role whatever, or may even be aerodynamically disadvantageous. The null hypothesis for this discussion should be that wing twist is just a structural inevitability for ultra-light wings experiencing rapidly changing aerodynamic and inertial forces. Twist may simply occur due to rotational inertia during pronation and supination, and be maintained due to an aerodynamic loading on a slightly flimsy wing. The lack of twist in flapping *Drosophila* wings has been explained by the higher relative torsional stiffness of smaller wings (Ellington 1984c). If twisting had aerodynamic advantages, the evolution of more flexible materials (which, if anything, should be less costly) might be expected. Of course, these arguments are confounded in many aspects, including *Re*. However, it is difficult for any description of an aerodynamic function of twist to account for the purpose of wings twisted in the opposite sense, where the base operates at lower α than the tip. This appears to be the case for *Phormia regina* (Nachtigall, 1979).

Camber

Fig. 2.13 agrees with results on the performance of 2-dimensional model *Drosophila* wings in unsteady flow (Dickinson and Götz, 1993); any changes in the aerodynamic properties of model hawkmoth wings due to camber are slight. Shifts in maximum C_h or C_v appear to be within the experimental error, so these trends should not be put down to aerodynamic effects. The similarities of the polars show that camber provides little improvement in lift:drag ratios at relevant angles of incidence.

Camber is beneficial in conventional wings because it increases incidence gradually across the chord. This shape deflects air downwards gradually, and the abrupt and undesirable breaking away of flow from the upper surface is avoided. So, the conventional reasoning behind the benefits of cambered wings to insects appears flawed if flapping insect wings use flow separation at the leading-edge as a fundamental part of lift generation. A reasonable analogy exists with aeroplane wings. The thin wings of a landing Tornado jet use leading- and trailing-edge flaps to increase wing camber, maintaining attached flow, and allowing higher lift coefficients than would otherwise be possible. Concorde, however, uses the high force coefficients

associated with leading-edge vortices created by flow separation from the sharp, swept, leading-edges: no conventional leading-edge flaps are used, as flow separation from the leading-edge is intentional.

Camber still has a role in improving the aerodynamic performance of gliding wings, but any beneficial aerodynamic effects for flapping insect wings will require experimental evidence, and not analogy with conventional wings designed (or adapted) for attached flow.

Accounting for differences between ‘Early’ and ‘Steady’ propeller coefficients

Fig. 2.8 and Figs 2.10 to 2.13 show that there is a considerable change in force production between ‘Early’ and ‘Steady’ conditions. There are two possible accounts for this change. First, the wings cause an induced flow in steady revolution that is absent at the start, and this decreases the effective angle of incidence. Second, there may be a fundamental change in aerodynamics due, for instance, to the shedding of the leading-edge vortex (and a resulting stall) as is seen for translating wings (Dickinson and Götz, 1993). Simple accounts are taken of the induced downwash in the calculation of $C_{D,pro}$ and C_L from steady coefficients (Fig. 2.14). Below $\alpha' = 50^\circ$, the downwash alone appears to account in the shift between ‘Early’ and ‘Steady’ propeller coefficients; the calculated $C_{D,pro}$ and C_L fit the observed $C_{h,Early}$ and $C_{v,Early}$ well. Also, the observation (Fig. 2.15) that LEVs can be maintained during steady revolution, supports the view that the shift in propeller coefficients can be accounted for with the effects of downwash alone, without a fundamental change in aerodynamics.

At very high α' the downwash models for determining $C_{D,pro}$ and C_L provide poorer results. A change in the value of $\overline{w_0}$ at high α' can improve the fit of $C_{D,pro}$ and C_L to $C_{h,Early}$ and $C_{v,Early}$: both k_{ind} and R (separation at the wing tip may reduce the effective wing length) in equation (2.15) may be altered. However, varying correction factors in the high α' -range without *a priori* justification (such as more accurate flow visualisation) limits the possibility of aerodynamic inferences. Both fundamental changes in aerodynamics, and failure of the Rankine-Froude actuator disc model for

calculating induced downwash, are also reasonable explanations for part of the shift in propeller coefficients between ‘Early’ and ‘Steady’ conditions at very high α' . An aerodynamic change due to a shift in the position of the vortex core breakdown is particularly worthy of consideration. Ellington *et al.* (1996) and Van den Berg and Ellington (1997) noted that the core of the spiral LEV broke down at about two-thirds of the wing length, resulting in a loss of lift in outer wing regions. Liu *et al.* (1998) postulated that this breakdown is due to the adverse pressure gradient over the upper wing surface due to the tip vortex. The development of the full vortex wake with its associated radial inflow over the wings might well shift the position of vortex breakdown inwards under ‘Steady’ conditions at higher α' , producing a quantitative reduction in the lift coefficient compared with the ‘Early’ state.

Potential errors

The small forces and relatively slow, large wings used in this study mean that a variety of potentially important errors should be considered. While random noise due, for instance, to small draughts or electronic drift, should be minimised by the averaging over several tests described, averaging across tests fails if an error occurs in a repeated manner. For instance, ‘bouncing’ of the wing after the rapid start, evident in Fig. 2.6 may have repeatable aerodynamic or electrical effects. Averaging over relatively large angles of revolution should limit these problems, but the effects of an asymmetric deviation from the true mean (e.g. complete loss of electrical contact) would cause error.

While high quality ball-races were used to support the propeller axle and the wings were relatively light, non-aerodynamic torques may be influenced by aspects of wing weight and weight distribution, so the correction for the aerodynamic effects of the sting and revolving propeller head may be somewhat inaccurate. If load distribution were to have an effect, systematic errors with increasing angles of attack are possible; the majority of the mass of the wing lies behind the line of the sting when the wing is held horizontally, but directly under the line of the sting when vertical.

The orientation of the wing base with respect to the propeller body, and the trailing edge with respect to supporting beams and wires, is also confounded with

angle of attack. These difficulties are outweighed by the benefits of using the same wings for tests at the complete range of α .

Conclusion

Steadily revolving model *Manduca* wings produce high vertical (\approx lift) and horizontal (\approx profile drag) force coefficients due to the presence of a LEV. Both horizontal and vertical forces, at relevant angles of attack, are dominated by the pressure difference between upper and lower surfaces; separation at the leading-edge prevents 'leading-edge suction'. This allows a relationship between vertical and horizontal forces, and the geometric angle of attack, to be derived for thin, flat wings.

Force coefficients are remarkably unaffected by considerable variations in leading-edge detail, twist and camber. Traditional accounts for the adaptive functions of twist and camber are based on conventional attached-flow aerodynamics, and are not supported.

Attempts to derive conventional profile drag and lift coefficients from 'Steady' propeller coefficients are relatively successful for angles of incidence up to 50° , and hence to the angles normally applicable to insect flight.

Chapter 3: Propeller force coefficients from mayfly to quail

Introduction

High force coefficients are required to account for hovering flight in animals ranging from small insects (e.g. Ellington, 1984a-f) to medium sized birds (Norberg, U, 1975) and bats (Norberg, U, 1976). Ellington *et al.* (1996) showed spiral leading-edge vortices (LEVs) to be present over flapping real and model hawkmoth wings. These LEVs, created by dynamic stall and maintained by spanwise flow, contribute significantly to lift production in slow-flying hawkmoths. Chapter 2 shows this phenomenon, and high force coefficients, to be a stable aerodynamic characteristic of revolving model moth wings. The current chapter aims to determine how robust this characteristic is to variations in wing design and Reynolds number. Both model *Manduca* wings with a range of aspect ratio, and real and model wings from a number of ‘key species’, are tested.

Aspect ratio

While insects show a great diversity in wing size, shape, number (0, 2, 4), mechanical coupling, edge detail (including the ‘fringe-wings’ characteristic of small insects in several taxa), hardness, toughness, and density, many animal wings, particularly of animals capable of hovering, can be described in very simple terms (Weis-Fogh, 1973; Ellington, 1984b). One key variable is the aspect ratio AR of the wing:

$$AR = \frac{4R^2}{S}, \quad (3.1)$$

where S is the area of both wings (most animals are functionally two-winged; many four-winged insects link fore- and hind-wings) and R is the single wing length. Standard *Manduca* planforms (Chapter 2), with their chords scaled by $\times 0.4$, $\times 0.6$, $\times 0.8$, $\times 1$ and $\times 1.4$ are tested in this study, resulting in 5 wing designs with an aspect

ratio range of 4.53 to 15.84. Scaling the chord produces reasonably insect-wing-like planforms with the variation of a single parameter.

Insects have wings of AR ranging from 2.8 (butterflies; Dudley and DeVries, 1990) to 10.9 (crane flies; Ellington, 1984b). Vertebrates capable of hovering have wings ranging in AR from 4.4 (pied flycatcher; Norberg, U, 1975) to 8.2 (hummingbirds; Wells, 1993). The wings in this study range from AR = 4.53 to 15.84, and incidences over 90° are tested, so inferences can be drawn for animals which hover using a vertical stroke plane, or swim with using drag-based propulsion.

Conventional propellers and wind turbines revolve, but delayed-stall and high force coefficients tend to exist only at the wing (rotor) bases (Himmelskamp in Schlichting, 1968 (propellers); Graham, 1992 (wind turbines)). Otherwise, flow over high AR propellers and turbines at high incidences stalls conventionally, and blade-element analyses using coefficients derived from steady, 2-d flow conditions are effective. So, it is reasonable to expect that the high-lift mechanisms described in Chapter 2 for wings of AR = 6.34 might gradually or suddenly decline with increasing aspect ratio.

The implications of Reynolds number to flight

Reynolds number Re has a large impact on the behaviour of fluids past an object; Vogel (1981) presents the concepts clearly in a biological context. It is therefore reasonable to expect Re to have a similar bearing on the flow (and so lift and drag) acting on wings. Indeed, it is frequently supposed that many of the unexpected phenomena associated with insect flight may be accounted for by the low values of Re at which they operate. However, predictions based on Re arguments are not always founded; while it is true that viscous drag forces are higher for smaller animals, it is not true that the very small and 'fringe-winged' insects ($Re < 28$) 'row' through the air using drag-based mechanisms. Indeed, the vertical stroke plane associated with drag-based weight-support is surprisingly seen in larger insects (butterflies) at Re around 2800 (Maxworthy, 1981; Ellington, 1984a; Sunada *et al.* 1993).

So, at this stage, it is unclear whether insects, small, and even large vertebrates, operate in the same Re regime; it is unknown whether there are significant qualitative differences in flow analogous to the transition between laminar and

turbulent conditions. Is there a subtle gradient from one regime to another (this does not appear likely given the properties of normal laminar / turbulent transitions)? Or is there a biologically significant threshold above (or below) which certain aerodynamic mechanisms are unable to operate? If so, where are these boundaries?

Key species

In order to gain more information of biological interest, this study investigates several key species for which the appropriate parameters are known. Bees are of particular interest as they show a considerable size range both within a species (between different castes of bumblebee) and within related genera (e.g. the Euglossini, or orchid bees). A coupled bumblebee wing was therefore tested to provide information on the aerodynamic properties of wings in revolution for an insect for which there is a great deal of morphological, kinematic and energetic data (Dudley and Ellington, 1990a,b; Cooper, 1993; Hedenström *et al.* in prep.), and which should also be applicable to studies of euglossine bees (Casey and Ellington, 1989; Dudley, 1995; Dudley and Chai, 1996).

To determine the steady aerodynamic performance of wings in revolution at low and high Re , a 'mini-spinner' was built covering the Re range from $Re = 1100$ to $Re = 26\ 000$. The model animals chosen for these extremes were the mayfly *Ephemera vulgata* and blue-breasted quail *Coturnix chinensis*, for which fresh wings were available. The 'mini-spinner', though limited in a number of ways, proved an effective and 'low-tech' tool. It also allows the use of real bird wings over a limited size range, so both real and model quail wings were tested.

Materials and Methods

Force measurements were made using two experimental propellers. The larger, described in Chapter 2, allows the determination of ‘Early’ (from the first half-revolution) and ‘Steady’ vertical and horizontal forces, using foil strain gauges. The smaller, much simpler design, could only measure ‘Steady’ forces, but could do so over a much larger speed range.

Vertical and horizontal force coefficients were derived from measured vertical forces and torques as described in Chapter 2. Following Chapter 2, the term ‘propeller coefficient’ is used to distinguish force coefficients derived from propeller experiments.

Large propeller experiments

Unless otherwise stated, all aspects of experimental method for the large propeller experiments were identical to those described in Chapter 2. Methods of wing construction, force measurement and data processing were suitable for a limited *Re* range, appropriate for hawkmoths and queen bumblebees

Aspect ratio

The standard *Manduca* planform was adapted to produce wing pairs with a range of 5 aspect ratios (Fig. 3.1A): all wings were thin and flat. The wing length in every case, including the offset due to the method of attachment to the propeller head (see Chapter 2), was 556mm, and the relevant non-dimensional wing moments remained constant: $\hat{r}_2(S) = 0.5472$ and $\hat{r}_3(S) = 0.5881$. Wing thickness was constrained by the material used, and the angular velocity was kept constant. The mean relative wing thickness (to mean chord) and *Re* (defined using Ellington’s (1984f) conventions) were therefore confounding variables (Table 3.1).

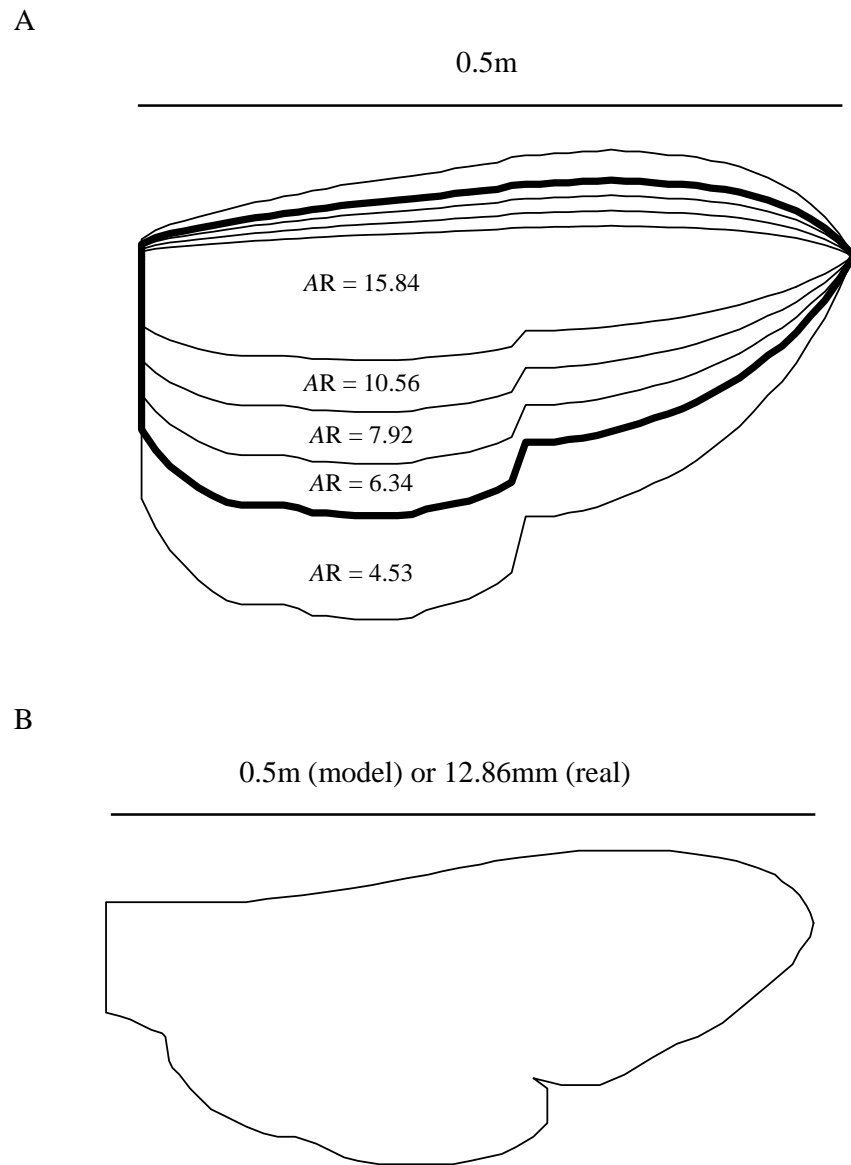


Fig. 3.1. Model *Manduca* planforms with a range of aspect ratio (A), and *Bombus* planform (B).

Table 3.1. *Confounded variables with variation in aspect ratio*

Wing type (Aspect ratio)	Wing thickness (%)	Reynolds number
15.84 (very narrow)	3.91	3230
10.56	2.61	4846
7.92	1.96	6461
6.34 (standard)	1.57	8071
4.53 (wide)	1.12	11295

The constant angular velocity also resulted in smaller signal:noise ratios for higher AR (narrower) wings, because they experienced smaller forces.

Bumblebee

The planform for a bumblebee (Fig. 3.1B) *Bombus terrestris* wing design was taken from a previous study (Hedenström *et al.* 2000) and used to produce a wing pair as described for *Manduca* (Chapter 2). Bumblebee ‘B27’ was selected as its aspect ratio and radii for moments of area were the closest to the population averages. Again, the wing shape was kept constant, meaning that the offset due to the attachment of the wings to the propeller head changed the wing moments, as shown in Table 3.2.

Table 3.2. *Morphological parameters for real and model bumblebee wings*

	<i>Bombus</i> B27	Model <i>Bombus</i> with offset
R (mm)	12.86	556
AR	6.32	7.13
$\hat{r}_2(S)$	0.541	0.578
$\hat{r}_3(S)$	0.585	0.614

The propeller was driven slightly more slowly than for the *Manduca* tests, at 0.147Hz, thus reducing the Reynolds number to 5496: a value appropriate for the largest queen bumblebees, and big euglossines. Further reduction in speed produced very noisy results, while reducing the wing length would have confounded the effects

of the offset, which otherwise was kept constant for experiments on the large propeller.

Small propeller ('mini-spinner') experiments

Fig. 3.2 shows the basic construction of the 'mini-spinner'. It uses the same principle for the measurement of vertical forces (moments about a knife-blade fulcrum, forming a 'see-saw') but uses different principles for torques. Unsteady force measurements and flow visualisations are impossible with the mini-spinner, but the smaller size requires higher frequencies for Re similarity, with the advantage that very low Re models can be used while minimising the effects of random air movements. The size and relative strength of the mini-spinner also allows the use of real bird wings.

The mini-spinner for low Re : model mayfly wings

Vertical forces

The mini-spinner as shown in Fig. 3.2A has the motor, gearbox and propeller head oriented vertically. During steady revolution, a moment is created about the fulcrum due to the vertical force and the arm length to the right of the fulcrum. This is equal and opposite to the moment created by the tension force applied from a wire connected to the under-hook of a Mettler BasBal BB240 balance situated directly above, and the appropriate arm length to the left of the fulcrum. This set-up was calibrated with the repeated application of a 1g mass to the centre of the propeller head. 5 (or 10 at values of α of particular interest) vertical force measurements were made at each angle of attack.

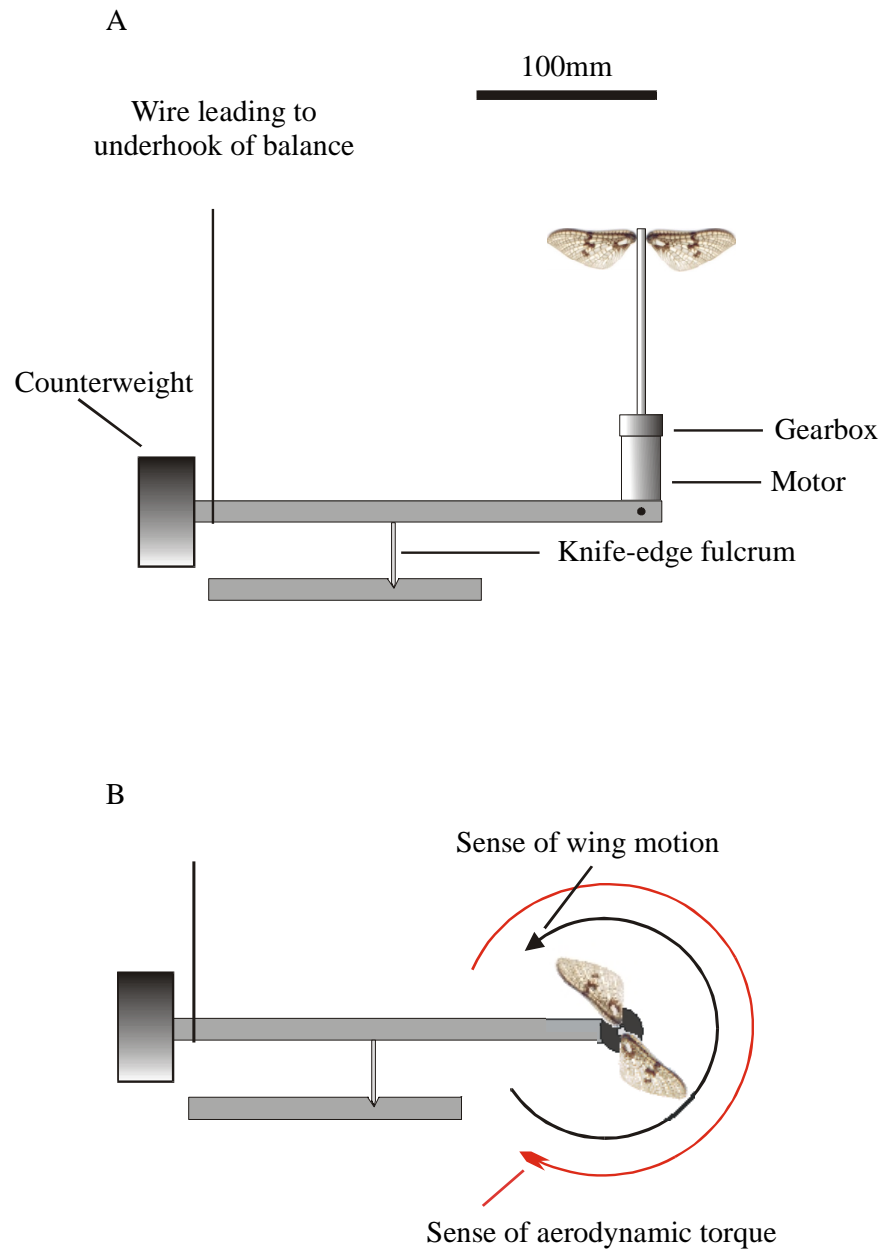


Fig. 3.2. The mini-spinner set-up for small vertical force (A) and torque (B) measurements.

Torques

Aerodynamic torques were measured by rotating the motor, gearbox and propeller head unit to a horizontal orientation as shown in Fig. 3.2B. During steady revolution, the moment about the fulcrum equals the aerodynamic torque from the revolving propeller head and wings. This torque can thus be calculated given the distance from the fulcrum to the wire attachment (140mm), directly below the balance. The same number of measurements were made as for the vertical forces, and the aerodynamic effects of the motor head and stings were determined from tests without wings, and removed.

Each vertical force and torque value was the mean of a pair of runs, starting with the wings in opposite positions. The measurements taken for each run consisted of a 'zero', and a 9s average after steady revolution had been achieved. This takes into account any error due to an imbalance between the wings.

Wing design

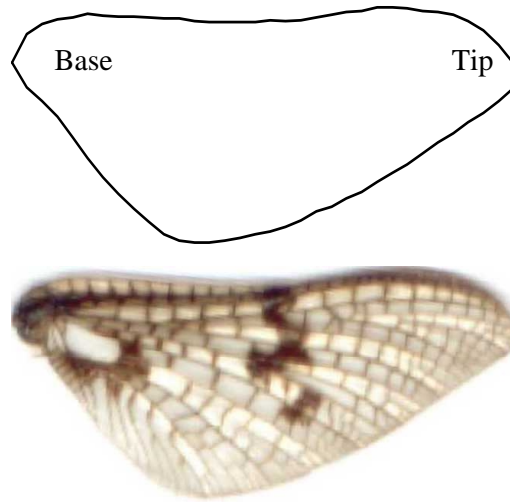
Model mayfly forewings were based on those from a 26.4mg male mayfly *Ephemera vulgata* (Fig. 3.3A). The hindwings were not included in the model, as they were small (and the appropriate moments of wing area relatively even smaller), and their orientation during flapping flight unknown. Any extra wing chord due to the hindwings is likely to have a more significant effect for gliding or 'parachuting' flight typical of mayflies, when the wing base and tip experience similar air velocities, as opposed to flapping, when the wing tips move faster, and are likely to dominate force production. The planform of the forewing was maintained, so the small shift due to the diameter of the rotor head (of diameter 9mm, so an offset of 4.5mm) influences the wing moments. Table 3.3 shows the resulting wing parameters.

Table 3.3. *Morphological parameters for real and model mayfly wings*

	Real forewing	Real hindwing	Combined real wings	Model forewing
R (mm)	13.0	3.9	13.0	54.5
AR	6.42	5.10	5.77	7.67
$\hat{r}_2(S)$	0.546	0.572	0.520	0.573
$\hat{r}_3(S)$	0.588	0.610	0.568	0.609

A

50mm (model) or 13.0mm (real)



B

100.1mm

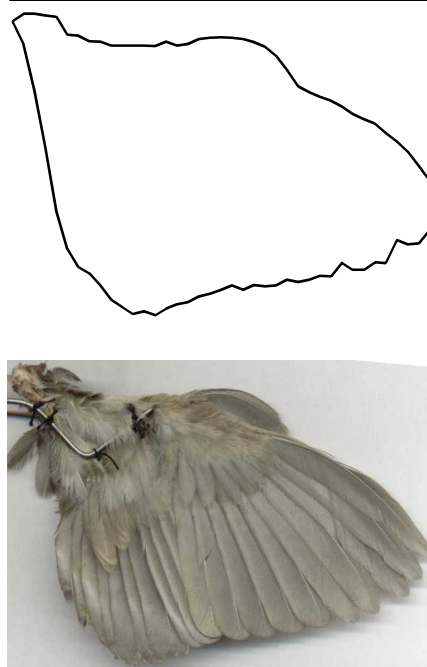


Fig. 3.3. Model and real wing planforms for mayfly (A) and quail (B).

The model wings were constructed from stiff, thin (0.15mm) card glued to 0.57mm diameter wire running half-way down the ventral surface of the wing. This resulted in a wing thickness at the position of mean chord of 5%.

Geometric angles of attack were set by rotating the wire wing-stems within the propeller head, and measured using a theodolite, which achieved an estimated accuracy of $\pm 2^\circ$. Angles from 0° to 90° were used, with 10° increments. The angles of incidence were calculated as in Chapter 2.

Frequency and Re

A variable power supply was used to drive the propeller head, using a 22mm diameter, 12V RS motor connected to a 24mm diameter 7.2:1 gearhead. The rotational frequency was varied using the power supply until it met 3.3Hz, as judged with the use of a Drelloscop Strob 2009S07 stroboscope. Rotational frequency was set before and checked after each test. 3.3Hz resulted in a Reynolds number based on the mean chord (Ellington, 1984f) of 1100, close to those estimated from videos of mayflies in ascending flight taken in the field, and reasonable for the parameters described by Brodsky (1973) for the same species.

The mini-spinner for high Re: real and model quail wings

Vertical forces

Vertical forces were measured exactly as for the mayfly wings, except that the moments were opposed with a stiff steel shim on which were glued a pair of strain gauges, instead of the vertical wire leading to the balance: forces were too large and variable for the balance to provide accurate results. Signals from the strain gauges were amplified electronically before being sampled at 50Hz using a Macintosh Quadra 650. Vertical force signals were averaged over 50s. 5 values from 10 paired runs, taking imbalance into account as before, were found for each angle of attack.

Torques

The forces due to the faster, heavier, quail wings were such that the previous method of measuring aerodynamic torques was impossible without adding large masses to stabilise the beam, which resulted in excessive loading on the strain-gauge shim. The torques were high enough, however, to be determined with sufficient accuracy from the power consumption of the motor. The current I passing through, and the voltage V across, the motor were measured 5 times for each angle of attack. The electrical power input (IV) is converted into aerodynamic power by the motor, with certain losses. These motor losses can be categorised (Electro-craft, 1980) as being either speed sensitive (which covers losses due to eddy currents, hysteresis, windage, friction, short circuits and brush contact) or torque sensitive (winding resistance). The speed sensitive components of electrical losses will be a constant C , as a constant rotational frequency was used. C was determined by measuring the electrical power required to drive the motor with no wings attached. The torque-sensitive power loss due to the winding P_{winding} is given by

$$P_{\text{winding}} = I^2 R \quad (3.2)$$

where R is the resistance of the motor. Tests showed that R varied only very slightly with the time spent at the maximum torque, so the internal resistance of the motor did not change due to internal heating. Thus, the value of R taken for the stationary motor can also be used during revolution. Subtracting the two power losses from the power input yields the aerodynamic power P_{aero} required to overcome the aerodynamic torque on the wings:

$$P_{\text{aero}} = (IV) - (I^2 R) - C, \quad (3.3)$$

and torque Q is given by

$$Q = \frac{P_{\text{aero}}}{\Omega}, \quad (3.4)$$

where Ω is the angular velocity of revolution.

Wing design

A 61.6g blue-breasted quail *Coturnix chinensis* was killed by decapitation as part of another study (Askew *et al.* submitted). The right wing (fresh mass 2.29g) was

removed at the base of the humerus and pinned to dry using hypodermic needles. The pinned position mimicked a typical mid-downstroke position determined from the videos of ascending flight used by Askew *et al.* Once stiff, the wing was connected to a rod bent to follow the humerus and radius/ulna with four sutures. It was only possible to use a single wing, as a second right wing accurately matching the first was not available, and the dorsal/ventral asymmetry of bird wings makes use of the left wing inappropriate. In order to balance the propeller, the stem of the rod attached to the wing was allowed to protrude through the propeller head. The wing was only slightly twisted (maximally 3°) but was strongly cambered, particularly at the base. At the ‘elbow’ joint, between humerus and ulna/radius, the wing depth (including camber and thickness) was 28.8% of the chord; at the ‘wrist’, over the alula base, this was 24.1%; half way between the alula and wing tip, 10%.

The wing, once attached to the rod, was scanned (Fig. 3.3B), and the appropriate moments calculated. A print-out of the scanned image was used as a template for a wing model. The model wing was constructed from stiff, thin (0.3mm) card glued to 1.4mm diameter wire running half-way down the ventral surface of the wing. This resulted in a wing thickness at the position of mean chord of 4%. The single model wing was counterbalanced in the same way as the real wing. Again, the propeller head was considered when calculating wing moments (Table 3.4).

Table 3.4. *Morphological parameters for real and model quail wings*

	Quail wing	Real or model quail wing including offset
R (mm)	100.1	104.6
AR	4.52	4.93
$\hat{r}_2(S)$	0.522	0.538
$\hat{r}_3(S)$	0.567	0.580

Angles of attack were set by rotating the wire wing stems within the propeller head, and measured using a theodolite. The arbitrary ‘representative’ α was taken across the wing chord from the base of the alula to the tip of the innermost primary. The angle of incidence α' was calculated as in Chapter 2.

Frequency and Re

The rotational frequency was 12.5Hz, resulting in a Re of 26 000 based on the mean chord. Askew *et al.* (submitted) have observed a maximum downstroke angular flapping velocity ω of $190 \text{ }^\circ \text{ s}^{-1}$ for a quail with a wing length of 95mm. This corresponds to a maximum Re of 48 000, so 26 000 for the propeller implies it is operating in a similar regime to the flapping wing for most of the downstroke. The upstroke has little aerodynamic effect.

Results

AR series

Fig. 3.4 shows ‘Early’ and ‘Steady’ results for the *Manduca* wings with a range of aspect ratios. In each case, the ‘pooled’ data for the flat *Manduca* wings shown in Chapter 2 are presented (both ‘Early’ and ‘Steady’ values) for comparison. The shift between ‘Early’ and ‘Steady’ values seen at intermediate angles of incidence for the standard *Manduca* wings is visible for all aspect ratios. The relationship between both $C_{h,Early}$ and $C_{h,Steady}$ (Fig. 3.4A and C) with α' at low angles is very consistent for wings of every AR tested. However, under both conditions, aspect ratio has a progressively greater effect at higher α' . Low AR wings achieve considerably higher maximum horizontal force coefficients, peaking at $C_{h,Early} = 3.4$ and $C_{h,Steady} = 3.5$ near $\alpha' = 90^\circ$, while the highest AR wings achieve maximum horizontal force coefficients of only 2.5.

The relationship of both $C_{v,Early}$ and $C_{v,Steady}$ (Fig. 3.4B and D), with α' is dependent on aspect ratio. While the maximum values reached, around 1.7 for $C_{v,Early}$, and 1.3 for $C_{v,Steady}$, are very close for the entire range of aspect ratios, and occur at similar α' , between 40° and 60° , the initial gradients differ significantly. The relationships are approximately linear between $\alpha' = -20^\circ$ and $+20^\circ$. The gradients $dC_v/d\alpha'$, with their 95% confidence intervals over this range are given in Fig. 3.5. Lower AR wings, and wings in ‘steady’ revolution, have lower gradients.

Bombus results

Fig. 3.6 shows the results for the *Bombus* wings. C_h and C_v , both ‘Early’ and ‘Steady’, show remarkably little differences compared with the ‘pooled *Manduca*’ results from Chapter 2.

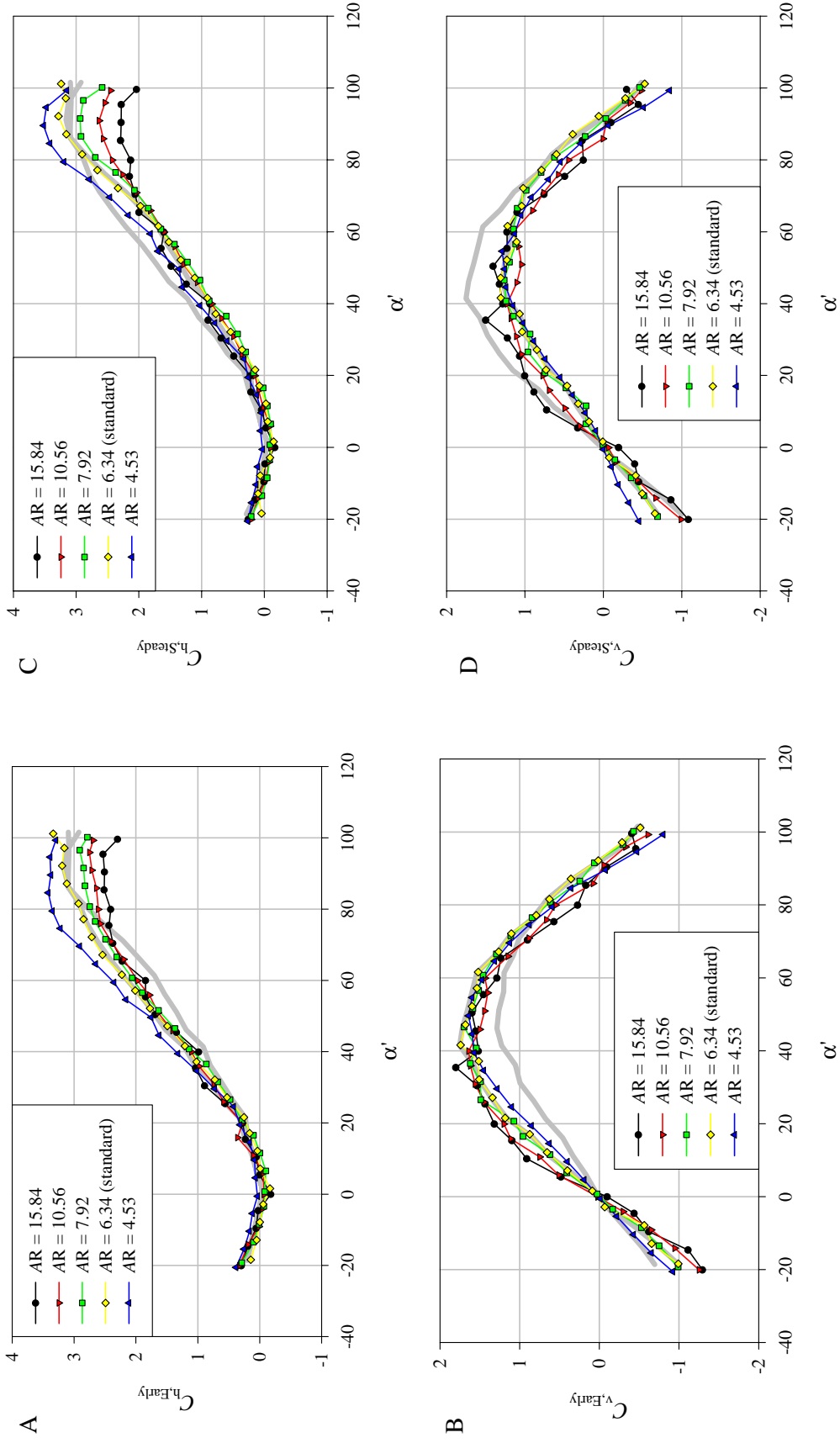


Fig. 3.4. Horizontal (A and C) and vertical (B and D) ‘propeller’ force coefficients for a range of α' under ‘Early’ (A and B) and ‘Steady’ (C and D) conditions for model *Manduca* wings with a range of aspect ratio. Grey lines show ‘Early’ and ‘Steady’ coefficients for ‘Pooled’ standard *Manduca* from Chapter 2.

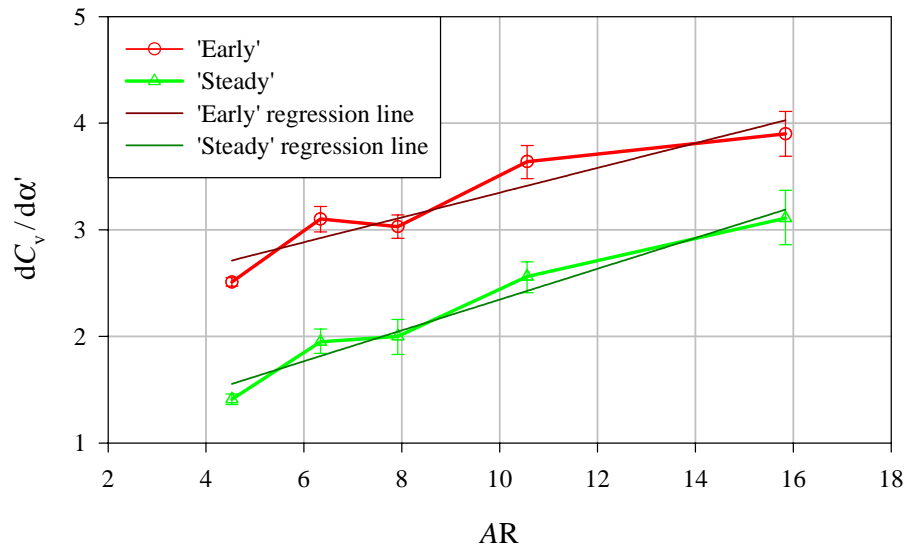


Fig. 3.5. $dC_v/d\alpha'$ for 'Early' and 'Steady' conditions from $\alpha' = -20^\circ$ to $+20^\circ$ for model *Manduca* wings with a range of aspect ratios. Bars show 95% confidence intervals. Differences both between high and low aspect ratios for either condition, and between 'Early' and 'Steady' conditions for each aspect ratio, are significant. The regression slopes of $dC_v/d\alpha'$ by AR for 'Early' and 'Steady' conditions are not significantly different, and average 0.130.

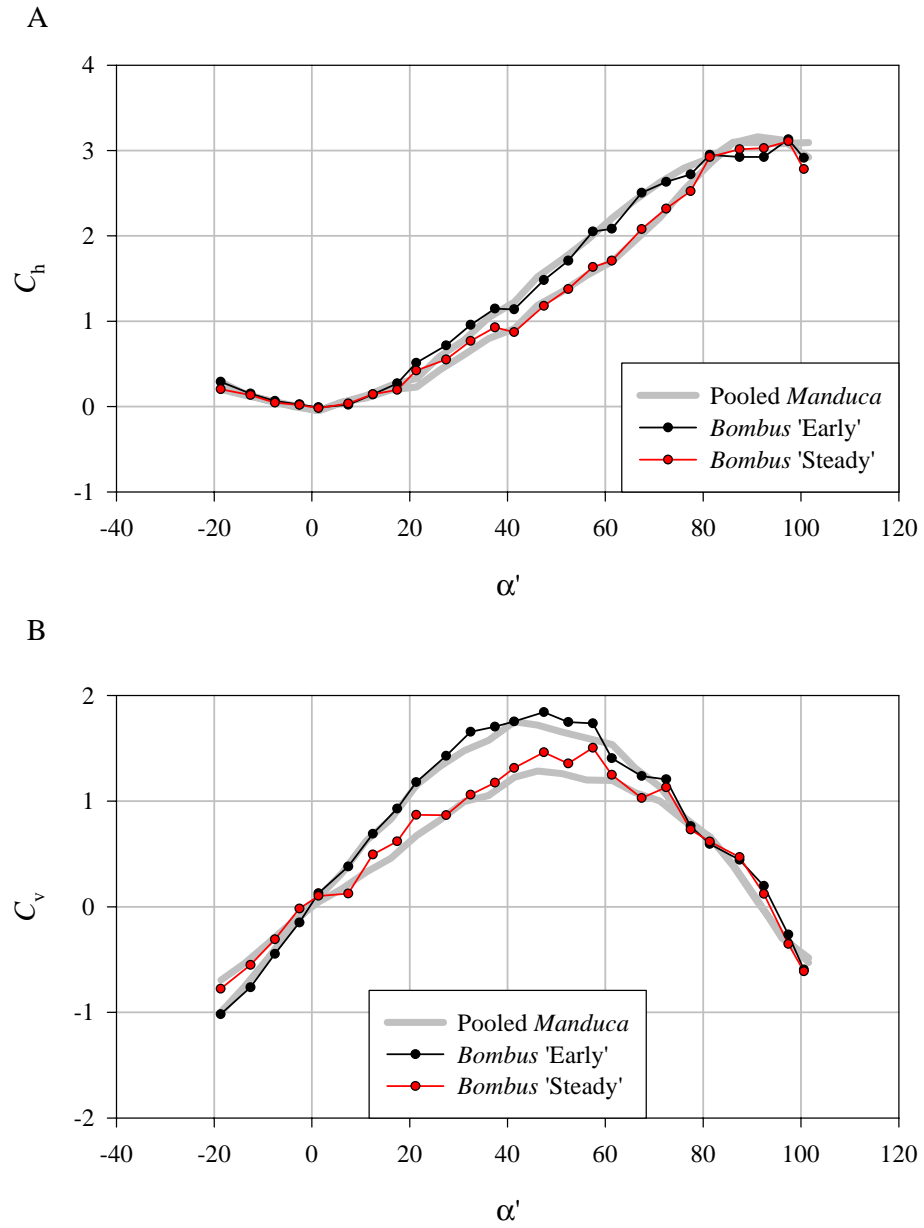


Fig. 3.6. Horizontal (A) and vertical (B) force coefficients under 'Early' and 'Steady' conditions for model *Bombus* wings. Grey lines show 'Early' (higher) and 'Steady' (lower) coefficients for standard 'pooled' *Manduca*.

Steady results for range of species

Fig. 3.7 shows the ‘Steady’ force coefficients for the model mayfly and model and real quail wings derived from force measurements using the ‘mini-spinner’. These are plotted with the ‘Steady’ coefficients for *Bombus* and pooled *Manduca* wings. Slight differences are visible in the horizontal force coefficients, with the mayfly showing lower coefficients (though with high standard errors), and the quail higher. The relationship between $C_{v,Steady}$ and α' was remarkably consistent for the whole range of wings tested. All wings achieved maximum vertical force coefficients well above 1 at α' between 40° and 60° .

Deflections were visible in the revolving quail wings, with the tips of both real and model wings bending backwards, especially at higher values of α . The values of α' shown for the quail wings in Fig. 3.7 must therefore be considered approximate.

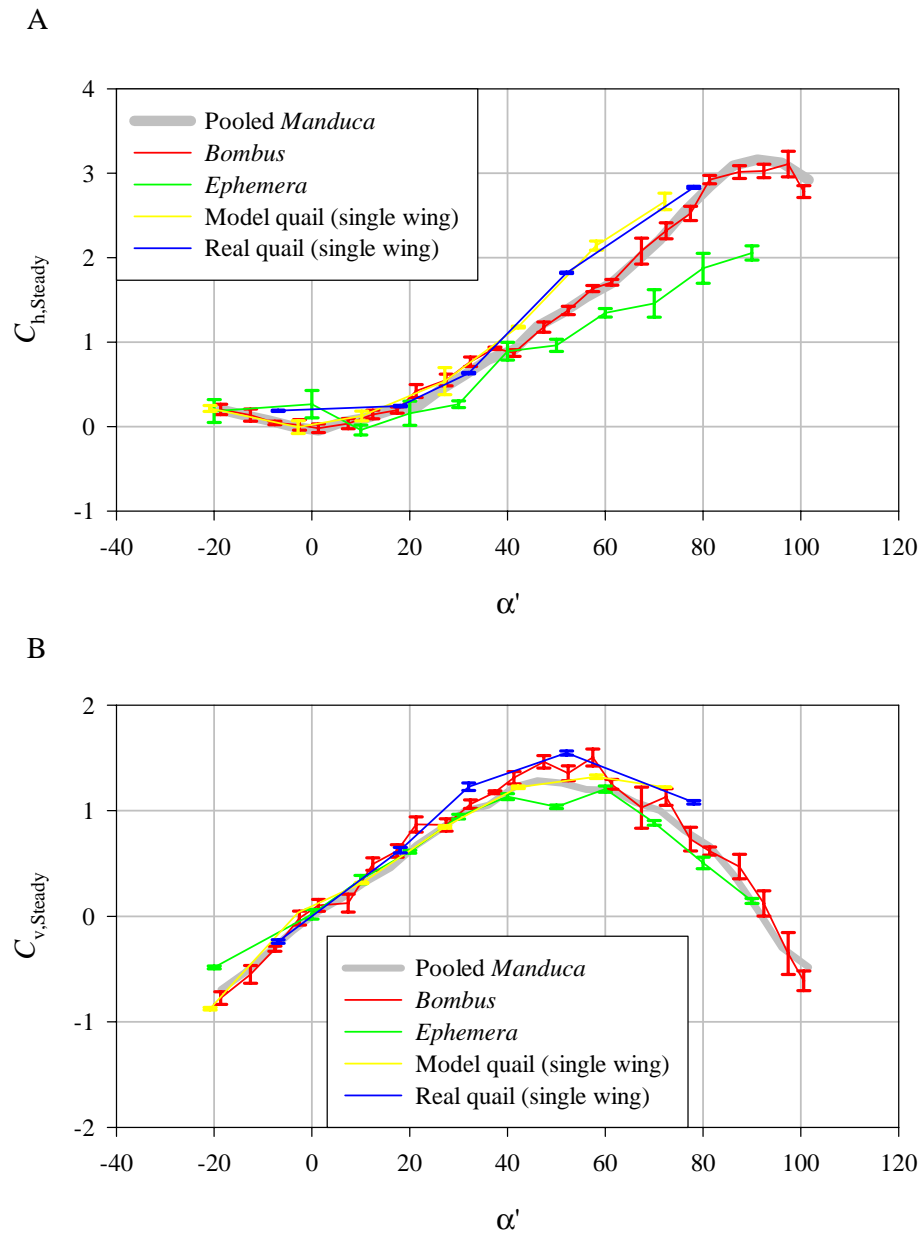


Fig. 3.7. Steady horizontal (A) and vertical (B) propeller coefficients for a range of wing types. Error bars show ± 1 standard error.

Discussion

Steady high-lift mechanisms exist for a wide range of revolving wings

Force coefficients for AR range

Aspect ratio appears to have remarkably little effect on the force coefficients that can be achieved by revolving wings. Wings from $AR = 4.53$ to 15.84 produce indistinguishable maximum vertical force coefficients between $\alpha' = 40^\circ$ and 60° of 1.70 ('Early') and 1.30 ('Steady'). There is no distinct reduction in force coefficients that would be associated with 'stall', at least below $\alpha' = 65^\circ$ (and so of any relevance to insects hovering with a horizontal stroke plane), even for wings of very high AR . Above this angle, however, low AR wings achieve higher force coefficients, which are dominated by C_h . At $\alpha = 90^\circ$, there is a considerable range in C_h : for $AR = 15.84$, $C_{h,Early} = 2.53$, and $C_{h,Steady} = 2.29$; for $AR = 4.53$, $C_{h,Early} = 3.42$, and $C_{h,Steady} = 3.52$. For the lower aspect ratio wings, these values are well above those predicted for flat plates in steady translational flow. Ellington (1991) gives an approximate relationship for the drag coefficient of an infinite flat plate $C_{D,FP}$ appropriate for Re in the range of 10^2 to 10^3 :

$$C_{D,FP} = 1.95 + \frac{50}{Re} \quad (3.5)$$

where $C_{D,FP}$ should be equivalent to $C_{h,steady}$ at $\alpha'=90^\circ$. Re is at least several thousand for the wings described here, so the predicted horizontal force coefficient is very close to 2 and varies only slightly over the range of Re covered by the wings. Furthermore, the 3-d effect of air 'sneaking' around the ends of the wing instead of flowing around its width would lead to even lower values of C_h (Hoerner, 1958), and incorrectly predict the direction of the relationship between maximum C_h and AR .

These results suggest that blade-element analyses of revolving, perpendicular 'wings' may be in serious error if conventional, steady, 2-d force coefficients are used. In particular, older analyses of pectoral-fin swimming in fish (Blake, 1978) may have to be re-assessed.

Bumblebee force coefficients

The measurements made on the *Bombus* wings are near the lower limits of the large propeller rig. However, all propeller coefficients ($C_{h,Early}$, $C_{h,Steady}$, $C_{v,Early}$ and $C_{v,Steady}$) agree so well with the values found for *Manduca* that little comment is possible, other than to observe that similar aerodynamic mechanisms are almost certainly available to bumblebees and hawkmoths.

Steady force coefficients from mayfly to quail

Remarkably consistent, high force coefficients are achieved for simple, thin, flat, model wings in steady revolution at Re from 1100 to 26 000. The real quail wing, with thickness and camber, not to mention feathers, produce very similar force coefficients. Drovetski (1996) gives polars from 0° to 25° for simple model galliform (game bird) wings. The videos of Askew *et al.* (submitted) (and, consequently, the wing and wing model used in this study) do not show the trailing-edge notch described by Drovetski; it appears that such a notch is only present in gliding flight, or is an artefact of pinning the wings in a fully extended position. The maximum lift coefficients cited by Drovetski for wing models ranging from California quail *Callipepla californica* to turkey *Meleagris gallopavo* were from 0.61 to 0.80; it seems that some aspect of revolution may as much as double the vertical force coefficients. Values for blackbird *Turdus merula*, house sparrow *Passer domesticus* and mallard *Anas platyrhynchos* (Nachtigall and Kempf, 1971), range from 0.9 to 1.1: higher than Drovetski's galliforms, but still considerably under those for revolving quail wings.

Further implications of aspect ratio

$dC_v/d\alpha'$ and aspect ratio

Fig. 3.5 shows relationships between aspect ratio and the rate of change of vertical force coefficient with angle of incidence, $dC_v/d\alpha'$. The relationship for both 'Early' and 'Steady' conditions are very similar; the gradients for regression lines

through each plot on Fig. 3.5 are not significantly different. This phenomenon is well known for translating wings: higher aspect ratio wings, for the same vertical force and angle of incidence, are longer, and so sweep a larger volume of air per unit time; from momentum considerations it is clear that the associated downwash velocity is lower for higher AR wings, which results in a smaller downwash angle ε , and so a greater increase in ‘effective angle of incidence’ ($\alpha'_e = \alpha' - \varepsilon$) for a given increase in angle of incidence α' . In the propeller case described here, the wing length is held constant, but the same principles apply: higher aspect ratio wings have smaller areas, and so produce smaller forces (but similar coefficients) for a given angle of incidence. A smaller downwash velocity, and a smaller downwash angle, is associated with the smaller forces, and the *effective angle of incidence* is closer to the *angle of incidence* for higher AR wings; with increasing α' and increasing vertical forces, higher AR wings are less affected by downwash, and so $dC_v/d\alpha'$ is higher. The presence of the $dC_v/d\alpha'$ relationship for ‘Early’ conditions does show that the ‘Early’ induced downwash, while small, is not negligible; $C_{h,Early}$ and $C_{v,Early}$ therefore provide slight under-estimates for $C_{D,pro}$ and C_L (see Chapter 2). However, the significance of this effect is minor compared with the surprisingly similar magnitudes of force coefficients for the AR range discussed above.

Implications of aspect ratio to wing design

The similarity in aerodynamic characteristics of wings with a considerable range of aspect ratio for $\alpha' < 65^\circ$ suggests that, all other factors being equal (an unrealistic position in biology, but useful in determining the evolutionary pressures involved with wing design), lower AR wings should support body weight with less power than higher AR wings. For a given wing length R , the vertical force F_v in hovering is proportional to

$$F_v \propto S n^2, \quad (3.6)$$

while the aerodynamic power P_{aero} is proportional to

$$P_{aero} \propto S n^3: \quad (3.7)$$

see equations (2.7), (4.3) and (4.14). Therefore the power required to support a given body weight is proportional to wingbeat frequency n ($\propto P_{aero} / F_v$). The frequency and

hence the power can be reduced by increasing wing area S (equation (3.6)) which, for a given wing length, is equivalent to decreasing the AR (equation (3.1)):

$$\frac{P_{\text{aero}}}{F_v} \propto n \propto \sqrt{AR} \quad (3.8)$$

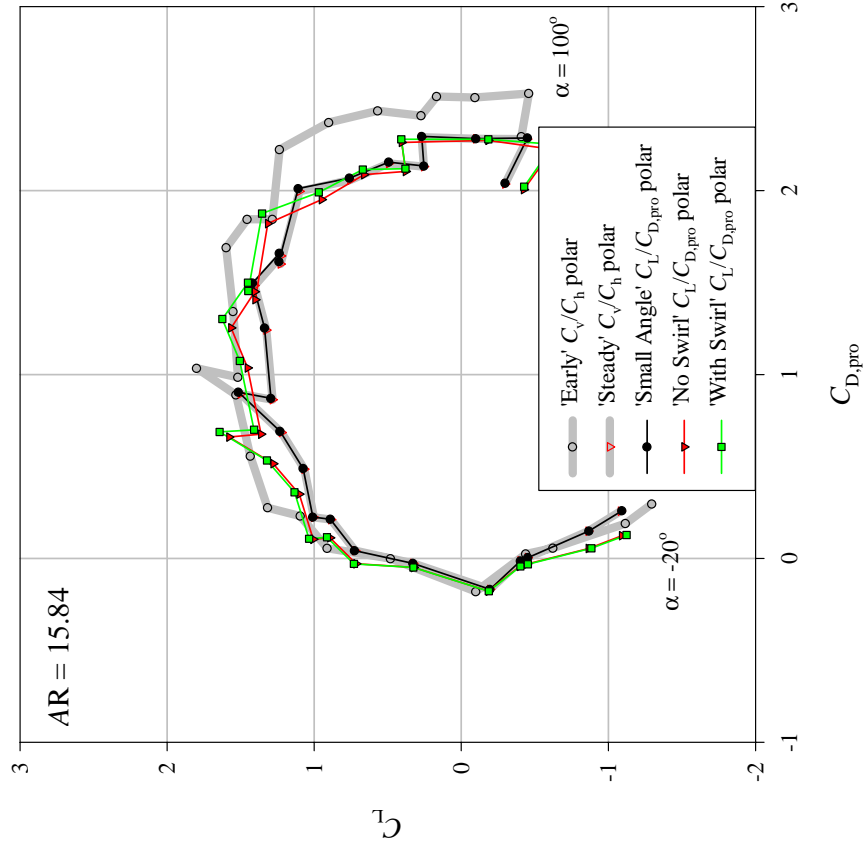
Clearly many other aspects influence wing design in insects: adaptive aspect ratios may be determined by inertial power or weight considerations, or the energetics of unsteady- or forward-flight aerodynamics; and aspect ratios may be constrained due to biologically important pressures such as wing strength, toughness, visibility. However, the above relationships do suggest a possible pressure towards broader wings on insects for which efficient hovering with a horizontal stroke plane is of selective significance.

The energetic advantage to butterflies of low aspect ratio wings is clearer. The large cabbage white *Pieris brassicae* hovers with a vertical stroke plane (Ellington 1984a), which means that horizontal force coefficients as defined here act in the vertical plane. While use is made of unsteady mechanisms such as the ‘clap and fling’, the benefits due to a low AR wing can be seen by considering steady propeller coefficients. The lowest AR wing tested had a maximum horizontal force coefficient of 3.52, 1.4 times that of the highest AR wing. Thus, lower aspect ratio wings produce larger forces both because of their larger areas and their higher force coefficients. This should allow the butterfly to flap disproportionately slowly, lowering the power requirements for hovering.

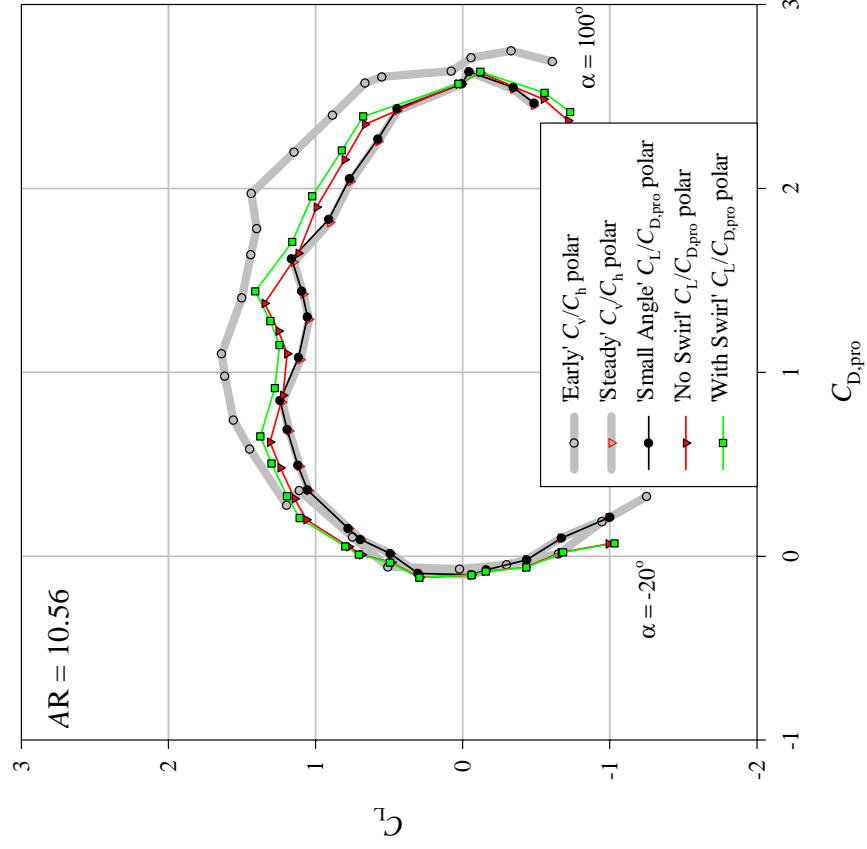
Conversion of propeller coefficients into $C_{D,\text{pro}}$ and C_L

Fig. 3.8 shows the results for the AR range of the three aerodynamic models described in Chapter 2 that convert $C_{h,\text{Steady}}$ and $C_{v,\text{Steady}}$ into $C_{D,\text{pro}}$ and C_L . At α' above 50° , the models progressively underestimate C_L with increasing AR. However, both large-angle models give good fits to $C_{h,\text{Early}}$ and $C_{v,\text{Early}}$ for values of α' below 50° , which are more realistic for hovering insects.

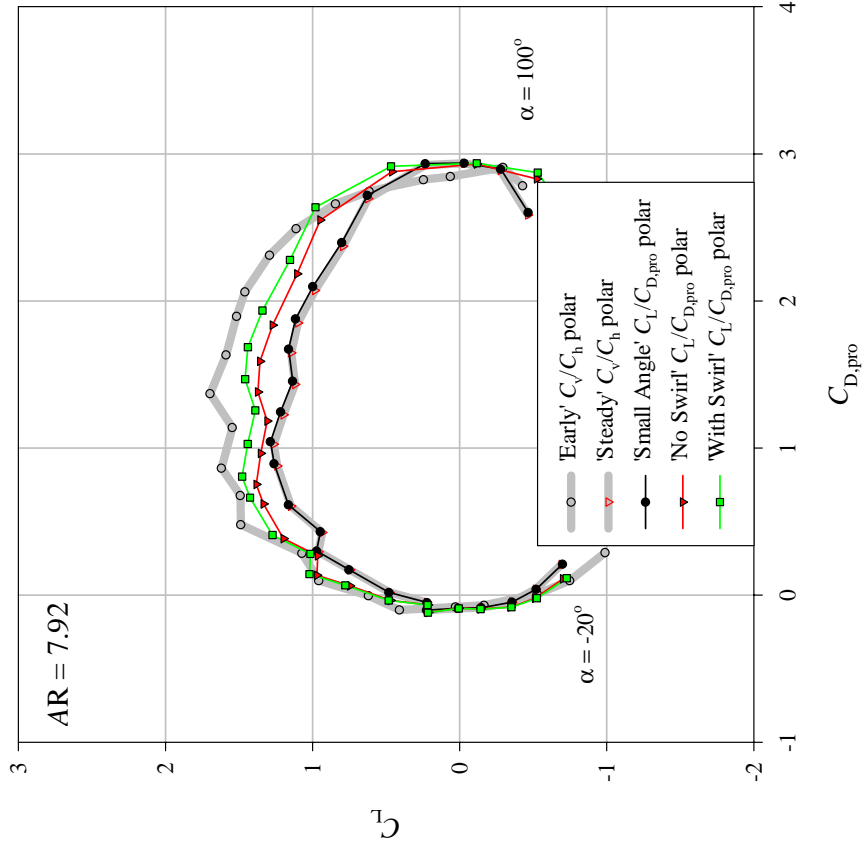
A



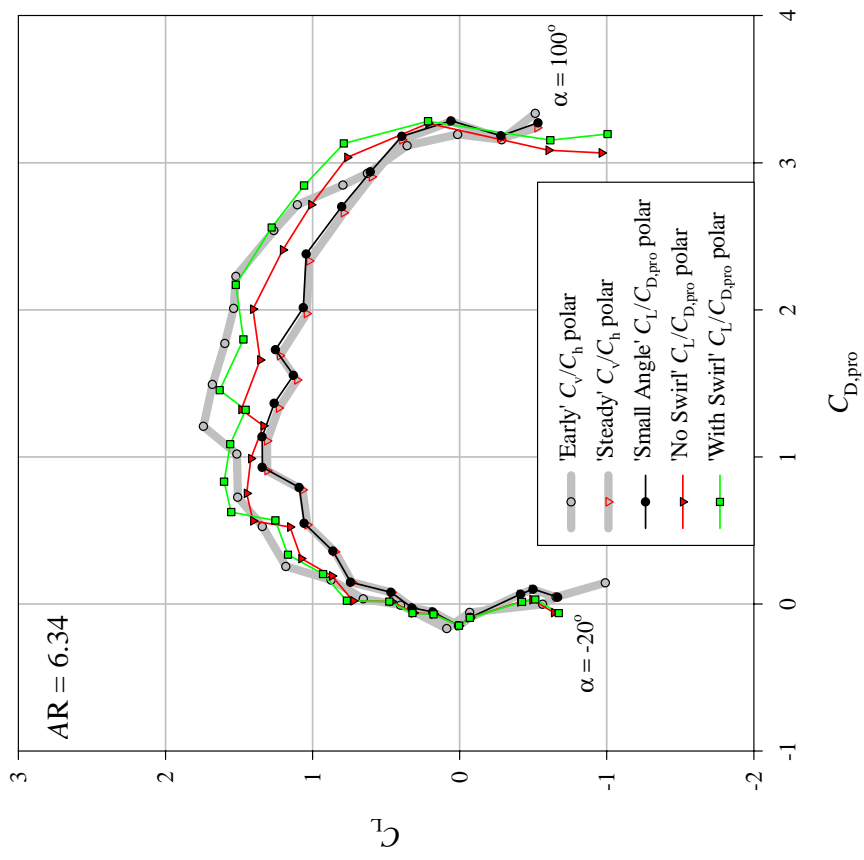
B



C



D



E

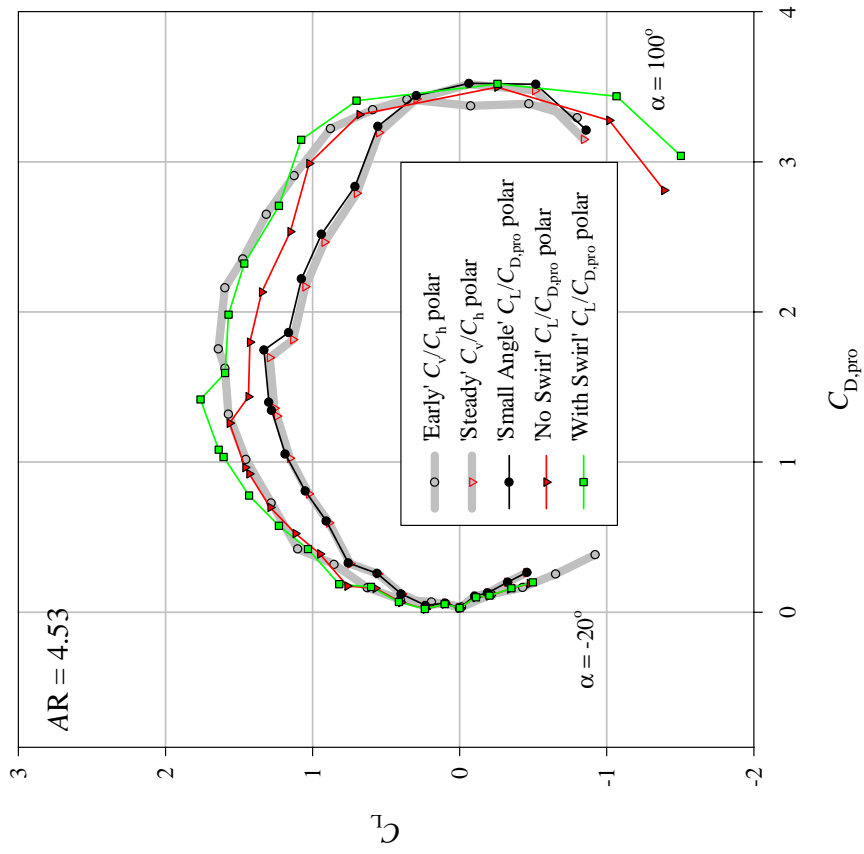


Fig. 3.8. Conversion of 'Steady' propeller coefficients into conventional profile drag and lift coefficients using the models described in Chapter 2 for a range of aspect ratio.

The ‘normal force relationship’ is unaffected by induced downwash

The ‘normal force relationship’ between C_h , C_v and α described for standard *Manduca* wings in Chapter 2 is also accurate at very low Re (Dickinson *et al.* 1999) at high angles. The effectiveness of the model for different AR, and its insensitivity to induced velocities, is shown in Fig. 3.9: the observed resultant force coefficient C_R can be accurately divided into C_h and C_v by

$$C_h = C_R \sin(\alpha) \quad (3.9)$$

and

$$C_v = C_R \cos(\alpha) \quad (3.10)$$

respectively. The fits are very good, even at very high α' , despite the various induced air-velocities associated with the range of AR and ‘Early’ and ‘Steady’ conditions.

High force coefficients as a robust phenomenon

The aerodynamic phenomenon, or phenomena, resulting in high force coefficients, appears remarkably robust; wings with a considerable range of planform, Re leading-edge detail, twist, camber and thickness, achieve very similar force coefficients. Some of the force measurements on the flapping *Drosophila* model of Dickinson *et al.* (1999) are equivalent to the ‘Early’ measurements described here, and their ‘simple harmonic relationships’ are shown with the ‘Early’ results for the *Manduca* AR range in Fig. 3.10. The *Drosophila* model shows an appreciable minimum horizontal force coefficient at low values of α , presumably due to relatively larger viscous forces. However, at higher values of α' there is very good agreement in both C_h and C_v with the values shown for *Manduca* planforms. If it is reasonable to suppose that shifts from ‘Early’ to ‘Steady’ conditions are relatively constant throughout the Re range, then it appears that similar force coefficients are possible right from *Drosophila* ($Re \approx 200$) to quail ($Re \approx 26\,000$). While the flow structure for the full range of wings has not been visualised, it is tempting to suggest that separation from the leading-edge, roll-up into leading-edge vortices, and maintenance of LEVs through strong spanwise flow, might all be similar for the complete range.

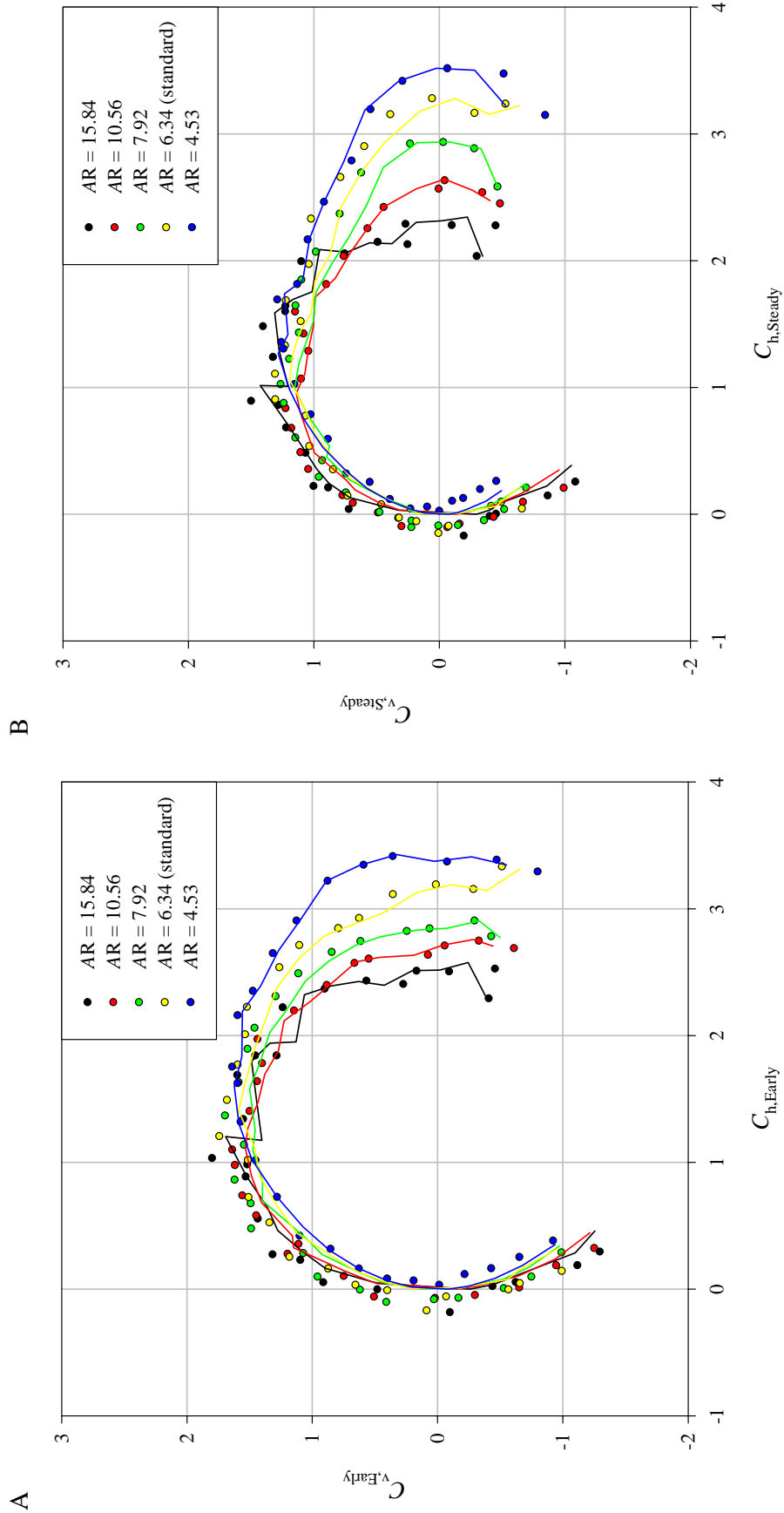


Fig. 3.9. Polar diagrams for model *Manduca* wings with a range of aspect ratio under ‘Early’ (A) and ‘Steady’ (B) conditions. Points give the measured values; lines are derived from the normal force relationship.

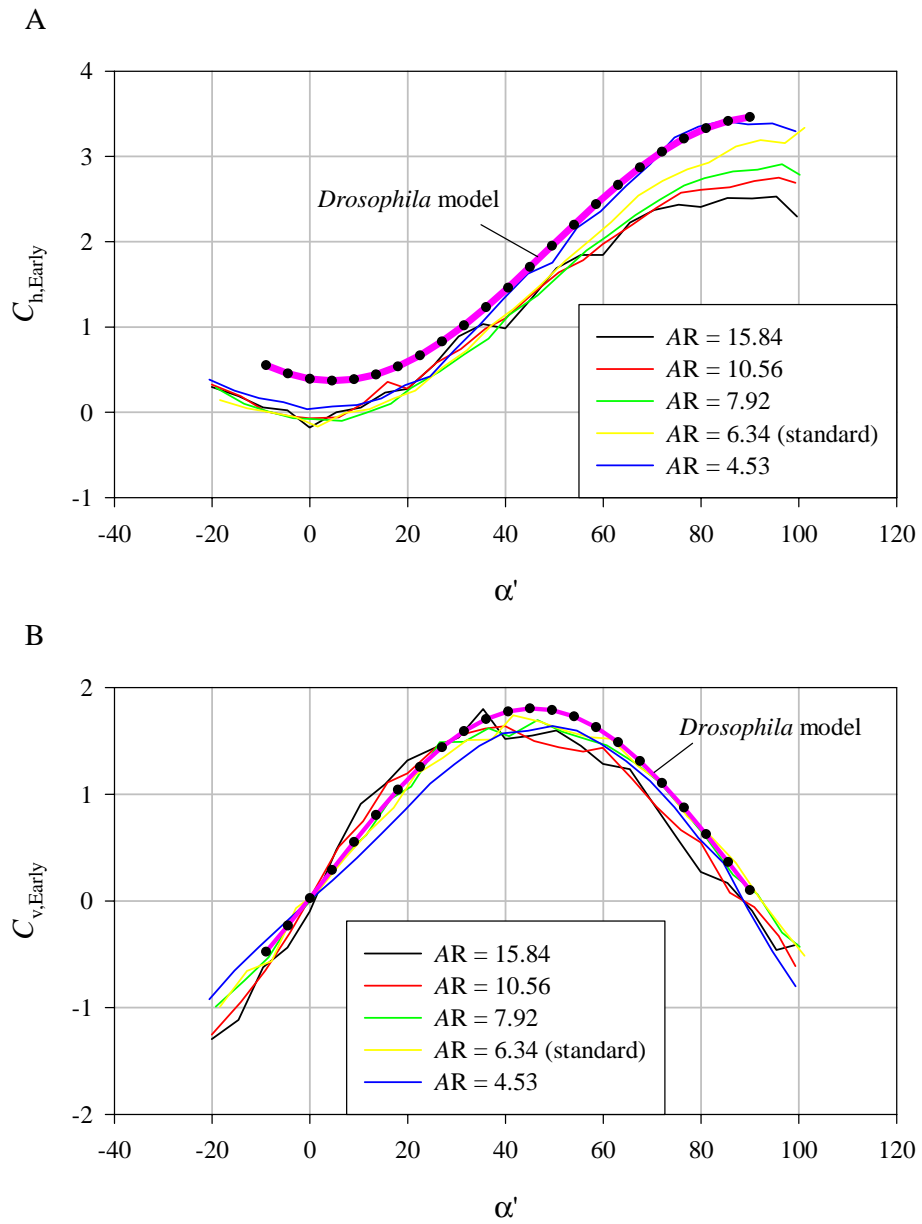


Fig. 3.10. ‘Early’ horizontal (A) and vertical (B) propeller coefficients for model *Manduca* wings with a range of aspect ratios. The model relationship given by Dickinson *et al.* (1999) for *Drosophila* is overlaid.

Flow separation from the leading-edge is a reasonable assumption at the high α s typical of hovering, and the orientation of the resultant force perpendicular to the wing surface does suggest loss of leading-edge suction associated with flow separation. Assumptions about details of any (or many) LEVs should be made with more caution, however, as similarity in force production may not imply similarity in flow structure: recent work on flapping *Drosophila* model (Birch and Dickinson, 2001) suggests that, while LEVs are observed, the strong spanwise flow described for flapping and revolving *Manduca* wings (Chapter 2) may not be present. In any case, if the mechanism for these high force coefficients is indeed associated with the production and maintenance of LEVs (which has been observed for the *Drosophila*, flapping, and revolving *Manduca* wings), then the insensitivity to Re is not as surprising as it may appear. LEVs over sharp, thin delta wings are effective lift-producers for slow paper aeroplanes, Concorde and the space shuttle; a vast range of Re .

Conclusion

Revolving wings of a remarkable variety of designs have very similar aerodynamic characteristics. High force coefficients, similar to those observed for revolving model *Manduca* wings in Chapter 2 (for which steady leading-edge vortices are directly observed), are apparent for mayfly, bumblebee, and quail wings, along with wings based on *Manduca* ranging in AR from 4.53 to 15.84. ‘Early’ propeller coefficients for model bumblebee and hawkmoth wings agree very closely with values previously described for model *Drosophila* wings.

The normal force relationship introduced in Chapter 2 is supported for wings over a full range of AR, in both ‘Early’ and ‘Steady’ conditions; local induced velocities appear not to affect the relationship.

Chapter 4: The ‘normal forces model’. A new method for estimating the power requirements of slow, flapping flight.

Introduction

Slow, hovering, and ascending flight are the most energetically demanding forms of locomotion known. Energetic (rather than aerodynamic) limitations appear to determine the maximum sizes at which hovering and vertical flight is achievable; while many larger birds and bats can hover momentarily, only the smaller species manage to do so aerobically in still air. The power requirements for hovering and slow flight, therefore, have implications for muscle performance (power and efficiency), whole-animal behaviour and ecology, and evolutionary constraints and pressures.

Traditional approaches to power estimates for slow flight

Modern techniques for the analysis of the energetics of animal flight (e.g. Pennycuik, 1972, 1975; Rayner, 1979a-c; Ellington, 1984a-f) divide the mechanical power requirements into ‘parasite’, ‘induced’ (which may also include ‘climbing’), ‘profile’ and ‘inertial’ powers (see Casey, 1981). Parasite power, due to body drag, is normally considered negligible for hovering and very slow flight. The induced power P_{ind} for hovering ‘represents the cost of imparting sufficient downwards momentum to the surrounding air so as to offset the body weight’ (Dudley, 2000). Variations on the ‘Rankine-Froude’ model (originally developed for propeller analysis) are traditionally used. For instance Ellington (1984e) describes, for hovering,

$$P_{\text{ind}} = k_{\text{ind}} mg \sqrt{\frac{mg}{2 \rho A_0}}. \quad (4.1)$$

where mg is the weight of the animal (of mass m in a gravitational field g , normally taken to be 9.81 m s^{-2}), ρ is the density of air, and A_0 is the area swept by the wings projected on to the horizontal plane. For a pair of flapping wings, each of length R , wingstroke amplitude Φ and stroke plane inclination β ,

$$A_0 = \Phi R^2 \cos(\beta). \quad (4.2)$$

The constant k_{ind} is a correction factor which takes into account uneven downwash distributions (e.g. Stepniewski and Keys, 1984) along with the effects of wake periodicity. Wake periodicity is likely to be particularly important for birds and bats hovering with an inclined stroke plane, as they produce the majority of the weight-supporting forces during the downstroke, instead of spreading them evenly between up- and downstroke (as do most insects and hummingbirds). Rayner (1979a-c) and Ellington (1984f) describe different approaches to determining induced power requirements based on vortex theory. However, Ellington showed that both methods provide results reasonably convergent with those from equation (4.1).

Profile power P_{pro} is usually calculated using a ‘blade-element’ approach, where the profile power due to an element of area S' and relative air velocity U_r is given by

$$P_{\text{pro}} = \frac{\rho}{2} S' U_r^3 C_{D,\text{pro}} \quad (4.3)$$

where $C_{D,\text{pro}}$ is the profile drag coefficient. Conventional values of $C_{D,\text{pro}}$ are derived from wind-tunnel tests on wings, in two-dimensional, steady flow. $C_{D,\text{pro}}$ is either taken to be the minimum value of C_D , or (at higher angles of attack) is the remaining drag coefficient after the effects of ‘induced drag’ (the drag associated with P_{ind}) are removed.

The term ‘Inertial power’ P_{acc} is conventionally used (Ellington, 1984f) to account for the energy required to periodically accelerate the wings. Energy must be put into the rotational kinetic energy of the wings each time they accelerate (each half-stroke). While the same amount of energy must be associated with the deceleration phase of each half-stroke, it is usually assumed that this ‘negative’ work can be achieved with relatively slight cost: it is supposed that the energy can be dissipated internally, or into the air (offsetting some of the aerodynamic costs, see below). So, the expression given by Ellington (1984f)

$$P_{\text{acc}} = 2 m_2 \omega_{\text{max}}^2 n, \quad (4.4)$$

where n is the flapping frequency and m_2 is the second moment of wing mass (Ellington, 1984b) (sometimes termed the moment of inertia), provides an estimate of the power required to overcome the *metabolic* costs of wing acceleration. ω_{max} is the maximum angular velocity, given by

$$\omega_{\max} = \Phi \pi n \quad (4.5)$$

for sinusoidal kinematics.

Some ‘virtual mass’ is usually included with m_2 in analyses of insect power requirements, to take account of the mass of air which is accelerated and decelerated with the wing. Previous estimates have been derived for accelerating aerofoils in 2-dimensional flow, however, so the validity of such values in the strongly 3-dimensional flow observed for revolving insect-like wings (Chapter 2) is questionable. As a result, ‘virtual mass’ is ignored in this analysis other than to note that, if the 2-dimensional values were to be included, the effects would be relatively slight.

The manner in which the power components should be combined depends on the relative magnitude of P_{acc} to the sum of the aerodynamic (induced and profile) power components P_{aero} . At one extreme (Ellington, 1984f), where $P_{\text{acc}} > P_{\text{aero}}$ the kinetic energy imparted to the wings is greater than the aerodynamic work required during wing acceleration. If the excess kinetic energy is simply dissipated or absorbed by the muscles for negligible metabolic cost, the total power requirement P is

$$P = \frac{1}{2}(P_{\text{acc}} + P_{\text{aero}}). \quad (4.6)$$

Alternatively, an elastic mechanism could be used to ‘brake’ the wings, storing the excess energy as elastic strain energy, and used to accelerate the wings for the next half-stroke. For perfect elastic storage the net inertial power requirement is zero over the half-stroke, and the total power requirement is simply the aerodynamic power:

$$P = P_{\text{aero}} \quad (4.7)$$

However, values for elasticity are unreliable (although estimates have been attempted: Dickinson and Lighton, 1995), and most studies therefore provide power calculations for both 0% and 100% elasticity, thus covering both ends of the spectrum.

At the other extreme (Dudley and DeVries, 1990), when $P_{\text{acc}} < P_{\text{aero}}$, the kinetic energy imparted to the wings can be recovered as aerodynamic work during deceleration. There is no excess energy, so recovery is complete and there is no net inertial cost. The total power is then equal to P_{aero} again, as in equation (4.7).

The present study

Force measurements made on revolving wings at high incidences (Chapters 2 and 3) show that the forces acting on a wing can be described by a single resultant force, which acts ‘normal’ or perpendicular to the wing surface. This is due to the loss of ‘leading-edge suction’ (discussed in Chapter 2), presumably associated with flow separation at the leading-edge, which results in forces being dominated by the pressure difference between upper and lower surfaces. Where previous studies have treated the two forms of aerodynamic drag, profile and induced, separately, the ‘normal pressure force’ can be used to combine considerations of induced drag and profile drag, and relate them directly to the vertical force balance and the geometric angle of attack. This allows an estimate of the aerodynamic power of hovering flight for a wide range of animals, without knowledge of the specific aerodynamic properties for each wing type.

The model presented in this study takes two forms. The first applies to animals which use ‘normal hovering’ (a term used by Weis-Fogh, 1973), in which the stroke plane is horizontal, and the upstroke and downstroke contribute equally to force production. Such hovering is typical for the majority of insects that have been studied, and also of hummingbirds. The second form applies to animals that hover with an inclined stroke plane (Ellington, 1984f), in which force production is dominated by the downstroke. This form applies to the majority of vertebrates capable of hovering, though the degree to which the upstroke plays a part in force production remains uncertain for many animals.

Methods

General assumptions

The models presented here are based on the assumption that force coefficients for flapping wings may be treated as being ‘quasi-steady’: the instantaneous forces acting on a flapping wing are assumed to be the same as those which would be experienced by a similar wing revolving in a propeller-like manner at the appropriate angular velocity. Using a ‘blade-element’ approach, the horizontal force F_h' and vertical force F_v' acting on a wing-element at a spanwise position r , with a width dr and chord c , can be described by

$$F_h' = \frac{\rho}{2} C_h \omega^2 r^2 c dr \quad (4.8)$$

and

$$F_v' = \frac{\rho}{2} C_v \omega^2 r^2 c dr \quad (4.9)$$

respectively, where ω is the instantaneous angular velocity of the revolving wing. C_h and C_v are horizontal and vertical force coefficients respectively, which equate to $C_{D,pro}$ and C_L in the absence of a downwash. When describing forces and coefficients, the term ‘horizontal’ applies to forces acting within the stroke plane, and ‘vertical’ refers to forces perpendicular to that plane. These definitions are particularly important when considering the model for an inclined stroke plane; in this case ‘horizontal’ and ‘vertical’ are *not* related to the conventional, gravity-based, frames of reference.

A ‘mean coefficients’ approach is adopted (following Osborne, 1951) so that the instantaneous total horizontal and vertical forces for a wing pair can be given by

$$F_h = \frac{\rho}{2} C_h \omega^2 S_2 \quad (4.10)$$

and

$$F_v = \frac{\rho}{2} C_v \omega^2 S_2 \quad (4.11)$$

respectively, where S_2 is the second moment of wing area for both wings (Ellington, 1984b)

$$S_2 = 2 \int_0^R r^2 c \, dr. \quad (4.12)$$

F_h is comprised of both profile drag and induced drag, and it is the source of aerodynamic torque and power. The power P_{aero} to revolve a wing against aerodynamic drag is

$$P_{\text{aero}} = \omega Q \quad (4.13)$$

where Q is the aerodynamic torque. As each F_h' produces a torque by acting about a moment arm of length r , P_{aero} is given by

$$P_{\text{aero}} = \frac{\rho}{2} C_h \omega^3 S_3, \quad (4.14)$$

where S_3 is the third moment of wing area for both wings (Ellington, 1984b):

$$S_3 = 2 \int_0^R r^3 c \, dr. \quad (4.15)$$

The normal force relationship

The models presented below rely on the determination of mean values of C_v from simple force balances, from which corresponding values for C_h can be derived using the ‘normal force relationship’ found to be robust in Chapters 2 and 3. The normal force relationship

$$C_h = C_v \tan(\alpha), \quad (4.16)$$

where α is the geometric angle of attack, holds well for relatively thin wings operating at high angles of incidence. This appears appropriate for all animals capable of hovering and slow flight, especially for the outer parts of the wing, which dominate force production.

Models

Hovering with a horizontal stroke plane: most insects and hummingbirds

The initial form of this model applies to animals hovering with a horizontal stroke plane, in which the downstroke and upstroke contribute equally to lift production: ‘normal’ hovering *sensu* Weis-Fogh (1973). This appears to be a fairly accurate description of hovering in many insects (Ellington, 1984c), including ladybirds *Coccinella*, craneflies *Tipula*, honey bees *Apis*, bumblebees *Bombus*, droneflies *Eristalis* and, occasionally, hoverflies *Episyrphus*. It is assumed that α is set early in the half-stroke, is similar for up- and downstroke, and remains constant throughout the half-stroke. These assumptions are valid for *Drosophila* (Vogel, 1967a) and hummingbirds (Hertel, 1966), and generally tend to be more accurate for the downstroke than the upstroke. They imply that constant mean values of C_h and C_v act throughout both half-strokes, and that the normal force relationship maintains a $C_v:C_h$ ratio which can be calculated given α .

C_v can be determined given that, for steady hovering flight, the upward thrust equals the weight of the hovering animal. In the case of a horizontal stroke plane, then,

$$mg = F_v = \frac{\rho}{2} C_v S_2 \overline{\omega^2}, \quad (4.17)$$

where $\overline{\omega^2}$ is the mean square of angular velocity. So, a mean value of C_v can be calculated from

$$C_v = \frac{2 mg}{\rho S_2 \overline{\omega^2}}, \quad (4.18)$$

and the mean C_h may be derived from the normal force relationship (equation (4.16)). Combining equations (4.14), (4.16) and (4.18), this gives

$$P_{\text{aero}} = \frac{mg S_3 \overline{\omega^3} \tan(\alpha)}{S_2 \overline{\omega^2}}. \quad (4.19)$$

where $\overline{\omega^3}$ is the mean cube of angular velocity.

Errors in P_{aero} due to errors α for the horizontal stroke plane model

The chief source of error in the model for hovering with a horizontal stroke plane is likely to be due to inaccuracy in α . This may be because of difficulties in determining which of the observed values of α is appropriate due to variation within a wingstroke or down a twisted wing, or may be due to errors in the measurement itself (see Willmott and Ellington, 1997a). If an angle of attack a is used in the model, which differs from the ‘true’ geometric angle of attack α , then the calculated and ‘true’ horizontal force coefficients, and the associated aerodynamic powers, are proportional to the tangent of these angles. So, the magnitude of the error in estimating P_{aero} due to an inappropriate selection of α can be given:

$$\text{Error (\%)} = 100 \left| \frac{\tan(\alpha) - \tan(a)}{\tan(\alpha)} \right|. \quad (4.20)$$

Some results for this expression are shown in Fig. 4.1. The plot for $\alpha = 35^\circ$ is of particular interest as it is appropriate for a wide range of insects (Ellington, 1984c). If estimates of α are accurate to within 5° , then P_{aero} should be within 22% of the true value.

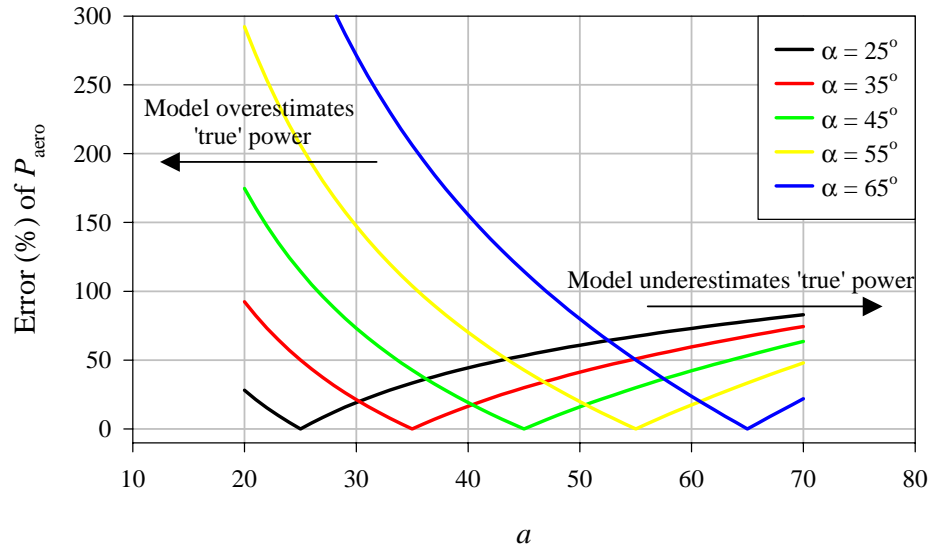


Fig. 4.1. The error in P_{aero} estimates for 'normal hovering' due to the use of incorrect geometric angles of attack.

Hovering with an inclined stroke plane: birds and bats

The hovering and very slow flight of most birds and bats relies predominantly on weight support during the downstroke only. In such flight, the component of F_v (which acts perpendicular to the stroke plane β) opposing gravity equals $F_v \cos(\beta)$. The net component of F_h from both wings acting against gravity is proportional to $\sin(\beta)$, and is also related to the angle ϕ within the stroke plane. At the beginning of a downstroke, most of F_h acts laterally and there is little contribution to weight support. Half-way through the downstroke, with ϕ around 0° , the components $F_h \sin(\beta)$ acting from each wing oppose gravity.

If weight is supported on the downstroke only, with an inclined stroke plane β , downstroke duration T_d , and total time T for a complete wingbeat cycle,

$$mg = F_v \frac{T_d}{T} \cos(\beta) + \sin(\beta) \frac{\int_{t=0}^{t=T_d} F_h \cos(\phi) dt}{T}. \quad (4.21)$$

Combining this with equation (4.11), and the normal force relationship (4.16), where α is the geometric angle of attack with respect to the stroke plane, a mean value for C_v can be found:

$$C_v = \frac{2mg}{S_2} \left[\frac{T}{T_d \cos(\beta) \overline{\omega^2} + \tan(\alpha) \sin(\beta) \int_{t=0}^{t=T_d} \omega^2 \cos(\phi) dt} \right]. \quad (4.22)$$

The mean value of C_h can then be calculated from equation (4.16) as before. If the wings only produce aerodynamic forces during the downstroke, then aerodynamic power is only required during the downstroke. The mean aerodynamic power P_{aero} for a complete wingbeat cycle is given by:

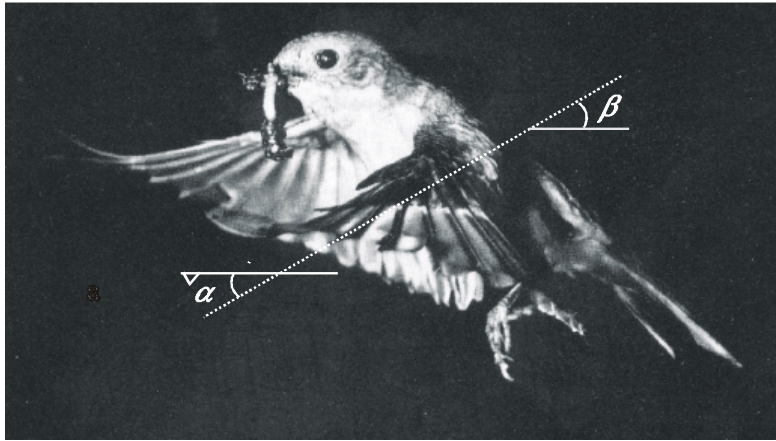
$$P_{\text{aero}} = \frac{\rho}{2} S_3 \overline{\omega^3} C_h \frac{T_d}{T}. \quad (4.23)$$

A suitable value of α has rarely been observed for animals that hover using an inclined stroke plane. However, if it is true that very little force is produced on the upstroke, and the normal force relationship holds, then the orientation of the wing chord should be approximately horizontal (see Fig. 4.2). In this case

$$\alpha = \beta, \tag{4.24}$$

and β is a very easily, and more frequently, observed parameter.

A



B



Fig. 4.2. (A, B). Wing position in mid to late downstroke of a hovering pied flycatcher after Norberg, U. (1975). In (A) the dotted line represents the path of the wing tip, following an 'inclined stroke plane' at an angle β to the horizontal. A representative wing chord is drawn on the dotted line, at an angle α to the stroke plane. If $\alpha = \beta$ then the wing chord is horizontal. The wing tips (B) are composed of spread primaries, which are sharp, thin, and are orientated horizontally.

Parameters

Hovering with a horizontal stroke plane

Table 4.1 shows mean parameters for a range of animals that hover with a ‘horizontal’ stroke plane. A varied number N of individuals is described for each species in the studies from which the data are taken. Of the parameters shown, α is the most uncertain. The value assumed for the bumblebee, craneflies, ladybird and euglossine bees is that described as typical by Ellington (1984c). The value for hummingbirds is the effective angle of incidence derived by Weis-Fogh (1972) from Hertel’s (1966) data, and was assumed to be close to the geometric angle of attack α . Willmott and Ellington (1997b) present α both throughout the wingstroke and along the length of the wing for the hawkmoth *Manduca sexta*. The value of 35° chosen here favours the wing tip, and the middle of each half-stroke, as this is where the force production is greatest. This value also agrees independently with Ellington’s typical value of 35° .

The remaining morphological and kinematic parameters are less uncertain. Wing moments are given in their non-dimensional forms (Ellington, 1984b). The non-dimensional second and third moments of wing area are given by

$$\hat{r}_2(S) = \sqrt{\frac{S_2}{S R^2}}, \quad (4.25)$$

and

$$\hat{r}_3(S) = \left(\frac{S_3}{S R^3} \right)^{\frac{1}{3}} \quad (4.26)$$

respectively, where S is the wing area for both wings. The non-dimensional second moment of mass is given by

$$\hat{r}_2(m) = \sqrt{\frac{m_2}{m_w R^2}}, \quad (4.27)$$

where m_w is the mass of both wings.

The kinematics were assumed to be sinusoidal. This appears reasonably accurate for the majority of insects which hover using horizontal stroke planes

Table 4.1a. Mean morphology and kinematics of animals which hover with a horizontal stroke plane: various insects

	Bumblebee	Cranefly	Cranefly	Hawkmoth	Ladybird	Fruit fly
	<i>Bombus terrestris</i>	<i>Tipula obselata</i>	<i>Tipula paludosa</i>	<i>Manduca sexta</i>	<i>Coccinella 7-punctata</i>	<i>Drosophila melanogaster</i>
Main references	Cooper, 1993	Ellington, 1984c	Ellington, 1984c	Willmott, 1995	Ellington, 1984c	Lehmann and Dickinson, 1997
N	29	1	1	3	1	1
Morphology						
m (mg)	252.5	11.4	49.8	1740.7	34.4	1.1
R (mm)	12.0	12.7	17.4	50.8	11.2	2.5
AR	6.76	10.93	11.25	5.48	7.07	6.18
m_w (as % m)	0.45	4.29	2.37	5.33	2.87	0.60
m_m (as % m)	26.8					30.0
$\hat{r}_2(S)$	0.558	0.602	0.604	0.516	0.528	0.632(a)
$\hat{r}_3(S)$	0.600	0.638	0.640	0.555	0.574	0.623
$\hat{r}_2(m)$	0.44 (b)	0.50	0.50	0.38	0.40	0.59
Kinematics						
n (Hz)	176.9	45.5	58.0	25.9	53.9	209.0
Φ (deg)	122	123	120	116	177	162
α (deg)	35 (b)	35 (b)	35 (b)	35	35 (b)	55 (a)

Secondary references: (a) Vogel (1967b); (b) Ellington (1984c). Symbols are defined in the text and described in the Symbols list.

Table 4.1b. Morphology and kinematics of animals which hover with a horizontal stroke plane: euglossine bees

		Casey and Ellington, 1989							
		<i>Euglossa crassipunctata</i>	<i>Euglossa bursigera</i>	<i>Euglossa cyanaspis</i>	<i>Euglossa imperialis</i>	<i>Eulaema nigrita</i>	<i>Eulaema cingulata</i>	<i>Exarete frontalis</i>	<i>Eulaema meriana</i>
		1	1	1	12	2	1	1	2
Main references									
N									
Morphology									
m (mg)		68.0	89.0	103.0	167.7	446.0	499.0	626.0	883.0
R (mm)		8.1	8.6	8.7	11.1	15.5	16.9	22.8	21.4
AR		6.70	6.52	6.84	6.84	6.37	6.51	6.34	5.97
m_w (as % m)		0.52	0.44	0.45	0.48	0.52	0.62	1.11	0.68
m_m (as % m)		29.4	26.4	32.0	27.6	28.5	29.5	29.0	27.0
$\hat{r}_2(S)$		0.551	0.544	0.539	0.543	0.529	0.540	0.532	0.526
$\hat{r}_3(S)$		0.595	0.587	0.582	0.587	0.574	0.583	0.577	0.572
$\hat{r}_2(m)$		0.45	0.41	0.41	0.40	0.40	0.37	0.39	0.38
Kinematics									
n (Hz)		177.0	196.5	209.0	181.6	155.1	138.0	88.7	108.8
Φ (deg)		145	134	140	127	118	120	118	132
α (deg)		35 (b)	35 (b)	35 (b)	35 (b)	35 (b)	35 (b)	35 (b)	35 (b)

Secondary reference: (b) Ellington (1984c). Symbols are defined in the text and described in the Symbols list.

Table 4.1c. *Morphology and kinematics of animals which hover with a horizontal stroke plane: hummingbirds*

	Broad-tailed hummingbird <i>Selasphorus platycercus</i>	Rufus hummingbird <i>Selasphorus rufus</i>
Main references	Wells, 1993	
N	8	3
Morphology		
m (mg)	3967.5	4280.0
R (mm)	55.1	49.0
$A R$	7.79	8.01
m_w (as % m)	5.40	3.64
m_m (as % m)	24.4	23.4
\hat{r}_2 (S)	0.522	0.520
\hat{r}_3 (S)	0.571	0.570
\hat{r}_2 (m)	0.26	0.25
Kinematics		
n (Hz)	38.4	48.1
Φ (deg)	143	154
α (deg)	23 (c)	23 (c)

Secondary reference: (c) Weis-Fogh (1972). Symbols are defined in the text and described in the Symbols list.

(Ellington, 1984c), and small deviations from sinusoidal wing motion have little effect on the power calculations. Sinusoidal kinematics are described by

$$\phi = \bar{\phi} + \frac{\Phi}{2} \cos(2\pi nt), \quad (4.28)$$

where $\bar{\phi}$ is the mean stroke angle. The magnitude of the angular velocity at any instant is

$$\omega = \pi n \Phi \sin(2\pi nt). \quad (4.29)$$

So, the average values of ω^2 and ω^3 are given by

$$\overline{\omega^2} = \frac{\pi^2 n^2 \Phi^2}{2}, \quad (4.30)$$

and

$$\overline{\omega^3} = \frac{4 \pi^2 n^3 \Phi^3}{3} \quad (4.31)$$

respectively. This allows the expression for aerodynamic power, equation (4.19), to be simplified to

$$P_{\text{aero}} = \frac{8}{3} m g n \Phi R \frac{\hat{r}_3^3(S)}{\hat{r}_2^2(S)} \tan(\alpha). \quad (4.32)$$

Flight with an inclined stroke plane

Table 4.2 shows appropriate morphological and kinematic parameters for hovering flight for one bird and two bats. Data for the slow ascending flight of a greater horseshoe bat (Aldridge, 1991) is also included, as the ascent approximates hovering; the upward velocity was only 21% of the mean downstroke wing-tip velocity, and the parasite drag implicit in Aldridge's calculations accounts for a force less than 1.3% of weight, and so was discounted.

Wing images from the appropriate publications (Norberg, U, 1975, 1976; Norberg, U *et al.* 1993) were scanned, from which the wing moments S_2 and S_3 were derived (equations (4.12) and (4.15)). Aspect ratio and wing area were also measured from the scanned images, and these agreed well with those published. Wing images and moments for the greater horseshoe bat were not available, so the values determined for the long-eared bat were used. The wing area calculated from the

Table 4.2 Morphology and kinematics of animals which hover with an inclined stroke-plane

	Pied flycatcher <i>Ficedula hypoleuca</i>	Long-eared bat <i>Plecotus auritus</i>	Long-tongued bat <i>Glossophaga soricina</i>	Greater horseshoe bat <i>Rhinolophus ferrumequinum</i>
Main references	Norberg (1973)	Norberg (1976)	Norberg <i>et al.</i> (1993)	Aldridge (1991)
Morphology				
m (g)	12.00	9.00	10.50	22.2
R (m)	0.100	0.124	0.117	0.180
AR	4.47	5.70	6.01	5.80
m_m (as % m)	15.6(a)	13.7(b)	13.7(b)	13.7(b)
$\hat{r}_2(S)$	0.510	0.595	0.570	0.595(c)
$\hat{r}_3(S)$	0.562	0.533	0.537	0.533(c)
Kinematics				
n (Hz)	14.3	11.35	10.27	10.64
τ	0.42	0.52	0.48	0.45
Φ (deg)	102	120	120	104.4
β (deg)	30	30	30	45.81

Secondary references: (a) Magnan (1922) in Greenewalt (1962); (b) Betz (1958) in Norberg (1976), which is taken to be reasonable for all bats. Moments for *Rhinolophus* (c) are assumed similar to those for *Plecotus*. This is supported by a calculation of wing area within 0.5% of that described by Aldridge. Symbols are defined in the text and described in the Symbols list.

values of S_2 (following Ellington, 1984b) taken from the long-eared bat, but R and aspect ratio from the greater horseshoe bat, was within 0.5% of that described by Aldridge.

It was assumed that no forces are produced during the upstroke, and equation (4.24) was used to find appropriate values of α .

In each study, the kinematics of the downstroke are described as being very close to sinusoidal. However, asymmetry between the duration of upstroke and downstroke is sometimes significant and has a considerable bearing on power estimates. For animals hovering with an inclined stroke plane the proportion of the complete wingbeat cycle spent on the downstroke is given by

$$\tau = \frac{T_d}{T}, \quad (4.33)$$

and the expression

$$\phi = \bar{\phi} + \frac{\Phi}{2} \cos\left(\pi \frac{t}{T_d}\right) \quad (4.34)$$

was used for the downstroke kinematics. $\bar{\phi}$ was assumed to be negligible, and the kinematic components of equations (4.22) and (4.23) were calculated numerically for 20 time steps.

Results

Values for power P are given in two mass-specific forms to enable comparisons between species covering a considerable size range. The body-mass-specific form P^* is given by

$$P^* = \frac{P}{m}, \quad (4.35)$$

where m is the total body mass. This is relevant for discussions on aerodynamic performance; animals that are ‘efficient’ at hovering, allowing body weight to be supported with a low mechanical power, would have low values of P^* . The muscle-mass-specific power P^\dagger is given by

$$P^\dagger = \frac{P}{m_m}, \quad (4.36)$$

where m_m is flight muscle mass. This is of interest in terms of muscle performance.

Table 4.3 shows results for P_{aero} given by previous authors (which combines their values for induced and profile powers), along with new values for P_{ind} and P_{acc} calculated from equations (4.1) and (4.4) with a k_{ind} of 1.2 in order to keep results comparable. While the power components presented in the previous studies are based on the ‘traditional’ methods described in the introduction, and are close to the new values presented in Table 4.3, slight differences do exist.

Tables 4.4 and 4.5 display results from the present model for animals that hover with horizontal and inclined stroke planes, respectively. Table 4.5 includes induced powers derived from equation (4.1) for comparison. Horizontal and vertical force coefficients are also presented. These approximate to the conventional profile drag and lift coefficients $C_{D,\text{pro}}$ and C_L (which act parallel and perpendicular, respectively, to the relative air velocity) when the induced air velocities are low. All values of C_v in Table 4.4, and for two of the bats in Table 4.5, appear achievable for steady, revolving wings (see Chapters 2 and 3). However, values of C_v calculated for the pied flycatcher and long-eared bat are considerably above those that have been described previously, even for revolving wings.

Table 4.3 includes published muscle efficiencies η , (avoiding the inclusion of inertial powers to aid comparison) defined as

$$\eta = \frac{P_{\text{aero}}}{P_{\text{met}}}, \quad (4.37)$$

where P_{met} is the metabolic power, calculated from respiratory measurements. Table 4.4 shows new values for η based on P_{aero} derived from the current model, using the same metabolic results as before.

Table 4.3a. Previous results for P_{aero} and η estimates, with values for P_{ind} and P_{acc} calculated from Ellington's (1984f) methods for animals which hover with a horizontal stroke plane: various insects

Main references	Bumblebee <i>Bombus terrestris</i>	Cranefly <i>Tipula obselata</i>	Cranefly <i>Tipula paludosa</i>	Hawkmoth <i>Manduca sexta</i>	Ladybird <i>Coccinella 7-punctata</i>	Fruit fly <i>Drosophila melanogaster</i>
	Cooper, 1993	Ellington, 1984f	Ellington, 1984f	Willmott, 1995	Ellington, 1984f	Lehmann and Dickinson, 1997
Body mass specific P						
P^*_{aero} (W kg^{-1})	29.2	10.1	15.0	23.6	11.3	17.9
P^*_{ind} (W kg^{-1})	20.6	4.3	6.7	13.7	7.1	5.9
P^*_{acc} (W kg^{-1})	59.2	14.8	30.4	28.6	17.0	18.2
Muscle mass specific P						
$P^{\dagger}_{\text{aero}}$ (W kg^{-1})	105.2			122.1		59.8
P^{\dagger}_{ind} (W kg^{-1})	75.4			71.7		19.6
P^{\dagger}_{acc} (W kg^{-1})	213.0			146.6		60.8
Implications						
η (excluding P_{acc}) (%)	7.9					9.0
$P_{\text{ind}}/P_{\text{aero}}$ (%)	70.5	42.6	44.7	58.1	62.8	33.0
$P_{\text{acc}}/P_{\text{aero}}$ (%)	202.7	146.5	202.7	121.2	150.4	101.7

Symbols are defined in the text and described in the Symbols list.

Table 4.3b. Previous results for P_{aero} and η estimates, with values for P_{ind} and P_{acc} calculated from Ellington's (1984f) methods for animals which hover with a horizontal stroke plane: euglossine bees

	<i>Euglossa crassepunctata</i>	<i>Euglossa bursigera</i>	<i>Euglossa cyanaspis</i>	<i>Euglossa imperialis</i>	<i>Eulaema nigrita</i>	<i>Eulaema cingulata</i>	<i>Exarete frontalis</i>	<i>Eulaema meriana</i>
Casey and Ellington, 1989								
Main references								
Body mass specific P								
P^*_{aero} (W kg^{-1})	24.1	26.2	27.9	27.7	29.7	28.9	24.1	28.9
P^*_{ind} (W kg^{-1})	15.2	17.1	17.7	18.7	22.6	21.7	18.2	21.8
P^*_{acc} (W kg^{-1})	47.6	45.0	61.8	52.8	61.2	55.4	51.6	60.0
Muscle mass specific P								
$P^{\dagger}_{\text{aero}}$ (W kg^{-1})	81.9	99.1	87.3	100.6	104.3	97.8	83.2	107.6
P^{\dagger}_{ind} (W kg^{-1})	51.8	64.6	55.4	68.1	79.4	73.7	62.7	81.4
P^{\dagger}_{acc} (W kg^{-1})	162.0	170.4	191.0	192.6	215.8	188.0	178.0	224.2
Implications								
η (excluding P_{acc})	3.9	4.4	4.7	6.0	9.4	10.0	11.1	13.0
$P_{\text{ind}}/P_{\text{aero}}$ (%)	63.2	65.2	63.5	67.7	76.1	75.4	75.4	75.7
$P_{\text{acc}}/P_{\text{aero}}$ (%)	197.8	171.9	218.8	191.5	206.9	192.2	213.9	208.4

Symbols are defined in the text and described in the Symbols list.

Table 4.3c. Previous results for P_{aero} and η estimates, with values for P_{ind} and P_{acc} calculated from Ellington's (1984f) methods for animals which hover with a horizontal stroke plane: hummingbirds

	Broad-tailed hummingbird <i>Selasphorus platycercus</i>	ufus hummingbird <i>Selasphorus rufus</i>
Main references		
Wells, 1993		
Body mass specific P		
P^*_{aero} (W kg^{-1})	24.4	27.6
P^*_{ind} (W kg^{-1})	19.6	22.2
P^*_{acc} (W kg^{-1})	78.4	82.6
Muscle mass specific P		
$P^{\dagger}_{\text{aero}}$ (W kg^{-1})	102.1	118.9
P^{\dagger}_{ind} (W kg^{-1})	81.0	94.8
P^{\dagger}_{acc} (W kg^{-1})	328.0	355.6
Implications		
η (excluding P_{acc})	8.3	9.4
$P_{\text{ind}}/P_{\text{aero}}$ (%)	80.3	80.4
$P_{\text{acc}}/P_{\text{aero}}$ (%)	321.3	299.3

Symbols are defined in the text and described in the Symbols list.

Table 4.4a. Current model results for animals which hover with a horizontal stroke plane: various insects

	Bumblebee <i>Bombus terrestris</i>	Cranefly <i>Tipula obselata</i>	Cranefly <i>Tipula paludosa</i>	Hawkmoth <i>Manduca sexta</i>	Ladybird <i>Coccinella 7-punctata</i>	Fruit fly <i>Drosophila melanogaster</i>
Force coefficients						
C_h	0.98	0.80	0.66	1.13	1.16	1.48
C_v	1.40	1.15	0.94	1.62	1.66	1.03
Body mass specific P						
P^*_{aero} (W kg^{-1})	57.3	16.3	27.8	31.7	23.2	33.0
Muscle mass specific P						
$P^{\dagger}_{\text{aero}}$ (W kg^{-1})	209.0			167.0		110.0
Implications						
η (excluding P_{acc})	15.8					16.6
$P_{\text{ind}}/P_{\text{aero}}$ (%)	37.0	26.5	24.0	25.2	24.2	17.8
$P_{\text{acc}}/P_{\text{aero}}$ (%)	107.6	61.2	73.2	67.2	51.2	55.4

Symbols are defined in the text and described in the Symbols list.

Table 4.4b. Current model results for animals which hover with a horizontal stroke plane: euglossine bees

	<i>Euglossa crassipunctata</i>	<i>Euglossa bursigera</i>	<i>Euglossa cyanaspis</i>	<i>Euglossa imperialis</i>	<i>Eulaema nigrita</i>	<i>Eulaema cingulata</i>	<i>Exarete frontalis</i>	<i>Eulaema meriana</i>
Force coefficients								
C_h	1.00	0.98	0.94	0.94	1.00	0.95	0.90	0.84
C_v	1.43	1.40	1.34	1.34	1.44	1.36	1.29	1.20
Body mass specific P								
P^*_{aero} (W kg ⁻¹)	46.2	49.5	55.3	55.6	61.4	60.7	51.8	66.3
Muscle mass specific P								
P^{\dagger}_{aero} (W kg ⁻¹)	157.2	187.6	172.9	201.8	215.7	205.9	178.7	247.7
Implications								
η (excluding P_{acc})	7.8	8.3	12.1	12.4	17.5	19.2	21.2	34.0
P_{ind}/P_{aero} (%)	33	35	32	34	37	36	35	33
P_{acc}/P_{aero} (%)	103.2	90.8	111.6	95.2	99.4	91.4	99.6	90.6

Symbols are defined in the text and described in the Symbols list.

Table 4.4c. Current model results for animals which hover with a horizontal stroke plane: hummingbirds

	Broad-tailed hummingbird <i>Selasphorus platycercus</i>	ufus hummingbird <i>Selasphorus rufus</i>
Force coefficients		
C_h	0.47	0.48
C_v	1.11	1.12
Body mass specific P		
P^*_{aero} (W kg^{-1})	40.1	47.9
Muscle mass specific P		
$P^{\dagger}_{\text{aero}}$ (W kg^{-1})	166.2	205.8
Implications		
η (excluding P_{acc})	13.8	16.6
$P_{\text{ind}}/P_{\text{aero}}$ (%)	49.2	46.3
$P_{\text{acc}}/P_{\text{aero}}$ (%)	194.4	172.2

Symbols are defined in the text and described in the Symbols list.

Table 4.5. Current model results for animals which hover with an inclined stroke plane

	Pied flycatcher <i>Ficedula hypoleuca</i>	Long-eared bat <i>Plecotus auritus</i>	Long-tongued bat <i>Glossophaga soricina</i>	Greater horseshoe bat <i>Rhinolophus ferrumequinum</i>
Mean force coefficients				
C_h	2.89	1.90	1.05	1.28
C_v	5.01	3.30	1.82	1.25
Body mass specific powers				
P^*_{aero} (W kg ⁻¹)	32.17	29.90	29.72	38.57
P^*_{ind} (W kg ⁻¹)	21.00	13.52	14.48	17.48
Muscle mass specific powers				
P^\dagger_{aero} (W kg ⁻¹)	206.2	218.2	217.0	281.5
P^\dagger_{ind} (W kg ⁻¹)	123.5	98.7	93.8	106.0

Symbols are defined in the text and described in the Symbols list.

Discussion

The most striking outcome of the model presented here is the increase in estimates for P_{aero} , typically around 90%. This should not be viewed as peculiar to the current model; similar increases are achieved if the high values of $C_{D,\text{pro}}$ presented in Chapters 2 and 3 are used in conventional models (Ellington, in prep.). Chapters 2 and 3 show that previous values for $C_{D,\text{pro}}$ for both insects (Ellington, 1984f) and vertebrates (Rayner, 1979c; Pennycuick *et al.* 1992) considerably underestimate drag for wings producing high forces during revolution. The high profile drags are related to the loss of leading-edge suction associated with the production of leading-edge vortices (Polhamus, 1971), which might be expected for revolving wings operating at high incidences and producing high vertical force coefficients (Tables 4.4 and 4.5). It should be noted, however, that these high profile drags may not be applicable to fast forward flight. The aerodynamics of fast forward, and certainly gliding, flight, are likely to be dominated by attached flow around cambered aerofoils operating at low incidences. In this situation, leading-edge suction is maintained, the net profile drags are likely to be very low, and the normal force relationship is invalid.

Hovering with a horizontal stroke plane

A key implication of the new, high, estimate of P_{aero} is that it approaches or exceeds P_{acc} , and so energy put into accelerating the wings can be returned directly into aerodynamic force production during the deceleration phase of each half-stroke. This means that P_{acc} need not be included in power calculations, and the need for elastic storage appears minimal, probably within the capabilities of the flight muscle itself (Alexander and Bennet-Clark, 1977). This is not to say that P_{acc} has no bearing on the determination of wing architecture and adaptive flight kinematics (discussed in Chapter 5), or on the contractile characteristics of the flight muscle.

Previously, P_{ind} was considered the dominating aerodynamic power requirement for the majority of hovering insects, with the notable exception of *Drosophila*. Results from the current model suggest that the relative importance of induced power is considerably lower than had been proposed. This means that hovering animals are far from optimal propellers: much of the air is being accelerated

in directions other than straight down. The conclusion reached by Lehmann and Dickinson (1997), that ‘it is the cost of overcoming drag, not the production of lift, that is the primary requirement for flight...’ appears applicable to a far broader range of animals than just *Drosophila*. However, the mechanism causing this drag is quite different from that previously supposed: the ‘drag’ is caused by the pressure force acting ‘normal’ to the wing surface, and not due to viscous effects at low Reynolds numbers.

The calculated muscle-mass-specific powers of around 200 W kg^{-1} are high, but recent work (Josephson *et al.* 2000) suggests that this may be achievable, at least in asynchronous muscle.

Unsteady mechanisms: energetic savings with ‘wake capture’

While steady propeller coefficients described in chapters 2 and 3 appear sufficient to account for the values of C_v calculated for the majority of animals in this study, the quasi-steady assumption should still be viewed critically (see Ellington, 1984a). Although unsteady mechanisms may no longer be required to account for weight support, implications to power estimates may be considerable. Energetic benefit may be achieved if unsteady induced flows could weight force production towards the slow phases of wing motion. The wake created behind a wing during a down- (or up-) stroke has some component of flow following the wing, due to the high profile drag, which may then increase the relative air velocity over the wing as it flaps slowly during and just after pronation (or supination). This would have the effect of increasing force production while the wing is moving slowly with respect to the body. In this way, unsteady mechanisms may improve aerodynamic efficiency by increasing weight support for a negligible energetic cost, even without a change in the ratio of C_v to C_h . This is one way of describing the potential energetic benefits of ‘wake capture’ mechanisms (Dickinson *et al.* 1999): some of the energy ‘wasted’ by accelerating air in directions other than downwards can be recovered.

Slow flight with an inclined stroke plane

The current model provides a reasonable estimate of the power requirements for the published hovering sequences for two bats and one bird. The ‘normal force relationship’ appears appropriate given that the large force coefficients required (Table 4.5) are achieved by sharp, thin wings (particularly at the wing tips of both birds and bats) which operate at high angles of incidence; flow separation at the leading-edge, along with the associated loss of leading-edge suction, is likely. Supporting this, the polar diagram for the revolving quail wing (Fig. 3.7) shows that high vertical force coefficients are associated with high horizontal force coefficients, even for a cambered, feathered wing.

The assumption that no forces are produced during the upstroke is clearly a simplification. Norberg, U’s (1975) flycatcher flexed its wings (Norberg, U, 1975, 1990) and appeared to allow air through the spread and angled primaries during the upstroke. Fig. 4.2 (after Norberg, U, 1975) shows a hovering pied flycatcher in mid to late downstroke. While the wing, when considered as a whole, is deeply cambered and is angled with respect to the ground, the tips of the outer four primaries are parallel to the ground, agreeing with the assumption that $\alpha = \beta$. However, bats flex their wings only slightly during the upstroke (30% in Norberg, U *et al.* 1993), and some contribution to the force balance during the upstroke is likely. As a preliminary analysis, though, it is reasonable to consider the forces during the upstroke negligible, as the angle each wing element makes with the incident air appears small (even the sign of the angle is not clear, (Norberg, U, 1976)) during the upstroke.

The results of the current model for hovering or slow ascent with an inclined stroke plane show that the total aerodynamic power is 1.5 to 2.2 times that calculated for induced power. While a variety of corrections can be made to take into account the periodicity of force production in hovering with an inclined stroke plane (Rayner, 1979a,c; Ellington, 1984d-f), the empirical measurements of Norberg, U *et al.* (1993) support the calculated P_{ind} , at least for *Glossophaga soricina*.

Calculation of inertial powers for vertebrate wings (excluding the hummingbirds) is more complex than for insects, as the second moments of mass m_2 change with flexing of the wings. While estimates of inertial power in slow-flying bats vary radically (compare Aldridge, 1991 with Norberg, U *et al.* 1993), in all cases where they are considered they are lower than the new aerodynamic power estimates.

The muscle-mass-specific aerodynamic powers for the pied flycatcher and bats, approximately 200 W kg^{-1} , closely match the values derived for ‘normal’ hoverers. However, the power output required for hovering birds (other than hummingbirds) and bats is only achieved anaerobically, probably reflecting differences in muscle composition. The power requirements in the case of the ascending bat, of 281.5 W kg^{-1} incorporates ‘climbing power’ (the power required to lift the body weight against gravity, which would account for a P^\dagger of 97.5 W kg^{-1}). Overall, the power is well within the latest estimates for climbing flight in vertebrates (Askew *et al.* submitted).

The body-mass-specific powers highlight the implications of differing proportions of muscle mass. While hummingbirds carry an average muscle-mass approximating 24% of body-mass, and have an average P^*_{aero} of 43 W kg^{-1} , the other hovering vertebrates have relatively smaller muscle-masses (taken to be 13.7% or 15.6% of body mass for the pied flycatcher and bats respectively), and lower body-mass-specific powers, averaging 31 W kg^{-1} . These results suggest that flycatchers and bats hover with lower energetic costs than hummingbirds. If this is so, presumably the benefits of hummingbird-like flight are associated with aspects of speed, control and manoeuvrability rather than the pure minimisation of the energetic costs of hovering.

Unsteady mechanisms

The potential for wake-capture mechanisms to improve aerodynamic efficiency is likely to be limited for animals hovering with an inclined stroke plane where force production during the upstroke is small. The creation of a wake following the wing during the upstroke would necessarily be associated with a component of force acting with gravity, and would be quite undesirable. Other unsteady mechanisms, such as the ‘fling’, ‘peel’, or ‘flex’ (see Ellington, 1995, for a review of such phenomena), presumably do act in certain cases; the force coefficients for the hovering flycatcher (Norberg, U, 1975) and long-eared bat (Norberg, U, 1976) are considerably higher than can be accounted for with steady aerodynamics, even including the effects of revolution. Whatever aerodynamic mechanisms do act, though, the forces on the wings are likely to be dominated by pressure forces and be associated with separation from the leading-edge of the thin wing tips, thus

maintaining the $C_h = C_v \tan(\alpha)$ relationship. Given the fact that, in order to allow the high forces to oppose weight effectively, these forces have to act when the wings are around the middle of the downstroke, the high forces exist when the wings are moving fastest. Without an increase in the $C_v:C_h$ ratio, or a weighting of force production towards the periods when the wings are flapping slowly, little energetic savings due to unsteady mechanisms are possible.

Conclusion

A causal link between vertical and horizontal aerodynamic forces identified in Chapters 2 and 3, the ‘normal force relationship’, has been used in the development of a novel method for estimating the power requirements of hovering animal flight. New aerodynamic power estimates are considerably higher than those previously calculated. The potential implications of unsteady mechanisms on power estimates are discussed. Further study of the temporal and spatial characteristics of the local flow field is vital, both because of its significance to conventional analyses, and its potential for reducing the power estimates presented here through some form of ‘wake capture’.

Chapter 5: General discussion

'Propeller' force coefficients and the future of propeller-based experiments

Smoke visualisation and force measurements on revolving propeller wings (Chapters 2 and 3) suggest that the leading-edge vortex found over flapping hawkmoth wings (Ellington *et al.* 1996) may be a robust, steady phenomenon, and high force coefficients can be produced by a diverse range of revolving animal wings. Unsteady mechanisms will need to be considered in a 'general theory of insect flight' (Dickinson *et al.* 1999) because of their importance in manoeuvrability, control and, to a varying extent, lift production. However, coefficients derived from propeller experiments go much of the way towards accounting for the vertical force balance in many cases, and currently provide the most justifiable means of estimating the power requirements for hovering.

Potential future directions for propeller-based animal flight research include wind-tunnel experiments. These may provide the basics for understanding the transition between hovering flight, where aerodynamics are dominated by 'revolving', propeller-like flow conditions, to fast forward flight, where translational flow increases in importance. Also, the testing of further real and model wings may be productive; the aerodynamics and passive mechanics of bird wings set in appropriate configurations could provide insights into the functions of the alula and spread primaries, previously only considered within the context of translational flow.

Power calculations

A new method for determining power requirements for hovering flight, given relatively easily observed kinematics and morphology, has been developed in Chapter 4. Whether this approach, or previously described techniques, is adopted in the future, researchers should take note of the implications of revolution on profile drag coefficients. Where sufficient kinematics are observed, the expression

$$C_{D,pro} = C_L \tan(\alpha_r) \quad (5.1)$$

should supersede either the relationship described by Ellington (1984f), or the profile drag coefficients for vertebrate wings derived from flow tunnel experiments (Rayner, 1979c; Pennycuik *et al.* 1992; Drovetsky, 1996), for analyses of slow or hovering flight.

Force measurements on flapping models, such as those being developed by Dickinson *et al.* (1999) are required if account is to be taken of unsteady aerodynamics on power requirements for flapping. Quantitative measurements of the flow-field near flapping animal (e.g. Norberg, U *et al.* 1993) or model (e.g. Müller *et al.* in prep.) wings may also be productive lines of research, allowing some inferences to be drawn about power requirements. However, while these methods may allow the mechanisms of force production to be studied, any power calculations derived from them are indirect. Tying direct force measurements with quantitative flow visualisation, as is starting to be achieved for *Drosophila* (Dickinson *et al.* 1999) allows both the aerodynamic mechanisms and the energetic consequences of flapping aerodynamics to be assessed.

The power requirements from animal muscle calculated in this study is high; a muscle-mass-specific power of 200 W/kg appears to be a general value for hovering animals ranging from bumblebee to small birds and bats. While this value is clearly an approximation, it is supported by calculations based on conventional approaches using the new $C_{D,pro}$ relationship described in Chapters 2 and 3 (Ellington, in prep.). 200 W/kg is relatively high, and even higher values would be required for rapid ascending or loaded flight. *In vitro* (Gilmour and Ellington, 1993) and *in situ* (Josephson, 1997a,b; Josephson and Ellington, 1997) measurements for bumblebee muscles using the work-loop technique achieve maximum muscle-mass-specific powers of around 100 W/kg. Josephson (1997b) argues that these values are likely to be minimum estimates for maximum power; experimental preparations are far more likely to reduce than enhance muscle performance. Recent work on beetle muscle (Josephson *et al.* 2000) has achieved powers of 200 W/kg. In future, direct force measurements on the wings or wing bases of relatively intact insects (avoiding all problems due to disrupting the tracheal system and operating the muscles under inappropriate conditions) could provide an important link between power predictions from muscle physiology and aerodynamics.

Animal hovering is inefficient

Power calculations based on force coefficients derived in Chapters 2 and 3, whether using conventional approaches or the ‘normal force relationship’ (Chapter 4), result in a remarkable finding: animals hover inefficiently. A large proportion of the power requirements of flight cannot be attributed to accelerating air directly downwards; in conventional terms, profile power is significant compared with induced power. The wings of hovering animals operate at relatively high incidences, typically 35° for insects (Ellington, 1984c), which is much higher than conventional rotors operate at for reasonable lift:drag ratios. This use of high angles of attack, and the apparent inefficiency of animal hovering, invites some attempt at an adaptive explanation.

Limitations to frequency range

Hovering is rarely the sole use of flight; muscles and wings used for hovering, in most cases, must also be able to allow the animal to escape, hunt, migrate, pursue mates etc. So, in most cases, evolution towards an optimal hovering form may well be compromised by other biological requirements.

A single muscle type operates optimally over a limited range of velocities (directly related to wingbeat frequencies). Given the selective pressure to minimise weight for flying animals, the optimal range of wingbeat frequencies may be limited due to a limited range of muscle types; the same muscles power hovering as power forward flight. Results from *in vitro* ‘work loop’ experiments on bumblebee (Josephson, 1997a) and beetle (Josephson *et al.* 2000) muscle fibres show power outputs to be strongly frequency dependent. In both cases, a half-optimal frequency results in an approximately half-maximal power. In addition to this, insects may gain energetic benefits from acting as mechanical resonators (Greenewalt, 1960), which could also limit the range of frequencies useable by an individual insect. *If* selective pressures on insects act to produce an optimal wingbeat frequency for forward flight, then the insects might show sub-optimal traits for hovering. A low wingbeat frequency may be sufficient, and very efficient, for fast forward flight, but would result in a requirement for surprisingly high angles of incidence for hovering, if the same, low, frequency (and so high lift coefficient) was used. This argument appears

quite reasonable, especially for ‘opportunist’ hoverers, and is supported by the increase in lift coefficient with decreasing flight speed observed for bumblebee (Dudley and Ellington, 1990b) and hawkmoths (Willmott and Ellington, 1997b). However, it would predict that insects which effectively continuously hover when flying should use much lower angles of incidence. Ellington (1984c) describes crane fly flight as so slow in relation to the wing speed as to result, in effect, in hovering flight under all flying conditions. Even so, crane flies use angles of attack between 25° and 45°; well above that which should result in good lift:drag ratios.

Significance of inertial power

A key difference between flapping and steady propeller-like revolution is the relevance of inertial power. Propellers, and flapping wings in which elastic mechanisms are perfect, require no inertial power once the wings have started. It is suggested in Chapter 4 that aerodynamic powers are usually sufficiently high for inertial powers to be ignored; energy put into angular momentum of the wings can be used to overcome aerodynamic drag. If lower angles of incidence, more efficient in aerodynamic terms, were used, however, this may not be the case. In order to produce the same net lift force, wings at lower angles of incidence would have to flap faster: a drop in aerodynamic costs could well be outweighed by an increase in inertial power costs. This idea would predict that animals with better elastic mechanisms, or wings with lower second moments of mass, should operate at lower angles of incidence. At this stage, though, there is insufficient data on either of these factors for further comment.

Implications to Micro Air Vehicle design

The two immediate challenges for aerodynamicists involved in the development of ‘Micro Air Vehicles’ (MAVs) are to get sufficient lift with a given maximum power supply, and to develop efficient flight to extend operating time for a finite fuel supply. If hovering flight is an important component to MAV design, then the evidence presented here suggests that a simple rotor or helicopter will be more efficient than hovering with flapping wings. While unsteady mechanisms in flapping

flight may reduce power costs to some extent, it appears likely that animal-like hovering with flapping wings will always accelerate air in directions other than downward, and so be relatively inefficient. A further requirement for MAVs is, however, the ability to travel and manoeuvre effectively and efficiently. It is in this combination of hovering and fast, agile, forward flight where animals excel, but conventional technology runs into difficulties: consider, for instance, the inefficiency of the Harrier jet, and the safety record of the V-22 Osprey tilt-rotor 'convertiplane'.

References

- Aldridge, H.D.J.N. (1991). Vertical flight in the greater horseshoe bat *Rhinolophus ferrumequinum*. *J. Exp. Biol.* **157**, 183-204.
- Alexander, R.McN. and Bennet-Clark, H.C. (1977). Storage of elastic strain energy in muscle and other tissues. *Nature* **265**, 114-117.
- Ashill, P.R., Riddle, G.L. and Stanley, M.J. (1995). Separation control on highly-swept wings with fixed or variable camber. *Aeronautical J.* **October**, 317-327.
- Askew, G.N., Marsh, R.L. and Ellington, C.P. (submitted). The mechanical power output of the flight muscles of blue-breasted quail (*Coturnix chinensis*) during take-off.
- Azuma, A. and Yasuda, K. (1989). Flight performance of rotary seeds. *J. Theor. Biol.* **138**, 23-53.
- Barnard, R.H. and Philpott, D.R. (1995). *Aircraft flight*. Harlow: Longman.
- Birch, J.M. and Dickinson, M.H. (2001). Spanwise flow and the attachment of the leading-edge vortex on insect wings. *Nature* **412**, 729-733.
- Blake, R.W. (1978). The mechanics of labriform locomotion I. Labriform locomotion in the angelfish (*Pterophyllum eimekei*): an analysis of the power stroke. *J. Exp. Biol.* **82**, 255-271.
- Brackenbury, J.H. (1992). *Insects in flight*. London: Cassel.
- Brodsky, A.K. (1973). The swarming behaviour of mayflies (Ephemeroptera). *Ent. Rev.* **52**, 33-39.
- Casey, T.M. (1976). Flight energetics of sphinx moths: power input during hovering flight. *J. Exp. Biol.* **64**, 529-543.
- Casey, T.M. (1981). A comparison of mechanical and energetic estimates of flight cost for hovering sphinx moths. *J. Exp. Biol.* **91**, 117-129.
- Casey, T.M. and Ellington, C.P. (1989). Energetics of insect flight. In *Energy Transformations in Cells and Organisms* (ed. W. Wieser and E. Gnaiger), pp. 200-210. Stuttgart: Georg Thieme Verlag

- Cloupeau, M., Devillers, J.F. and Devezeaux, D. (1979). Direct measurements of instantaneous lift in desert locust; comparison with Jensen's experiments on detached wings. *J. Exp. Biol.* **80**, 1-15.
- Cooper, A.J. (1993). *Limitations of bumblebee flight performance*. PhD thesis, Cambridge University.
- Crimi, P. (1996). Finite element analysis of a samara-wing decelerator. *J. Aircraft* **33**, 793-802.
- Dalton, S. (1977). *The Miracle of Flight*. London: Sampson Low.
- Dickinson, M.H. (1994). The effects of wing rotation on unsteady aerodynamic performance at low Reynolds numbers. *J. Exp. Biol.* **192**, 179-206.
- Dickinson, M.H. and Götz, K.G. (1993). Unsteady aerodynamic performance of model wings at low Reynolds numbers. *J. Exp. Biol.* **174**, 45-64.
- Dickinson, M.H., Lehmann, F.-O. and Sane, S.P. (1999). Wing rotation and the aerodynamic basis of insect flight. *Science* **284**, 1954-1960.
- Dickinson, M.H. and Lighton, J.R.B. (1995). Muscle efficiency and elastic storage in the flight motor of *Drosophila*. *Science* **268**, 87-90.
- Drovetski, S.V. (1996). Influence of trailing-edge notch on flight performance of galliforms. *Auk* **113**, 802-810.
- Dudley, R. (1991). Biomechanics of flight in neotropical butterflies: aerodynamics and mechanical power requirements. *J. Exp. Biol.* **159**, 335-357.
- Dudley, R. (1995). Extraordinary flight performance of orchid bees (Apidae: Euglossini) hovering in heliox (80% He/20% O₂). *J. Exp. Biol.* **198**, 1065-1070.
- Dudley, R. (2000). *The biomechanics of insect flight*. Princeton: Princeton University Press.
- Dudley, R. and Chai, P. (1996). Animal flight mechanics in physically variable gas mixtures. *J. Exp. Biol.* **199**, 1881-1885.
- Dudley, R. and DeVries, P.J. (1990). Flight physiology of migrating *Urania fulgens* (Uraniidae) moths: kinematics and aerodynamics of natural free flight. *J. Comp. Physiol. A* **167**, 145-154.
- Dudley, R. and Ellington, C.P. (1990a). Mechanics of forward flight in bumblebees. I. Kinematics and morphology. *J. Exp. Biol.* **148**, 19-52.
- Dudley, R. and Ellington, C.P. (1990b). Mechanics of forward flight in bumblebees. II. Quasi-steady lift and power requirements. *J. Exp. Biol.* **148**, 53-88.

- Electro-Craft Corporation (1980). *DC motors speed controls servo systems*. Crewe: Electro-Craft.
- Ellington, C.P. (1984a). The aerodynamics of hovering insect flight. I. The quasi-steady analysis. *Phil. Trans. R. Soc. Lond. B* **305**, 1-15.
- Ellington, C.P. (1984b). The aerodynamics of hovering insect flight. II. Morphological parameters. *Phil. Trans. R. Soc. Lond. B* **305**, 17-40.
- Ellington, C.P. (1984c). The aerodynamics of hovering insect flight. III. Kinematics. *Phil. Trans. R. Soc. Lond. B* **305**, 41-78.
- Ellington, C.P. (1984d). The aerodynamics of hovering insect flight. IV. Aerodynamic mechanisms. *Phil. Trans. R. Soc. Lond. B* **305**, 79-113.
- Ellington, C.P. (1984e). The aerodynamics of hovering insect flight. V. A vortex theory. *Phil. Trans. R. Soc. Lond. B* **305**, 115-144.
- Ellington, C.P. (1984f). The aerodynamics of hovering insect flight. VI. Lift and power requirements. *Phil. Trans. R. Soc. Lond. B* **305**, 145-181.
- Ellington, C.P. (1991). Aerodynamics and the origin of insect flight. *Adv. Insect physiol.* **23**, 171-210.
- Ellington, C.P. (1995). Unsteady aerodynamics of insect flight. In *Biological Fluid Dynamics* (ed. C.P. Ellington and T.J. Pedley). *Symp. Soc. Exp. Biol.* **49**. Cambridge: Company of Biologists.
- Ellington, C.P. (1999). The novel aerodynamics of insect flight: Applications to micro-air vehicles. *J. Exp. Biol.* **202**, 3439-3448.
- Ellington, C.P. and Usherwood, J.R. (in press). Lift and drag characteristics of flapping wings.
- Ellington, C.P., Van den Berg, C., Willmott, A.P. and Thomas, A.L.R. (1996). Leading-edge vortices in insect flight. *Nature* **384**, 626-630.
- Ennos, A.R. (1988). The importance of torsion in the design of insect wings. *J. Exp. Biol.* **140**, 137-160.
- Ennos, A.R. (1989a). The kinematics and aerodynamics of the free flight of some Diptera. *J. Exp. Biol.* **142**, 49-85.
- Gilmour, K.M. and Ellington, C.P. (1993). Power output of glycerinated bumblebee flight muscle. *J. Exp. Biol.* **183**, 77-100.

- Graham, J.M.R. (1992). Wind tunnel measurements on a stalled horizontal axis wind turbine rotor. *IEA meeting, ECN Petten, NL*.
- Greek, D. (1999). Mini flyers follow the buzz. *Professional Engineering*. **12**, 26-27.
- Greenewalt, C.H. (1960). The wings of insects and birds as mechanical oscillators. *Proc. Am. Phil. Soc.* **104**, 605-611.b
- Hertel, H. (1966). *Structure, Form, Movement*. New York: Reinhold.
- Hoerner, S.F. (1958). *Fluid-dynamic Drag*. Bricktown, N.J.: S.F. Hoerner.
- Hopkins, H. (1986). Fastest blades in the world. *Flight International*. **27 December**. 24-27.
- Jensen, M. (1956). Biology and physics of locust flight. III. The aerodynamics of locust flight. *Phil. Trans. R. Soc. Lond. B* **239**, 511-552.
- Josephson, R.K. (1997a). Power output from a flight muscle of the bumblebee *Bombus terrestris*. 2. Characterization of the parameters affecting power output. *J. Exp. Biol.* **200**, 1227-1239.
- Josephson, R.K. (1997b). Power output from a flight muscle of the bumblebee *Bombus terrestris*. 3. Power during simulated flight. *J. Exp. Biol.* **200**, 1241-1246.
- Josephson, R.K. and Ellington, C.P. (1997). Power output from a flight muscle of the bumblebee *Bombus terrestris*. 1. Some features of the dorso-ventral flight muscle. *J. Exp. Biol.* **200**, 1215-1226.
- Josephson, R.K., Malamud, J.G. and Stokes, D.R. (2000). Power output by an asynchronous flight muscle from a beetle. *J. Exp. Biol.* **203**, 2667-2689.
- Lehmann, F.-O. and Dickinson, M.H. (1997). The changes in power requirements and muscle efficiency during elevated force production in the fruit fly *Drosophila melanogaster*. *J. Exp. Biol.* **200**, 1133-1143.
- Lighthill, M.J. (1973). On the Weis-Fogh mechanism of lift generation. *J. Fluid Mech.* **60**, 1-17.
- Liu, H., Ellington, C.P., Kewachi, K., Van den Berg, C. and Willmott, A.P. (1998). A computational fluid dynamic study of hawkmoth hovering. *J. Exp. Biol.* **201**, 461-477.
- Lowson, M.V. and Riley, A.J. (1995). Vortex breakdown control by delta wing geometry. *J. Aircraft* **32**, 832-838.

- Maxworthy, T. (1979). Experiments on the Weis-Fogh mechanism of lift generation by insects in hovering flight. Part 1. Dynamics of the 'fling'. *J. Fluid Mech.* **93**, 47-63.
- Maxworthy, T. (1981). The fluid dynamics of insect flight. *Ann. Rev. Fluid Mech.* **13**, 329-350.
- Müller, U.K., Stamhuis, E.J. and Ellington, C.P. (in prep.). Quantifying the leading-edge vortex of a 'hovering' robotic insect.
- Nachtigall, W. (1977). Die aerodynamische Polare des Tipula-Flügels und eine Einrichtung zur halbautomatischen Polarenaufnahme. In *The Physiology of Movement; Biomechanics*. (ed. W. Nachtigall), pp. 347-352. Stuttgart: Fischer.
- Nachtigall, W. (1979). Rasche Richtungsänderungen und Torsionen schwingender Fliegenflügel und Hypothesen über zugeordnete instationäre Strömungseffekte. *J. Comp. Physiol.* **133**, 351-355.
- Nachtigall, W. (1981). Der Vorderflügel grosser Heuschrecken als Luftkraftherzeuger. 1. Modellmessungen zur aerodynamischen Wirkung unter schiedlicher Flügel profile. *J. Comp. Physiol.* **142**, 127-134. [Locust wing models in parallel and rotating flow]
- Nachtigall, W. and Kempf, B. (1971). Vergleichende Untersuchungen zur Flugbiologischen Funktion des Daumenfittichs (*Alula spuria*) bei Vögeln. *Z. Vergl. Physiol.* **71**, 326-341.
- Newman, B.G., Savage, S.B. and Schouella, D. (1977). Model tests on a wing section of an *Aeschna* dragonfly. In *Scale Effects in Animal Locomotion* (ed. T.J. Pedley), pp. 445-477. London: Academic Press.
- Norberg, R.Å. (1972). Flight characteristics of two plume moths, *Alucita pentadactyla* L. and *Orneodes hexadactyla* L. (Microlepidoptera). *Zool. Scripta* **1**, 241-246.
- Norberg, R.Å. (1973). Autorotation, self-stability, and structure of single-winged fruits and seeds (samaras) with comparative remarks on animal flight. *Biol. Rev.* **48**, 561-596.
- Norberg, U.M. (1975). Hovering flight of the pied flycatcher (*Ficedula hypoleuca*). In *Swimming and Flying in Nature*, vol. 2 (ed. T.Y. Wu, C.J. Brokaw and C. Brennen), pp. 869-881. New York: Plenum Press.

- Norberg, U.M. (1976). Aerodynamics of hovering flight in the long-eared bat *Plecotus auritus*. *J. Exp. Biol.* **65**, 459-470.
- Norberg, U.M. (1990). *Vertebrate Flight*. Berlin: Springer-Verlag.
- Norberg, U.M., Kunz, T.H., Steffensen, J.F., Winter, W. and Helversen, O.V. (1993). The cost of hovering and forward flight in a nectar-feeding bat, *Glossophaga soricina*, estimated from aerodynamic theory. *J. Exp. Biol.* **182**, 207-227.
- Okamoto, M., Yasuda, K. and Azuma, A. (1996). Aerodynamic characteristics of dragonfly wings and body. *J. Exp. Biol.* **199**, 281-294.
- Osborne, M.F.M. (1951). Aerodynamics of flapping flight with application to insects. *J. Exp. Biol.* **28**, 221-245.
- Payne, F.M., Ng, T.T. and Nelson, R.C. (1988). Visualization and wake surveys of vortical flow over a delta wing. *AIAA J.* **26**, 137-143.
- Pennycuik, C.J. (1972). *Animal Flight*. London: Arnold.
- Pennycuik, C.J. (1975). Mechanics of flight. In *Avian Biology*, vol. 5 (ed. D.S. Farner and J.R. King), pp 1-75. London: Academic Press.
- Pennycuik, C.J., Heine, C.E., Kirkpatrick, S.E. and Fuller, M.R. (1992). The profile drag of a hawk's wing, measured by wake sampling in a wind tunnel. *J. Exp. Biol.* **165**, 1-19.
- Polhamus, E.C. (1971). Predictions of vortex lift characteristics by a leading-edge suction analogy. *J. Aircraft* **8**, 193-198.
- Rayner, J.M.V. (1979a). A vortex theory of animal flight. Part 1. The vortex wake of a hovering animal. *J. Fluid Mech.* **91**, 697-730.
- Rayner, J.M.V. (1979b). A vortex theory of animal flight. Part 2. The forward flight of birds. *J. Fluid Mech.* **91**, 731-763.
- Rayner, J.M.V. (1979c). A new approach to animal flight mechanics. *J. Exp. Biol.* **80**, 17-54.
- Schlichting, H. (1968). *Boundary-layer theory*. New York: McGraw-Hill.
- Shyy, W., Berg, M. and Ljungqvist, D. (1999). Flapping and flexible wings for biological and micro air vehicles. *Progress in Aerospace Sciences* **35**, 455-505.

- Stepniewski, W.Z. and Keys, C.N. (1984). *Rotary-wing aerodynamics*. New York: Dover.
- Sunada, S., Kawachi, K., Watanabe, I and Azuma, A. (1993). Performance of a butterfly in take-off flight. *J. Exp. Biol.* **183**, 249-277.
- Van den Berg, C. and Ellington, C.P. (1997a). The vortex wake of a 'hovering' model hawkmoth. *Phil. Trans. R. Soc. Lond. B* **352**, 317-328.
- Van den Berg, C. and Ellington, C.P. (1997b). The three-dimensional leading-edge vortex of a 'hovering' model hawkmoth. *Phil. Trans. R. Soc. Lond. B* **352**, 329-340.
- Vogel, S. (1967a). Flight in *Drosophila* II. Variations in stroke parameters and wing contour. *J. Exp. Biol.* **46**, 383-392.
- Vogel, S. (1967b). Flight in *Drosophila* III. Aerodynamic characteristics of fly wings and wing models. *J. Exp. Biol.* **46**, 431-443.
- Vogel, S. (1981). *Life in Moving Fluids*. London: Willard Grant.
- Wakeling, J.M. and Ellington, C.P. (1997a). Dragonfly flight I. Gliding flight and steady-state aerodynamic forces. *J. Exp. Biol.* **200**, 543-556.
- Wakeling, J.M. and Ellington, C.P. (1997b). Dragonfly flight III. Lift and power requirements. *J. Exp. Biol.* **200**, 583-600.
- Weis-Fogh, T. (1972). Energetics of hovering flight in hummingbirds and in *Drosophila*. *J. Exp. Biol.* **56**, 79-104.
- Weis-Fogh, T. (1973). Quick estimates of flight fitness in hovering animals, including novel mechanisms for lift production. *J. Exp. Biol.* **59**, 169-230.
- Wells, D.J. (1993). Muscle performance in hovering hummingbirds. *J. Exp. Biol.* **178**, 39-57.
- Werlé, H. (1963). Méthodes de visualisation des écoulements hydrauliques. *La houille blanche*. **Aout/Sept. 1963**, 587-595.
- Willmott, A.P. (1995). *The mechanics of hawkmoth flight*. PhD. Thesis, Cambridge University
- Willmott, A.P. and Ellington, C.P. (1997a). Measuring the angle of attack of beating insect wings: Robust three-dimensional reconstruction from two-dimensional images. *J. Exp. Biol.* **200**, 2693-2704.

- Willmott, A.P. and Ellington, C.P. (1997b). The mechanics of flight in the hawkmoth *Manduca sexta*. 1. Kinematics of hovering and forward flight. *J. Exp. Biol.* **200**, 2705-2722.
- Willmott, A.P. and Ellington, C.P. (1997c). The mechanics of flight in the hawkmoth *Manduca sexta*. 2. Aerodynamic consequences of kinematic and morphological variation. *J. Exp. Biol.* **200**, 2723-2745.
- Willmott, A.P., Ellington, C.P. and Thomas, A.L.R. (1997). Flow visualization and unsteady aerodynamics in the flight of the hawkmoth, *Manduca sexta*. *Phil. Trans. R. Soc. Lond. B* **352**, 303-316.
- Winter, Y., Voigt, C. and Von Helversen, O. (1998). Gas exchange during hovering flight in a nectar-feeding bat *Glossophaga soricina*. *J. Exp. Biol.* **201**, 237-244.
- Wootton, R.J. (1981). Support and deformability in insect wings. *J. Zool., Lond.* **193**, 447-468.
- Wootton, R.J. (1991). The functional morphology of the wings of Odonata. *Adv. Odonatol.* **5**, 153-169.
- Wootton, R.J. (1992). Functional morphology of insect wings. *A. Rev. Ent.* **37**, 113-140.
- Wootton, R.J. (1993). Leading edge sections and asymmetric twisting in the wings of flying butterflies (Insecta, Papilionoidea). *J. Exp. Biol.* **180**, 105-117.
- Wootton, R.J. (1995). Geometry and mechanics of insect hindwing fans – a modelling approach. *Proc. R. Soc. B.* **262**, 181-187.